ABSTRACT

Title of thesis: FLOW FIELD AND PERFORMANCE MEASUREMENTS OF A FLAPPING-WING DEVICE USING PARTICLE IMAGE VELOCIMETRY

Joseph Patrick Ramsey, Master of Science, 2011

Thesis directed by: Professor J. Gordon Leishman
Department of Aerospace Engineering

A flexible flapping wing was tested using various flow interrogation techniques including particle image velocimetry (PIV) to further the understanding of its complex, unsteady, three-dimensional flow field. The flow field was characterized using high-speed flow visualization (FV) in chordwise and spanwise planes to observe and characterize the evolution of flow structures produced. The formation, growth, convection, and shedding of a leading-edge vortex (LEV) was observed on the upper surface of the wing, which was found to mimic the classical process of dynamic stall. A motion-tracking system was used to characterize the complex wing kinematics and aeroelastic deformations of the flexible wing. These measurements were then used to estimate the noncirculatory forces and moments acting on the wing. Two-dimensional velocity fields around the wing contour and in its wake were obtained using PIV. These velocity fields were used to calculate the circulatory lift as well as the drag produced on the wing. It was found that the process of LEV formation, growth, and convection significantly increased the lift production on the flapping wing. The noncirculatory and circulatory lift measurements

were then combined in amplitude and phase to calculate the total lift on the wing. It was shown that the noncirculatory contributions to the airloads were small except near pronation and supination. The flow field results were also used to calculate the lift-to-drag ratio during the wing stroke, where surprisingly it was found that the lift-to-drag ratio increased during the process of LEV formation and shedding. This observation perhaps suggests a reason why flapping-wing flyers intentionally produce LEVs during their wing stroke.

FLOW FIELD AND PERFORMANCE MEASUREMENTS OF A FLAPPING-WING DEVICE USING PARTICLE IMAGE VELOCIMETRY

by

Joseph Patrick Ramsey

Thesis submitted to the Faculty of the Graduate School of the
University of Maryland, College Park in partial fulfillment
of the requirements for the degree of
Master of Science
2011

Advisory Committee:
Professor J. Gordon Leishman, Chair/Advisor
Associate Professor James Baeder
Associate Professor J. Sean Humbert

Acknowledgments

First and foremost I'd like to thank my advisor and thesis committee chair, Professor J. Gordon Leishman, for giving me the opportunity to work under his tutelage on this interesting and challenging project. It has been an honor to learn from Dr. Leishman through the years as an undergraduate Minta Martin Intern and as a Graduate Research Assistant.

I would like to thank Associate Professor Sean Humbert for letting me to use his laboratory for research in this present work. Thanks to Dr. Humbert and Associate Professor James Baeder for their contributions as members of my thesis committee.

Special thanks to David Mayo for assisting in all of the experiments, providing expertise, and always maintaining our "Team Flapping-Wing" spirit.

Many thanks to Dr. Paul Samuel of Daeldus Flight Systems. All of his efforts to keep our experiments running smoothly will be forever appreciated. I would also like to thank Greg Gremillion for all of his efforts in the present research. Thanks to Dr. Manikandan Ramasamy and Bradley Johnson for their mentorship as an undergraduate intern.

I want to thank all of the guys in the lab, Anish Sydney, Joe Milluzzo, Ben Hance, Ajay Baharani, and Juergen Rauleder for making it a blast to come to work everyday. Warm thanks to friends Steven Gerardi and Ryan Robinson for their support as we have gone through the undergraduate and graduate programs together at the University of Maryland.

My deepest appreciation to my family for their unrelenting support: my parents,

Joseph and Maureen, my sisters, Kathleen and Shannon, and our pups, Penny and Luna. My family's unconditional love buoyed my self-confidence and enabled me to accomplish all that I have.

Table of Contents

List of Figures

Nomenclature

a	pitch axis location relative to mid-chord, m
b	semi-chord, m
c	local chord length, m
C_a	sectional total axial force coefficient
$C_{a,c}$	sectional circulatory axial force coefficient
$C_{a,nc}$	sectional noncirculatory axial force coefficient
C_A	wing total axial force coefficient
$C_{A,c}$	wing circulatory axial force coefficient
$C_{A,nc}$	wing noncirculatory axial force coefficient
C_d	sectional drag coefficient
C_D	wing drag coefficient
C_l/C_d	sectional lift-to-drag ratio
C_l	sectional total lift coefficient
$C_{l,c}$	sectional circulatory lift coefficient
$C_{l,nc}$	sectional noncirculatory lift coefficient
C_L/C_D	wing lift-to-drag ratio
C_L	wing total lift coefficient
$C_{L,c}$	wing circulatory lift coefficient
$C_{L,nc}$	wing noncirculatory lift coefficient
$C_{m,1/2}$	sectional mid-chord moment coefficient
$C_{M,1/2}$	wing mid-chord moment coefficient
C_n	sectional total normal force coefficient
$C_{n,c}$	sectional circulatory normal force coefficient
$C_{n,nc}$	sectional noncirculatory normal force coefficient
C_N	wing total normal force coefficient
$C_{N,c}$	wing circulatory normal force coefficient
$C_{N,nc}$	wing noncirculatory normal force coefficient
D	aerodynamic drag, N
F^{nc}	noncirculatory fluid force, N
FM	figure of merit
$\ddot{h}$	plunge acceleration, ms^{-2}
L	aerodynamic lift, N
$(L/D)_R$	rotor lift-to-drag ratio
M	image magnification
M_a	apparent mass
s	reduced time
U,V,W	Cartisian flow velocities, ms^{-1}
U_T, V_T	tangential velocities along integration contour, ms^{-1}
U_{T_1}	flow velocity upstream relative to wing section, ms^{-1}
U_{T_2}	flow velocity downstream relative to wing section, ms^{-1}
w	perturbation velocity, ms^{-1}
x,y,z	Cartisian coordinate system, m

Greek Symbols

α	angle of attack, deg
Δt	pulse separation time, μs
Δx, Δy	grid spacing
Γ_b	circulation, $m\,s^{-1}$
ψ	yaw angle, deg
Ψ	flapping phase angle, deg
ϕ	roll angle, deg
ρ	air density, kgm^{-3}
θ	pitch angle, deg
$\dot{\theta}$	pitch rate, $deg\,s^{-1}$
$\ddot{\theta}$	pitch acceleration, $deg\,s^{-2}$

Abbreviations

CCD	charge coupled device
CFD	computational fluid dynamics
CMOS	complementary metal oxide semiconductor
DARPA	Defense Advanced Research Projects Agency
DAQ	data acquisition
FFT	Fast Fourier Transform
fps	frames-per-second
FV	flow visualization
LEV	leading-edge vortex
MAV	micro air vehicle
PIV	particle image velocimetry
PR-PIV	phase-resolved particle image velocimetry
Re	Reynolds number
TR-FV	time-resolved flow visualization
TR-PIV	time-resolved particle image velocimetry

Chapter 1

Introduction

1.1 Motivation for Micro Air Vehicle (MAV) Development

The present work has been motivated, in part, by the need to determine a suitable platform for a small, efficient, and hover-capable micro air vehicle or MAV. A bio-inspired reciprocating wing motion, or flapping-wing, for a hovering platform has been suggested as one possible solution to this problem. While the inspiration for such a vehicle has obviously been drawn from nature, a flapping wing does not necessarily offer the best engineering solution to the mission challenges or the engineering problems being faced. Therefore, foundational research is still required to validate biomimetic types of flapping wings as a feasible concept for a MAV. To this end, the present work has examined under controlled laboratory conditions the unsteady aerodynamic mechanisms responsible for lift generation on a flapping wing, and has investigated the ability of a prototype flapping-wing MAV concept to efficiently generate lift.

Research into MAVs can be traced back at least to 1997 when the Defense Advanced Research Projects Agency (DARPA) started a program to develop and demonstrate a new type of small air vehicle. This program was intended to inspire the invention of small vehicles that would be capable of sustained hover but having a maximum dimension of only 15 cm. While the classification of a "MAV" has grown today to encompass vehicle sizes other than 15 cm (both smaller and larger), enormous scientific interest con-

tinues to drive the development of small, autonomous MAVs. This interest is fostered by the potential for an air vehicle of small size, low weight, stealth, and agility, amongst other attributes. Such MAVs have many potential military and civil roles. For military applications, hover-capable MAVs are ideal for covert reconnaissance missions that require perch and observe capabilities, or for missions inside buildings where they must fly at low speeds to negotiate corridors, winding stairwells, narrow openings, etc. Such capabilities can offer the modern military increased situational awareness in urban and complex terrain, potentially leading to greater combat effectiveness while suffering fewer casualties. In civil applications, MAVs have several possible uses, such as the ability to investigate a chemically dangerous area or a radioactive environment, homeland defense, law enforcement, disaster response, pipeline patrol, border security, etc.

Over the last decade, the capabilities of MAVs have improved considerably through advancements in design, materials and powerplants. This work has resulted in decreases in size and structural weight, as well as improved levels of aerodynamic efficiency. However, one of the key challenges in improving the performance of MAVs lies in overcoming the problems inherent to low Reynolds number flight. In this regard, the characteristic chord Reynolds numbers of the lifting surfaces on MAVs (whether they be fixed-wings or rotors) are in the range of 10^2–10^5. This aerodynamic regime coincides with higher relative viscous losses and lower aerodynamic efficiencies on the airfoil sections compared to those found at larger chord Reynolds numbers. Figure 1.1 shows that drag coefficients are significantly higher at lower Reynolds numbers. Therefore, the fundamental design issue with a MAV from the perspective of aerodynamic design is to determine the type of platform that will provide the best levels of performance for the intended mission, (i.e.,

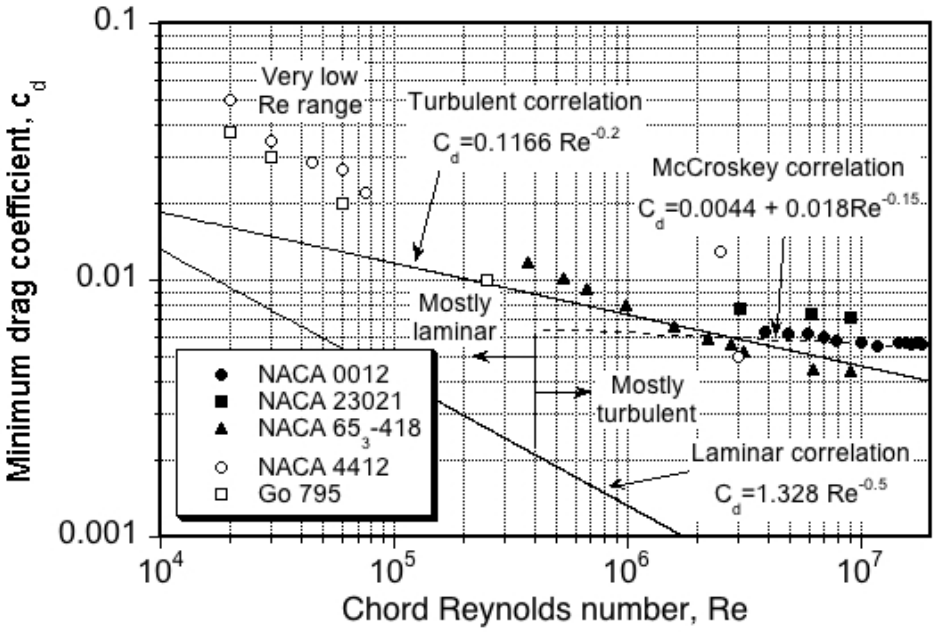

Figure 1.1: Minimum drag coefficients of different airfoils throughout a range of chord Reynolds numbers [1].

the platform to give the best possible payload, flight endurance, range, etc). While such questions are not new, they have not yet been fully answered.

The forgoing situation is especially important for hover-capable MAVs because sufficient empirical performance data has not yet been gathered about the various competing MAV concepts, e.g., rotating wing, cyclorotor, flapping wing, and flotor [2]. In particular, the flapping-wing concept seen in nature may present one solution to the problem of a hovering MAV platform, and biomimetic wings have received much recent interest because of claimed aerodynamic efficiencies at this scale [11]. Much of the available performance data on flapping-wing concepts has been compiled by Mayo and Leishman [2], which is shown in Fig. 1.2. This plot compares hover-capable platforms using power loading as the efficiency metric. Power loading is an absolute (rather than relative) measure of

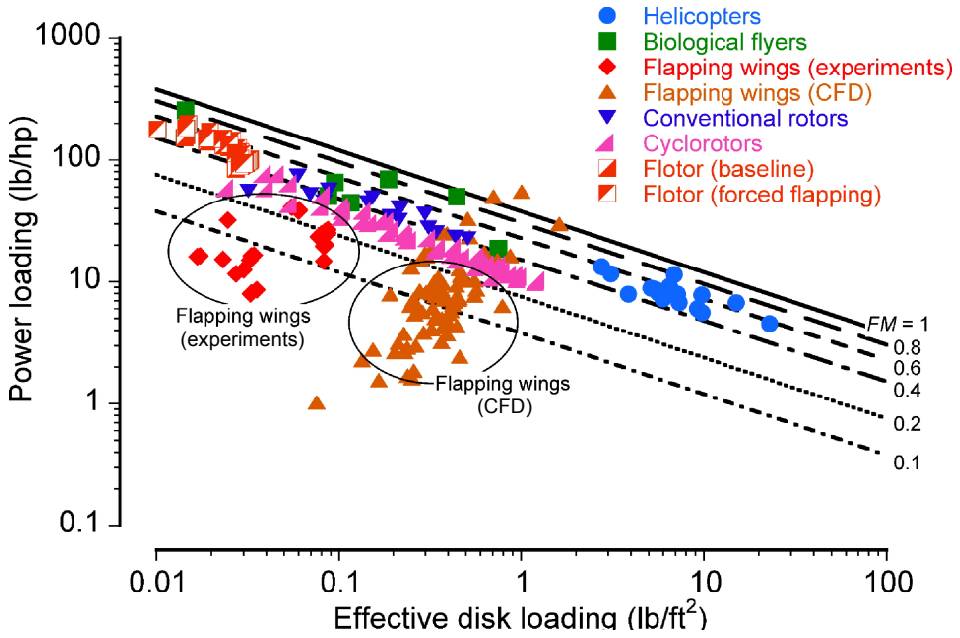

Figure 1.2: Comparison of available performance data for hover-capable MAVs [2].

efficiency given that it represents the ratio of thrust produced per unit power expended [1]. When compared to other rotating-wing MAV systems, it is clear that biomimetic flapping wings have thus far achieved relatively low values of hovering efficiency, as shown in Fig. 1.2.

Biomimetic flapping wings may still offer a solution as a hovering MAV platform because of their low noise and stealth capabilities as well as their maneuverability and agility at this scale. However, the concept must be much more thoroughly investigated from the perspective of fundamental aerodynamics. Specifically, there is a need for greater understanding of the fundamental aerodynamic mechanisms responsible for lift generation, as well as additional performance measurements that can help validate the flapping wing as a viable lift-generating mechanism for a MAV. This understanding may then allow for more efficient and reliable MAVs to be designed.

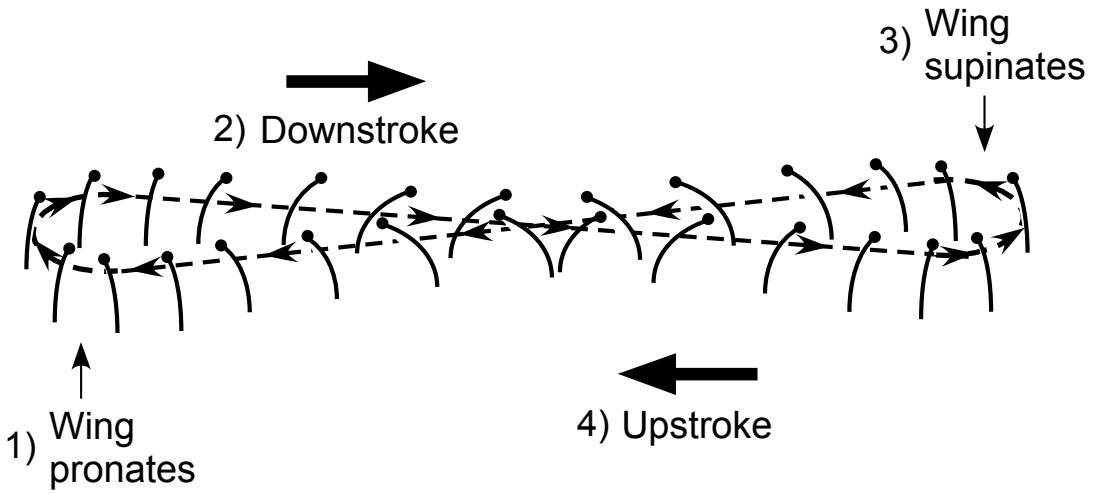

Figure 1.3: Wing kinematics of reciprocating flapping-wing motion: 1) Pronation; 2) Downstroke; 3) Supination; 4) Upstroke.

1.2 Flapping-Wing Flight

In nature, many insects and some birds (e.g., hummingbirds) utilize a patten of reciprocating wing motion, e.g., [12]. This reciprocating motion exploits unsteady aerodynamic forces to generate lift, and enables these creatures to fly successfully and navigate various environments with great agility. The wing kinematics of this reciprocating motion feature two translational motions (downstroke and upstroke), where the wing sweeps through the air at a relatively large pitch angle, and two rotational motions (called pronation and supination) where the wing rotates its pitch to reverse the direction of its sweep. The wings reach positive pitch angles on both parts of the ensuing translational motion. Figure 1.3 shows a schematic of a representative flapping cycle, which continuously repeats the process of: pronation, downstroke, supination and upstroke.

1.3 Unsteady Lift Enhancement Mechanisms in Flapping-Wing Flight

Steady and quasi-steady aerodynamic theory, experiments, and modeling (e.g., computational fluid dynamics or CFD) have not yet fully explained the ability of flapping-wing flyers to generate the needed values of lift to achieve hover and to fly forward at the observed speeds [5]. In this regard, unsteady lift mechanisms are now known to be important, but they are still not fully understood. In particular, several unsteady lift mechanisms on flapping wings have been recognized in previous research [3, 13], and these mechanisms have been examined further during the course of the present research.

1.3.1 Leading-Edge Vortex (LEV)

The formation of a leading-edge vortex (LEV) has been noted during many types of flapping-wing motion. The LEV forms on the upper surface of the wing, and can be responsible for significantly increasing lift forces on the wing. This outcome occurs because the presence of a LEV lowers the local pressure on the upper surface of the wing, thus increasing the overall lift. The presence of the LEV, however, can also be expected to increase the drag on the wing, which raises some interesting questions about the efficiency of flight under these conditions. A prominent example of LEV formation occurs on delta wings [14], where a stable conical LEV structure forms on the upper surface and provides enhanced lift generation. This type of flow gives a delta wing a high stall angle of attack, which can be exploited for takeoff and landing, as well as maneuver performance.

LEVs have also been experimentally identified and studied both on live insects and birds as well as mechanical models [3, 13, 15–17], and the phenomenon has been further

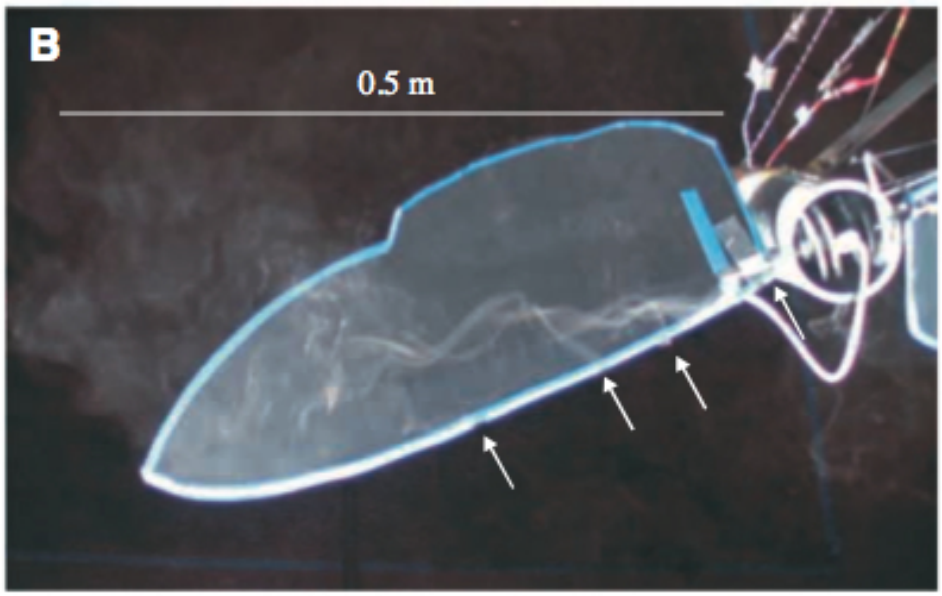

Figure 1.4: Image of conical LEV on hawkmoth wing at angle of attack of 35° [3].

analyzed using CFD [18, 19]. Specifically, the detailed characteristics of the LEV, including its formation and shedding process, have been the subject of much recent research interest [5, 6, 20]. Given its ability to augment the lifting performance of a wing, exploiting the aerodynamic benefits of LEV generation could be crucial in the successful design of MAVs.

The existence of LEV formation in nature was discovered by Ellington et al. [3], who imaged its formation using flow visualization on a tethered live hawkmoth. Later, the formation of the LEV was studied in greater detail on a dynamically-scaled mechanical model. At an average chord Reynolds number around 5,560, Ellington et al. [3] found that the LEV formed a conical spiral and encompassed an increasing amount of the wing chord as the wing span increased, as shown in Fig. 1.4. Near the wing tip, the LEV separated and joined with the tip vortex. They found similar characteristics of LEV formation

and shedding between the tethered insect and their model, and initially noted that LEV formation resembled the process of dynamic stall. During dynamic stall, as an airfoil pitches to very high angles there is a delay in the onset of flow separation, and a vortex is formed at the leading edge of the airfoil [1]. The vortex grows in strength and the detaches from the leading edge to convect over the upper surface of the wing. This vortex is then shed from the wing into the downstream wake, resulting in gross stall on the wing.

Later work by Usherwood and Ellington [21] used smoke flow visualization on this mechanical hawkmoth wing to discover that the LEV was stable on the wing during its translational stroke. It was postulated that the LEV was stabilized by a strong spanwise flow through the core of the vortex. This spanwise flow was postulated to remove energy from the vortex core, preventing the growth and eventual shedding of the LEV. It was noted that a stable LEV could lead to continuous lift augmentation through the entire flapping cycle. While the foregoing process is different when compared to the features of classic dynamic stall [1], this type of LEV structure is more similar to that seen on delta wings [20]. As previously mentioned, instead of shedding vortices from the leading edge, the vortex flow on the upper surface of a delta wing maintains a stable structure. Figure 1.5 shows the structure of the LEV and the spanwise flow through its core as described by Usherwood and Ellington [21].

The stability of the LEV was further investigated by Birch and Dickinson [5] on a dynamically scaled fruit fly wing operating at a chord Reynolds number of 160. Their research found that the stabilization of the LEV in their case was not achieved by spanwise flow through the vortex core. While the LEV did remain attached throughout the entire wing stroke, they found that the spanwise velocity within the core of the LEV was rela-

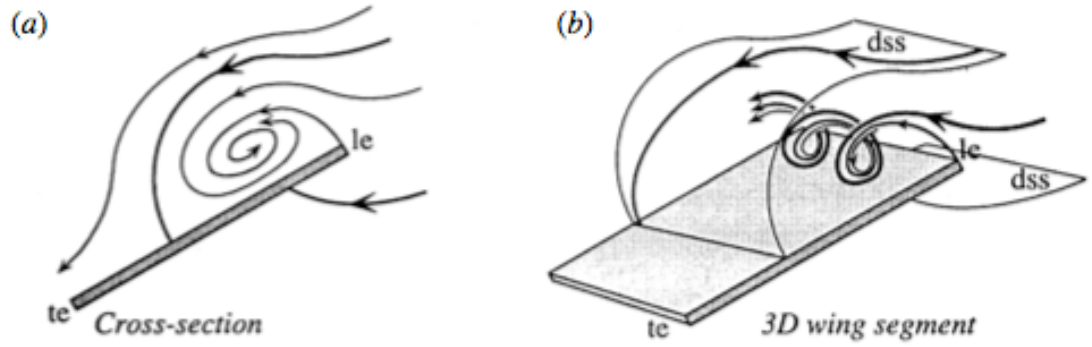

Figure 1.5: Conical LEV structure: a) cross-section of LEV; b) three-dimensional view of LEV structure and spanwise flow ("le" denotes leading edge, "te" denotes trailing edge, "dss" denotes dividing stream surface) [4].

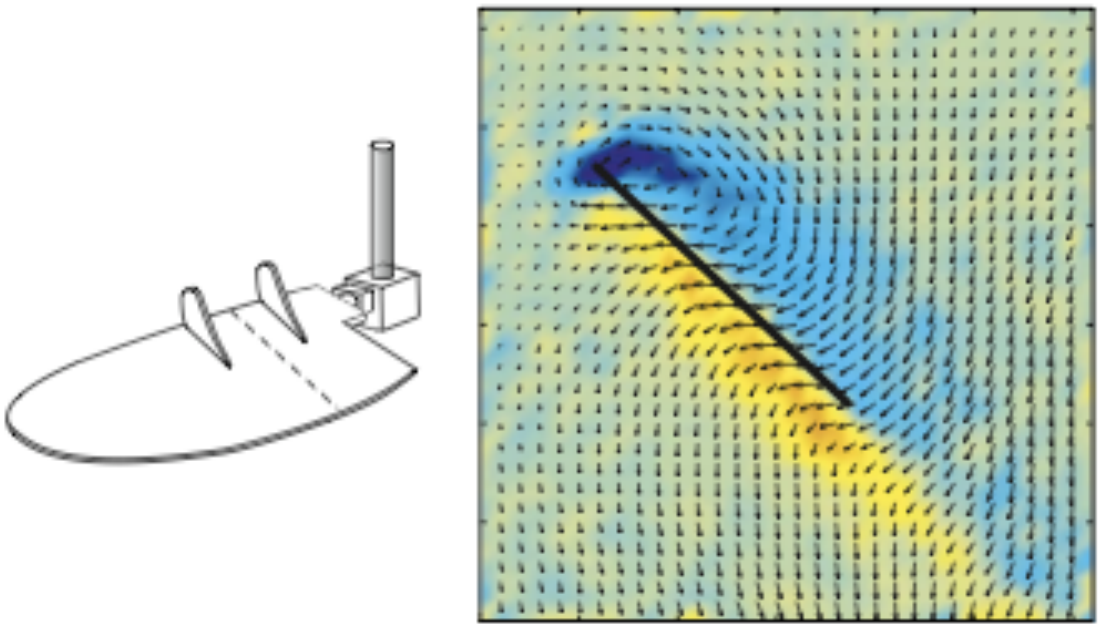

Figure 1.6: Wing with fences placed on its upper surface to inhibit spanwise flow, and resulting velocity field showing the LEV in blue [5].

tively low, being only 2–5% of the mean velocity of the wing tip. They instead suggested that a downward flow induced by the tip vortex and wake vorticity limited the growth of the LEV and contributed to its attachment throughout the wing stroke. To further test the effect of spanwise flow, Birch and Dickinson [5] applied fences and baffles on the upper surface of the wing to inhibit spanwise flow, and they demonstrated that the LEV still did not detach from the wing. Figure 1.6 shows their setup, and the resulting velocity field showing the presence of the LEV. These authors emphasized that their results suggested some dependence upon Reynolds number as it affects the stability characteristics of the LEV.

Besides experimental studies, the LEV has also been examined computationally. Shyy and Liu [19] performed CFD computations on flapping wings for a range of Reynolds numbers, and specifically examined the hawkmoth and fruit fly wing geometries used in previous research. They found a much more pronounced spanwise flow through the core of the LEV on the hawkmoth wing compared to the fruit fly wing, which was consistent with previous experimental findings [21]. In the evaluation of the stability of the LEV, the results showed that the fruit fly wing maintained a stable LEV throughout its translational stroke, whereas with the hawkmoth model the LEV was shed during the downstroke.

Srygley and Thomas [16] performed flow visualization on an untethered, free-flying butterfly, and examined the LEV development in various modes of flight (climb, maneuver, forward flight). During climb and gentle maneuver, they found that two LEVs formed on the upper surface of the wings. They postulated that in these particular flight modes, the insect required more lift and modified its wing kinematics to exploit lift enhancement from the LEVs. During forward flight, however, the LEVs were not observed to occur

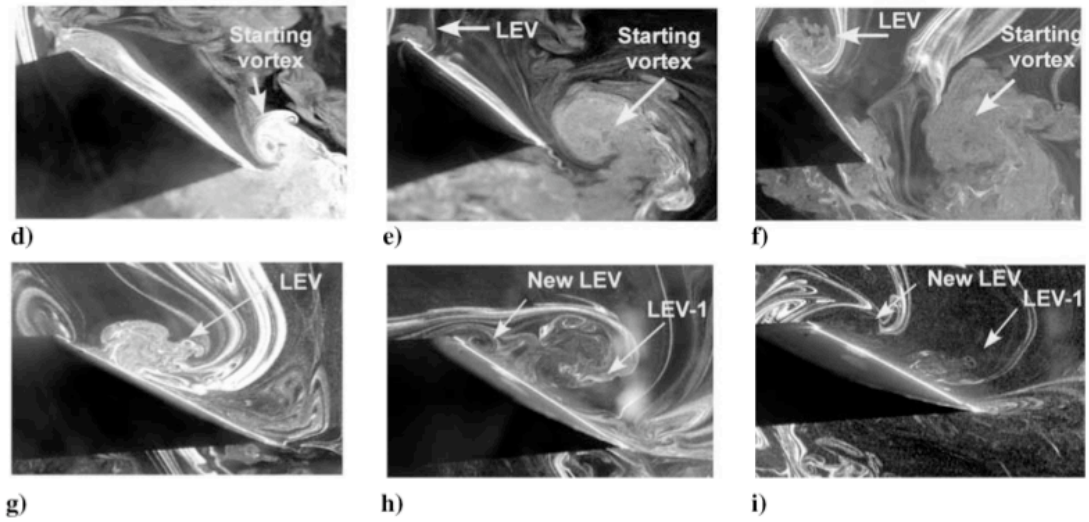

Figure 1.7: Chordwise flow visualization images by Ramasamy and Leishman: d) start of translational stroke; e) accelerating wing; f) midpoint of translational motion; g) spilled LEV; h) formation of new LEV; i) multiple vortices [6].

over the wing. Their research also demonstrated that the LEV generated by the butterfly did not resemble LEV structure seen in previous experiments; the butterfly produced a LEV of approximately constant diameter across the wing span, as opposed to the spiral LEV structure that was seen on the hawkmoth.

Other research has been conducted by Tarascio et al. [15] and Ramasamy and Leishman [6] on a biomimetic flapping-wing device that was operated at a mean chord Reynolds number of about 15,500. In this work, it was shown that the LEV was not stable throughout the wing stroke. Utilizing flow visualization and particle image velocimetry (PIV), they noted a continual formation, convection and shedding process of the LEV, with several LEVs formed on the upper surface of the wing during a single wing stroke. This behavior was noted to be similar to the classic features of dynamic stall, and was at variance with the stable LEV theory. Additionally, they showed that the shedding of

the LEV occurred despite the measurement of a significant spanwise flow on the upper surface of the wing. They noted that the continual presence of at least one vortex over the wing might help to explain sustained lift generation shown by flapping wings during stationary hovering flight. Figure 1.7 shows the LEV shedding process through the downstroke of the wing motion as taken from Ramasamy and Leishman [6].

Usherwood and Ellington [21] examined the lift and drag production on model hawkmoth wings for a fairly wide range of parameters, including angle of attack, twist, and camber. At an angle of attack around 41°, they showed that the wing lift coefficient can reach as high as 1.75 if a stable LEV is produced over the wing. Birch et al. [22] made force measurements on a dynamically scaled fruit fly wing at two different chord Reynolds numbers of 120 and 1,400. They found that an impulsively started flapping wing showed constant force generation during its wing stroke. They suggested that the constant force generation was a result of the stable attachment of the LEV. They also noted that a higher maximum lift occurred at higher chord Reynolds numbers. The maximum measured lift coefficient at a chord Reynolds number of 120 was around 1.7, whereas at a chord Reynolds number of 1,400 they found a maximum lift coefficient of 2.1.

1.3.2 Noncirculatory Lift Production

A flapping wing experiences significant time-varying changes in pitch angle throughout the flapping cycle, most significantly at the end of each half-stroke, i.e., during pronation and supination. Here, the wing rotates through a large pitch angle of about 90° in a very short time. The resulting pitch rates are typically greater than $10,000^\circ$ per second.

Dickinson et al. [13] measured the forces acting on their flapping wing throughout the entire wing stroke and found large force peaks just before the end of each half-stroke. They attributed this result to the rapid pitching up motion of their wing at the end of each half-stroke, but did not identify the origin of these forces, i.e., whether they were of circulatory or noncirculatory origin. Sun and Tang [18] utilized CFD to analyze the aerodynamic forces on the same model fruit fly wing. Their research suggested that the force peak at the end of a half-stroke resulted from the rapid growth in vorticity during pitching motion. The results from this CFD analysis were in good agreement with force measurements acquired by Sane and Dickinson [23].

The primary question that remains, however, is how much of the force peaks arise because of the generation of circulation and how much of it is because of noncirculatory effects. Such high pitch rates will certainly affect the lift generation on the flapping wing through flow acceleration effects, which result in the production of noncirculatory aerodynamic forces. This phenomenon is otherwise known as the "apparent mass" effect, and arises because of pressure forces required to accelerate the fluid near the wing [1]. These pressure forces appear as reaction forces and moments on the wing. In terms of lift generation, the pitch rate contribution to the noncirculatory lift depends on the instantaneous kinematics of the wing (primarily its translational and angular accelerations), and the effects can be evaluated using unsteady thin airfoil theory, as discussed by Theodorsen [24]. The evaluation of the noncirculatory and circulatory effects in the flow for a flapping-wing motion was an important objective of the present work.

1.3.3 Wake Capture

The reciprocating motion of flapping wings can cause the wing to interact with its near wake during a subsequent wing stroke (or strokes). At the conclusion of pronation and supination, the encounter between the wing and the previously shed wake may lead to enhanced lift generation at the beginning of each half-stroke; this mechanism is known as wake capture. As the wing reverses direction, the incoming free-stream velocity may also be increased by the induced effects of the incoming shed wake. In some cases, it has been shown that a flapping wing can encounter a shed LEV at the beginning of its half-stroke during part of this wing-wake interaction. Therefore, a better understanding of this interaction may lead to a MAV with more highly optimized wing kinematics that could take advantage of this mechanism of lift production.

Dickinson et al. [13] showed lift enhancement from wake capture on their flapping-wing mechanism. They noticed a lift force peak directly after the conclusion of pronation and supination. To confirm that it was wake capture, they predicted that because a significant part of the velocity field that the wing encountered at the beginning of the half-stroke was from the previously shed wake, the wing should continue to generate a force from the incoming wake velocity, even if the wing was stationary. They found that the lift force peak persisted after the cessation of wing motion, demonstrating that the shed wake served as one energy source for lift generation. Their research also showed that lift enhancement from wake capture was highly dependent upon the wing kinematics at the end of each half-stroke.

Tang et al. [25] investigated wake capture through CFD simulations. Using typical

hovering flight kinematics, they confirmed that a lift peak was produced as the wing commenced each half-stroke. They also varied the chord Reynolds number to examine the effects on lift production throughout the wing stroke, and noticed that an increase in Reynolds number (from 75 to 500) led to greater asymmetry in lift production between the two half-strokes. The ability of wake capture to enhance lift was noted to be highly dependent on Reynolds number.

1.3.4 Clap-and-Fling Mechanism

A two-stage wing-wing interaction, known as the "clap-and-fling mechanism" was first discovered on a tiny wasp by Weis-Fogh [7], and the resulting fluid dynamics can be responsible for enhanced lift generation on flapping wings. The entire process occurs at the end of a half-stroke and is shown in Fig. 1.8. During the "clap" phase, an insect brings the leading edge of its wings together during wing pronation/supination until they are in close proximity and almost parallel to one another, as shown in Fig. 1.8 A–C. Figure 1.8 C shows that the closing gap between the wings pushes fluid out, providing a boost to thrust generation. Following this is the "fling" phase where the wings rotate about their trailing edge away from one another to begin their translational stroke, as shown in Fig. 1.8 D–F. As the leading edges of the wings separate, fluid rushes into the growing gap between the wings, causing an increase in circulation. A LEV begins to form as the wing enters its translational stroke. This fluid dynamic process was later discovered on other small insects by Ellington [26], and Ennos [27].

Lehmann et al. [28] examined the lift augmentation produced by the clap-and-fling

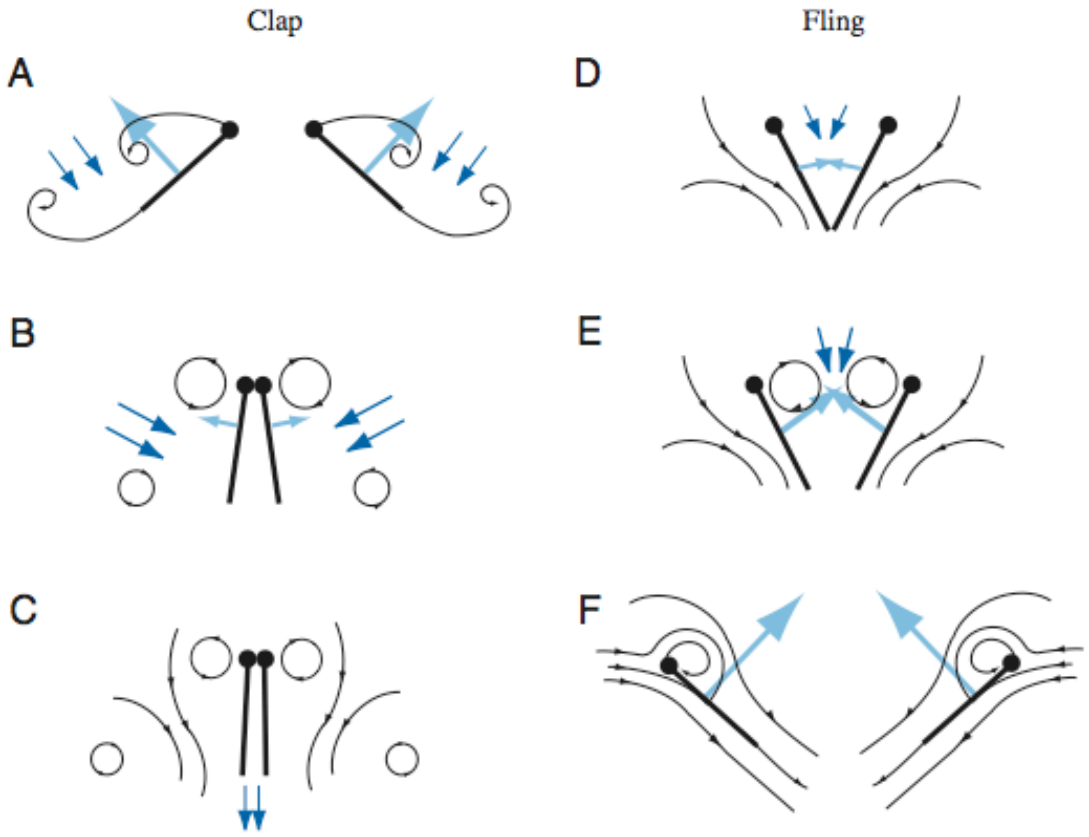

Figure 1.8: Schematic showing the clap-and-fling mechanism discovered by Weis-Fogh [7] and illustrated by Sane [8]: A) wings approach the end of half-stroke; B) wings move toward one another; C) fluid is pushed out by closed gap; D) wings rotate about the trailing edge; E) fluid rushes into the widening gap; F) LEV formation begins during translation.

mechanism on a scaled fruit fly wing at a chord Reynolds number between 50–200. To evaluate the effects produced by this mechanism, they compared force measurements from a single flapping-wing configuration to that of a dual flapping-wing configuration. They found that the process of clap-and-fling could increase the lift by as much as 17% in the dual flapping-wing configuration. Lehmann et al. [28] also examined the predicted effect of increased LEV strength during the fling phase. They quantified the circulation of the LEV and noted increased values with the dual-wing configuration to be as high as 32%. The frequency of the flapping wings was varied to examine how clap-and-fling was affected by different chord Reynolds numbers. Lehmann et al. [28] found that as Reynolds number increases in this limited range of 50–200, the lift enhancement resulting from the clap-and-fling motion begins to decrease.

It should be pointed out that the clap-and-fling mechanism is not utilized by all insect flyers, especially those at larger scales [8,29]. Additionally, this phenomenon could simply result from need of the insect to maximize its stroke amplitude [8]. Previous research has suggested that optimal lift generation occurs at the maximum 180° of stroke amplitude [30].

1.4 Rigid Versus Flexible Flapping Wings

Much flapping-wing research reported in the literature has been focused on the testing of rigid flapping wings rather than more realistic flexible (i.e., elastic) flapping wings. Because of the desire to avoid the added complexities posed by aeroelastic wing deformation produced by aerodynamic and inertial loading throughout the flapping cycle,

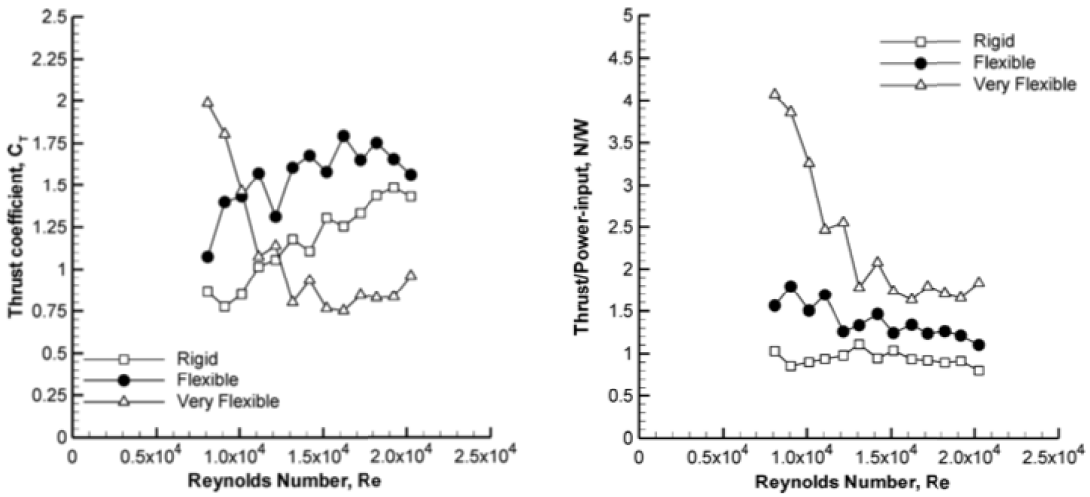

Figure 1.9: Thrust coefficient and power loading as a function of Reynolds number [9].

most research has been conducted on more rigid wings. However, it has been shown [12] that wing flexibility can improve flapping wing performance at high angles of attack, and better adapt to the unsteady aerodynamic environment. In particular, the stall angle of attack has been shown to increase as much as 20° when using a flexible wing versus a rigid wing, while maintaining comparable lift-to-drag ratios throughout the range of angle of attack [31].

Heathcote et al. [9] investigated the effects of wing flexibility on a plunging wing at zero free-stream velocity, which was an experiment designed to mimic a flapping wing in hovering flight conditions. They made direct force measurements, and removed contributions from inertial forces to calculate the aerodynamic forces. Three wings of different bending stiffnesses were tested, and were referred to as "rigid," "flexible," and "very flexible." The wings were tested over a range of chord Reynolds numbers from 8,000 to 20,000 with some of their results being shown in Fig. 1.9. For the low range of these chord Reynolds numbers, the most flexible wing produced the highest thrust coefficient.

However, after the chord Reynolds number exceeded 10,000, the flexible wing produced the highest thrust coefficients. The flexible wing always outperformed the rigid wing, but the rigid wing produced higher thrust values than the most flexible wing at higher Reynolds numbers. The thrust results were normalized by the power to provide a measure of wing efficiency. The most flexible wing demonstrated better thrust to input power ratios compared to the other two wings, especially in the lower range of Reynolds numbers. Additionally, the flexible wing was found to be more efficient than the rigid wing throughout the entire Reynolds number range. These outcomes showed that some level of wing flexibility favorably affected performance.

Research conducted by Ho et al. [32] showed the potential advantages of increased wing flexibility in forward flight. The thrust coefficient at several forward flight speeds was measured on a wing covered with a paper membrane and also with a more flexible Mylar membrane, the wings otherwise being geometrically identical. The Mylar membrane was found to produce higher thrust coefficients, more significantly at the lowest forward speeds. The benefits from exploiting wing flexibility have qualifications, however, given that the findings showed that a wing with a flexible leading edge showed significantly lower lift coefficients in comparison to that with a rigid leading edge.

Force measurements were made on rigid and flexible wings that were modeled from hawkmoth wings [33]. Specifically, the flexible wing was designed to have an approximate flexural stiffness distribution and wing deformations measured from the moth wings. The researchers found that the flexible wings showed increases in power efficiency while maintaining similar generation of aerodynamic forces when compared to the rigid wings.

The role of wing flexibility was explored using dynamically-scaled experiments as

well as numerical simulations [34]. In their experiments, they found that a flexible wing consumes less power than a rigid wing for the same wing kinematics. However, the rigid wing generated larger values of mean lift compared to the flexible wing throughout the flapping cycle. Their results also showed that the flexible wing required less power per unit lift when compared to the rigid wing.

It should be noted that adding some structural flexibility to a flapping wing has been shown to be beneficial for performance, and it also allows for the passive control of wing pitch. More research is required to understand the aeroelastic problem posed by flexible wings, and perhaps to find a better optimized wing design for a flapping-wing MAV.

1.5 Particle Image Velocimetry (PIV) Studies of Flapping Wings

Particle image velocimetry (PIV) is a flow measurement technique that can be used to measure both two-dimensional and three-dimensional velocity fields. The measurements are achieved by seeding a given flow with submicron flow tracer particles, and illuminating a plane in the flow with a laser light sheet. A camera is placed orthogonal to the light sheet, and captures two successive images of the seeded flow within a given pulse separation time of the order of microseconds. The resulting displacements of the flow tracers are calculated using a cross-correlation procedure, and using the pulse separation time the velocity field in the plane of interest can then be computed. PIV as used in the present work will be explained in greater detail in Chapter 2 of this thesis.

Previous research has utilized PIV in various forms to examine the flow field on both live and mechanical flapping wings. Bomphery et al. [35] used two-dimensional

PIV to examine the velocity fields produced on a tethered hawkmoth. They performed PIV at several locations in the wing stroke and compiled these results into a time-resolved history of the flow field. PIV measurements were taken of the flow field of a free-flying hummingbird by Warrick et al. [17]. They examined the complex wake structure as well as how the shed vortices evolved and diffused into the far-field wake.

PIV has been utilized in several studies on a dynamically-scaled fruit fly wing in an oil tank, where small air bubbles were used to trace the flow. Birch and Dickinson [36] used PIV to quantify the flow around the wing throughout the entire wing stroke. The velocity fields were then used to calculate the vorticity fields, allowing for an understanding of how vortical structures were generated in the flow [36, 37]. Dickinson et al. [13] used PIV to characterize the near wake at the end of a half-stroke as part of a greater analysis to determine the most efficient timing for wing pronation/supination. Stereoscopic PIV was also performed on the fruit fly wing to obtain three-dimensional velocity fields throughout the flapping cycle [38]. Wang et al. [37] used velocity fields acquired by PIV to evaluate the accuracy of their CFD model in predicting the flow field generated by the fruit fly wing.

As previously mentioned, PIV measurements have also be made on a biomimetic flapping-wing mechanism by Ramasamy and Leishman at the University of Maryland [6]. They quantified the magnitude of the spanwise flow on the upper surface of the wing and discovered that it was approximately equal to the maximum wingtip velocity. Ramasamy and Leishman [6] tracked the peak swirl velocity of the root and tip vortex throughout the wing stroke, and found that the tip vortex was always stronger than the root vortex. They also saw a decrease in the peak swirl velocity in the root and tip vortices as they were

convected into the wake. This diffusion was accompanied by an increase in core radius, which redistributed the vorticity but conserved circulation. Their measurements also revealed a higher than expected growth rate of the tip vortices, suggesting greater levels of turbulence were present inside the vortex cores despite having low vortex Reynolds numbers of only around 10,000.

1.6 Other Previous Research Using Flow Measurements

Various methodologies can be applied to make flow velocity measurements to establish estimates of the aerodynamic forces. Bomphery et al. [35] performed PIV across the chord of the wing of a rigidly tethered hawkmoth inside a wind tunnel at two different forward flight speeds. From the planar velocity fields, they measured the circulation of the shed vortices by calculating a line integral of the tangential velocities around a single elliptical loop that enclosed the vortex core. This process used Kelvin's theorem of equivalence of shed and bound circulation of an impulsively started airfoil. They coupled this analysis with direct force measurements, and found that the circulation loop method gave 85% of the measured resultant force. This discrepancy was partly attributed to the three-dimensional nature of the flow, given that the estimates were made from two-dimensional PIV measurements. Their force measurements and circulation estimates also demonstrated a peak upward force when the LEV was present over the chord at the end of the downstroke.

Poelma et al. [38] utilized velocity fields obtained from PIV to calculate the forces acting on a dynamically-scaled fruit fly wing. They used an exact equation as derived by

Wu [39] to predict the total forces acting on the wing. They compared their calculations to force measurements made by a sensor mounted at the base of the wing, and found that the equation systematically underpredicted the lift by 10–20% throughout the wing stroke.

A recent study by Warrick et al. [17] has made PIV measurements on a live hummingbird in free flight, examining lift production throughout its wing stroke. This research utilized a single circular integration loop to calculate the bound circulation. They found that the hummingbird generated more than twice as much circulation during its downstroke compared to its upstroke.

1.7 Objective of the Present Work

The present work contributes to the understanding of the complex, unsteady, three-dimensional flow field produced on a flexible flapping wing. The flow field was measured using high-speed flow interrogation techniques, including time-resolved flow visualization (FV) and time-resolved particle image velocimetry (PIV). The wing kinematics were characterized using a motion tracking system. Phase-resolved particle image velocimetry was used to acquire velocity fields, and the measurements were used to calculate the components of the lift and drag of the flapping wing. Specifically, the work was an attempt to better quantify the aerodynamic efficiency of a flapping wing and contribute to the scope of performance measurements at MAV scale.

These flow interrogation techniques allowed for a better characterization of the unsteady lift enhancement mechanisms, as mentioned previously in Section 1.3. In this regard, the LEV was imaged during its formation, convection, and shedding throughout

the wing stroke. The effect of the LEV on the lift and drag was calculated using the velocity fields obtained from the PIV. The pitching up motion at the end of each half-stroke was characterized using the motion tracking system to examine its impact on lift production. The results obtained contribute to the understanding of flapping-wing flow fields, and add much needed measurements and other data in this low Reynolds number realm. One interesting result from this work was that the presence of the LEV over the chord led to an increase in the lift-to-drag ratio of the wing section. This outcome contrasts with classic dynamic stall, where the onset of LEV formation and convection leads to a rapid decrease in the sectional lift-to-drag ratio.

1.8 Organization of Thesis

The present work explores the flow field of a prototype flapping-wing MAV and has obtained measurements of its lift and drag production. The motivation behind MAV development and the fundamentals of flapping-wing aerodynamics have been discussed in the present chapter. A review of past research on unsteady lift mechanisms, and comparisons between flexible and rigid flapping wings has also been discussed. Chapter 2 gives a comprehensive description of the experimental techniques that were utilized to characterize the flow field and to make performance measurements. These descriptions include the motion tracking system, and the flow interrogation techniques of flow visualization and particle image velocimetry. The fundamental principles, equipment used, and challenges unique to each experimental technique are explained. Chapter 3 documents the results in terms of flow field characterization, velocity measurements, and performance

measurements. Chapter 4 concludes the thesis by discussing the significance of the findings, and suggesting future experimental goals toward better understanding the potential performance characteristics of flapping-wing MAVs.

Chapter 2

Description of the Experiments

2.1 Introduction

To help understand the complex flow field generated by a flapping-wing, with the objective of gaining new insight into its hovering aerodynamics and to quantify its efficiency, several types of experiments were performed. This chapter provides a description of the experimental setups , the equipment used, the fundamental principles of the flow interrogation techniques, and also discusses the challenges in performing such experiments.

2.2 Flapping-Wing Test Rig

The biomimetic type of flapping-wing rig that was tested in the present work was modified from a prototyped MAV. This MAV was light enough to be capable of free-flight when the flapping frequency was 25 Hz. Given that the aerodynamics of the problem was of primary interest in the present work, all flight control servos and associated electronics were removed from the device. A small electric motor and gear system was used to drive the wing motion, and the frequency was varied by changes in the supply voltage. The pitch of the wing was passively controlled by the design of the wing mount, although there was also an aeroelastic response of the wing to aerodynamic and inertial forces during its stroke, as well be discussed in Chapter 3. A schematic of the test rig is shown

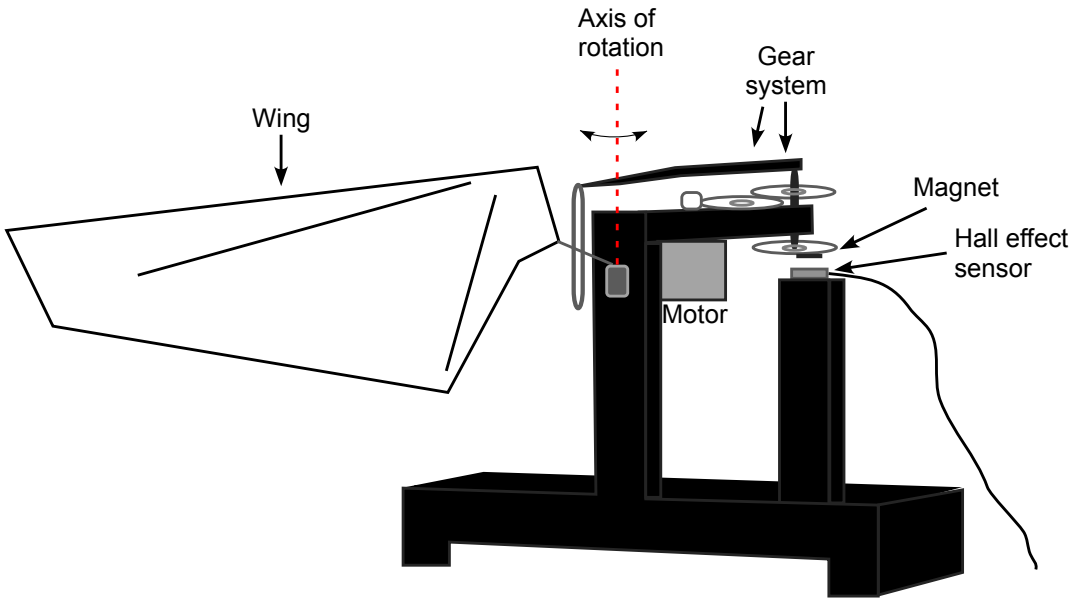

Figure 2.1: Schematic of flapping-wing MAV test rig.

in Fig. 2.1.

The kinematics of the wing stroke was designed to mimic the flapping cycle seen in insects and some birds (e.g., hummingbirds). In this regard, the flapping stroke consisted of four parts: 1) Pronation, where the wing rotated at the end of its upstroke to a positive pitch angle on its downstroke; 2) A downstroke, where the wing translated at changing pitch angles; 3) Supination, where the wing rotated at the end of its downstroke to a positive pitch angle on its upstroke; 4) An upstroke, where the wing translated at changing pitch angles (see also Fig. 1.3)

The wing was constructed of carbon rods of 0.3 and 0.5 mm diameter to which was bonded a 5 μm thick Mylar sheet. The leading-edge spar was bonded to a 0.5 mm diameter titanium wire, which was inserted into a brass rivet. This rivet was then secured into the rotational axis of the mechanism. To strengthen the carbon-titanium bond,

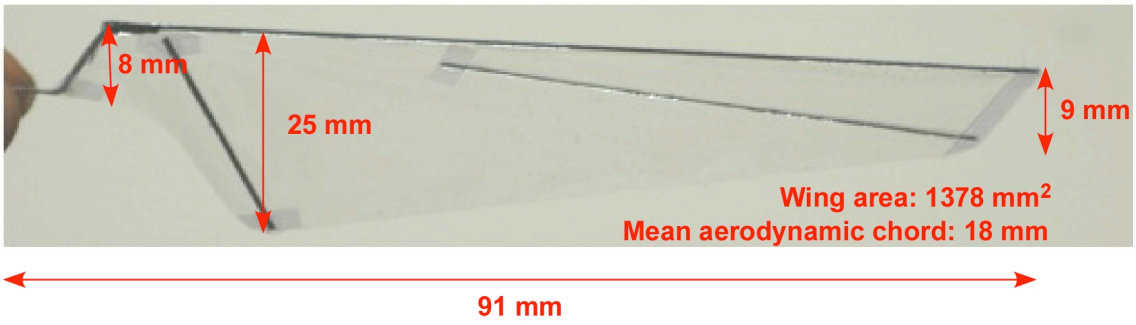

Figure 2.2: Geometry of wing and its characteristic dimensions.

lightweight Kevlar thread was tightly wrapped and bonded to this joint. Small pieces of translucent tape were applied to the wing root, wing tip and inner spar tips, which reinforced several stress points and completed the fabrication of the wing. However, the extremely lightweight construction of the wing meant that the lifespan of each wing was approximately one hour of testing (until the onset of significant structural fatigue), and about two hours to structural failure. Each wing was constructed using an identical process, minimizing the impact of manufacturing imperfections on the characteristics. The consistency of the wing construction was checked throughout the experiments, and this issue is discussed in Chapter 3. Figure 2.2 shows a photograph of the completed wing, along with its characteristic dimensions. The chord Reynolds number based on the average wingtip velocity, a flapping frequency of 17 Hz, and the mean aerodynamic chord was approximately 9,000.

The test rig for the flapping wing was fixed to a stand with the stroke plane approximately ten semi-spans above the floor. This stand allowed for translation and rotation of the test rig, which eliminated time-consuming laser and camera re-alignment for each stroke angle of interest. The present experiments used a single-wing configuration, with

the application of a vertical image plane to produce flow symmetry. More recent tests have been conducted with a dual-wing configuration with two wings flapping in phase. The results from the dual-wing experiment have demonstrated that conducting experiments on a single-wing with an image plane accurately represents the flow field of a dual-winged device. These results will be shown in Chapter 3.

2.3 Motion Capture System

A motion capture system was used to measure the wing motion. This system allows for the tracking of an object in three-dimensional space, which is done by applying retroflective reference markers to its surface and placing high-speed cameras in various positions and orientations around the object. The camera system then tracks the markers in space and time by utilizing triangulation methods. The camera system must be placed such that at least two of the cameras can image each marker at any one time. The camera system has an operable capture frame rate in the range of 60 to 800 frames-per-second (fps) depending on the hardware platform, camera choice, and number of cameras being used. The outcome of such experiments is a time-history of the three-dimensional position of the reference markers, as well as their Euler angles (ϕ, θ, ψ) with respect to a fixed axis.

For the present work, a VICON MX hardware platform was used in conjunction with seven MXF40 cameras. This hardware platform and camera system tracked the markers at a frame rate of 500 fps. Flat markers of 3.5 mm in diameter were placed across the wing to measure the wing displacements and aeroelastic deformations at six

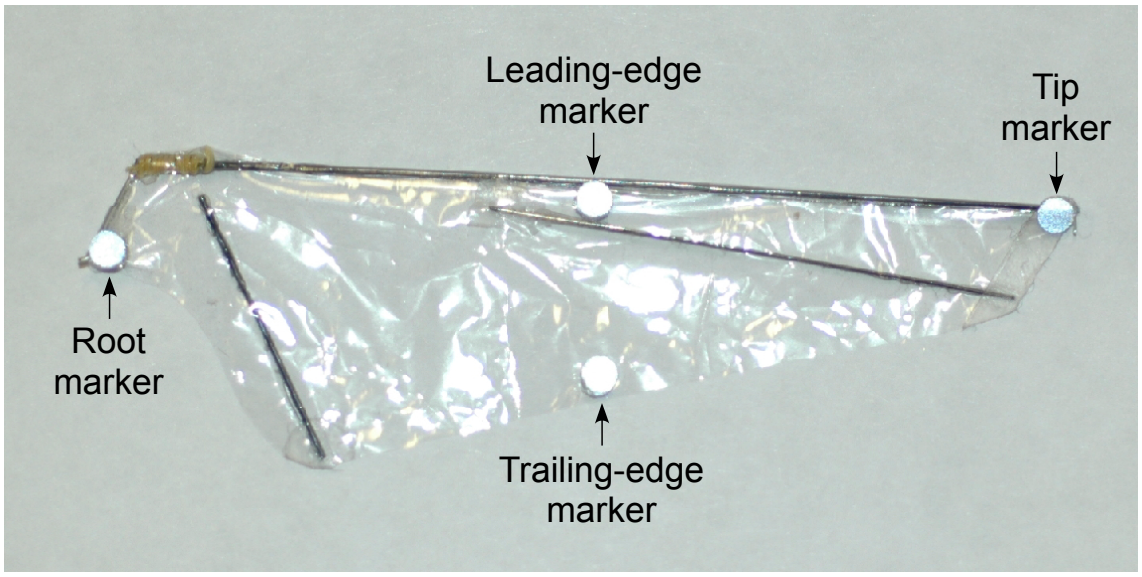

Figure 2.3: Markers placed on the wing for motion capture testing.

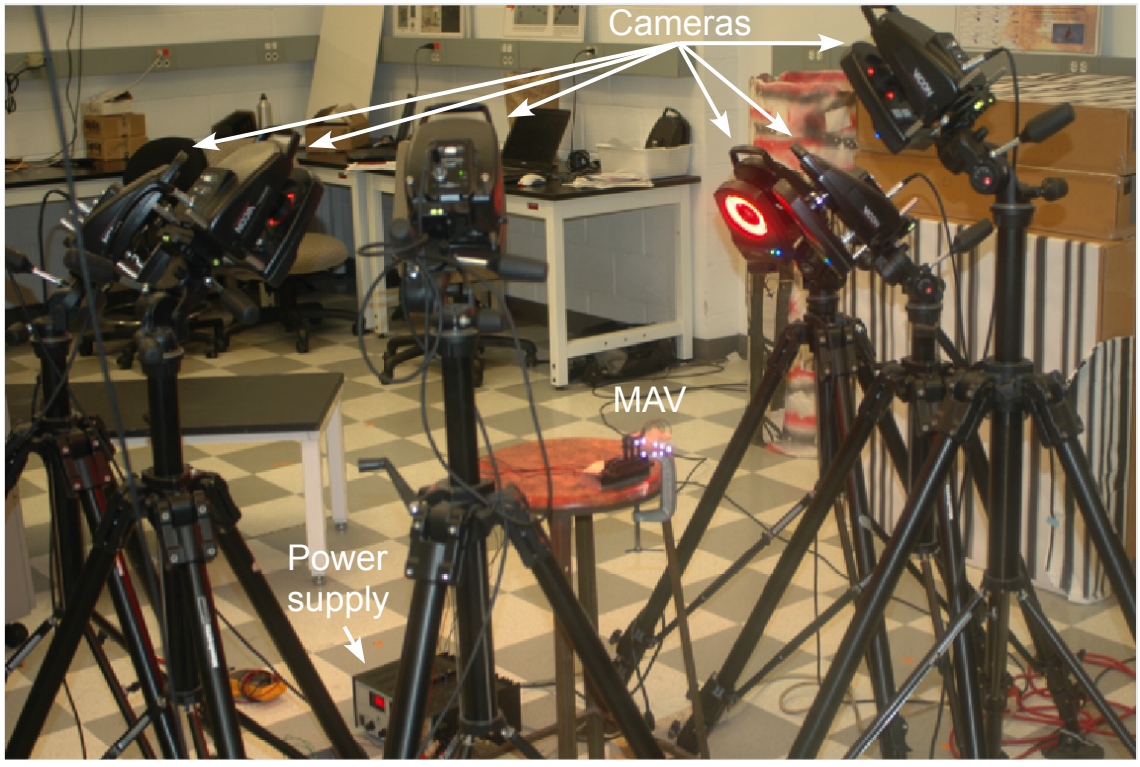

Figure 2.4: Motion capture system setup in the laboratory.

span locations. Markers were placed at the root and tip of the wing to provide the software with a reference axis, and markers were placed at the leading edge and trailing edge of the wing at six span locations to track the pitch displacement. This setup gave measurements where no more than four markers were used on the wing at a time, minimizing the impact of the weight of the markers on the motion and the aeroelastic deformation of the wing. Figure 2.3 shows the placement of the markers on the wing.

Seven cameras were strategically placed around the wing at different heights and angles to track the markers as they translated and pitched throughout the wing stroke. Figure 2.4 shows the placement of the cameras around the flapping-wing test rig, with the seventh camera (not shown) being mounted on the ceiling. After the raw data were captured, marker reconstruction and processing provided the complete time-history of the three-dimensional location of each marker. The wing velocities and accelerations, and the pitch and stroke angles of the wing, were then obtained throughout the wing stroke. Experiments were conducted at wing flapping frequencies of 17 Hz and 25 Hz.

2.4 Time-Resolved Flow Visualization (TR-FV)

The complex, unsteady, three-dimensional flow produced by the flapping wing was first qualitatively studied using high-speed imaging of the flow field. Specific interest in this case was in the formation, convection, and shedding of the leading-edge vortex (LEV) from the upper surface of the wing during its stroke.

Time-resolved flow visualization (TR-FV) allowed for the temporal tracking of unsteady flow structures throughout the wing stroke. The images were captured with the

camera viewing axis orthogonal to the plane of a laser sheet. This approach allowed imaging of slices of the flow across the chord or span of the wing. A high-speed CMOS camera was used in conjunction with a high-speed Nd:YLF laser to capture the images. The CMOS camera was able to capture images at a maximum rate of 3,000 fps with a pixel resolution of 1,024-by-1,024 pixels (1 MP). The Nd:YLF laser emitted light at a wavelength of 527 nm with 20 mJ per pulse. Given the large number of high-resolution images being transferred to the data acquisition system in a relatively short time, a hyper-streaming system was used to provide a temporary data buffer before the images were sent to the data acquisition system.

During the TR-FV, the flow field was heavily seeded with particles to track individual flow structures as well as the flow field as a whole. A smoke generator was used to produce these submicron seed particles. Inside the generator, high pressure nitrogen was mixed with a mineral oil solution, which was then vaporized after being heated to its boiling point. As the vapor left the nozzle it mixed with the air of the room, producing a dense white smoke containing the tracer particles. These seed particles were passed through a plenum and honeycomb structure under the influence of a weak pressure gradient, which helped to remove most of the larger turbulence and eddies from entering the test section.

For the present TR-FV measurements, the frame rate of the camera was chosen to be 1,500 fps. There was a trade-off between the frame rate and laser intensity because at higher frame rates there was less time for the camera to capture the available light energy. Therefore, at a very high frame rate the camera captures darker images, which can sometimes be unusable for analysis. A frame rate of 1,500 fps was found to be optimal between balancing temporal resolution and image intensity. For each data capture run,

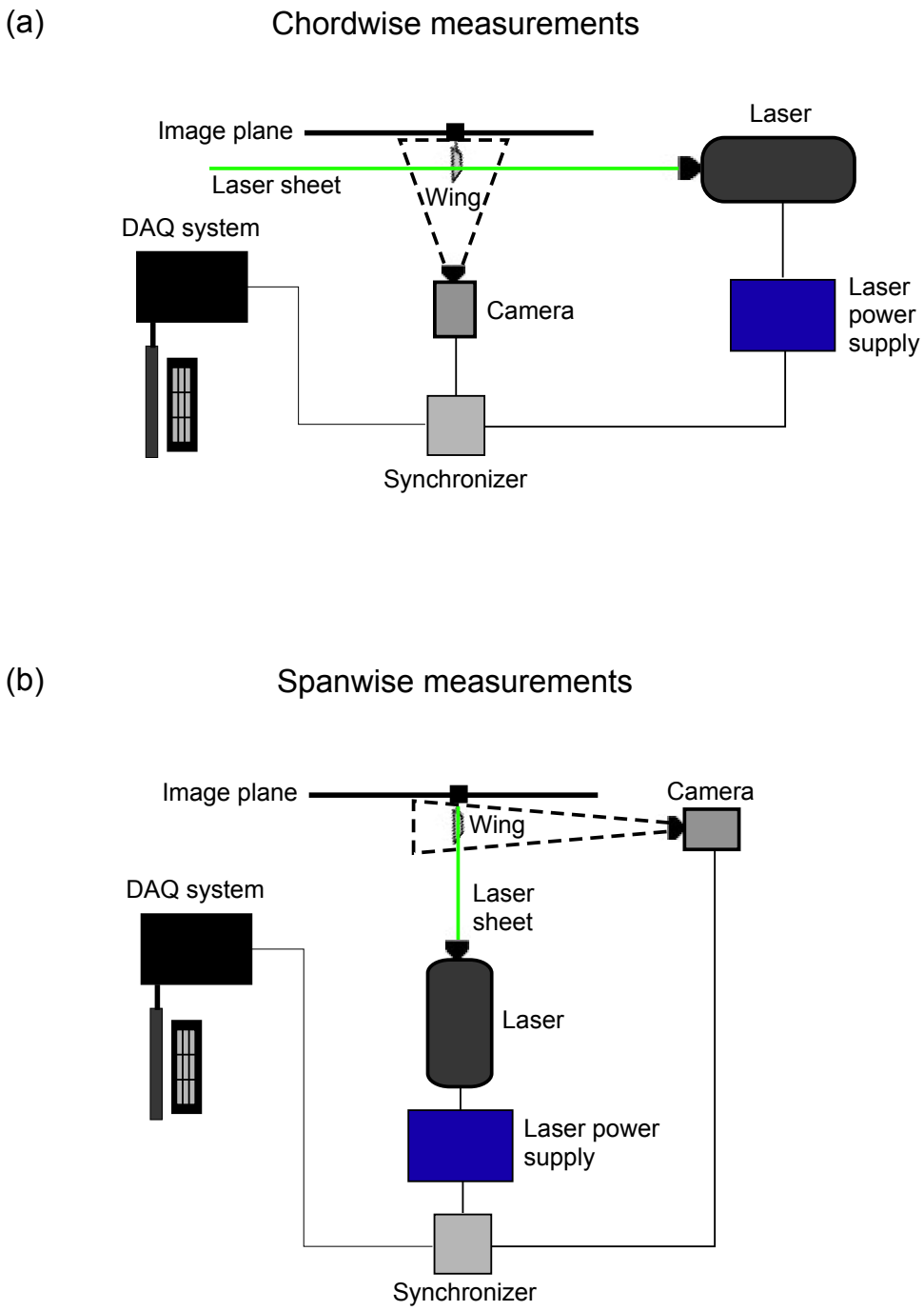

Figure 2.5: Setup of the laser and camera configurations for: (a) chordwise flow measurements, (b) spanwise flow measurements.

250 sequential images were taken, which corresponded roughly to 2.5 wing strokes and approximately one image per 2.8° of wing stroke. TR-FV images were taken in several planes, as shown in Fig. 2.5, which identifies a plane across the chord of the wing (chord-wise measurements) and a plane across the span of the wing (spanwise measurements).

2.5 Particle Image Velocimetry (PIV)

While the TR-FV revealed a qualitative time-history of the flow features present in the flow of the flapping wing, particle image velocimetry (PIV) was used to provide quantitative, two-dimensional velocity field measurements to better understand the aero-dynamic environment. Two types of PIV were utilized during these tests: 1) Phase-resolved PIV (PR-PIV), and 2) time-resolved PIV (TR-PIV). Both of these measurement techniques are detailed in the following sections.

2.5.1 Principles of PIV

PIV is a non-intrusive flow measurement technique that measures a planar velocity field over a designated region of interest. The flow is uniformly seeded with submicron tracer particles, which serve to track the flow. A planar laser light sheet is placed in the region of interest to illuminate the particles, and a digital camera is oriented orthogonally to the light sheet. The camera is uniformly focused over the region of interest. The seeded flow field is then illuminated twice within a small pulse separation time, Δt, which is of the order of microseconds. The camera is then digitally synchronized with the laser and camera to capture the two successive images.

The pair of images contains the pixel displacement of the particles for the selected pulse separation time. First, the images are divided into smaller interrogation windows, which for the present experiments were 24-by-24 pixels in size. A cross-correlation procedure was used to match the intensities of the particles between the two images within each small window, and then computes the magnitude and direction of the pixel displacement $(\Delta x, \Delta y)$. This process was performed utilizing a Fast Fourier Transform (FFT) algorithm in the frequency domain [40,41]. A deformation grid algorithm was utilized to improve particle correlation, and details of this cross-correlation technique are given in Appendix A. Once the pixel displacement was found, the local velocity can be calculated using the equation

$$\left\{ \begin{array}{c} U \\ V \end{array} \right\} = \frac{1}{M\Delta t} \left\{ \begin{array}{c} \Delta x \\ \Delta y \end{array} \right\} \tag{2.1}$$

where M is the image magnification. The image magnification was calculated within the PIV software from a master image with a scale placed in the laser plane to calibrate the ratio of pixels to millimeters. The cross-correlation process was then repeated for all interrogation windows within the image, the outcome being a planar velocity field. Figure 2.6 outlines this process. Additional information about this PIV technique can be found in Refs. [42–45].

2.5.2 Phase-Resolved PIV (PR-PIV)

In the present work, the PR-PIV was utilized to acquire the velocity fields to make a determination of the circulatory components of lift and drag components acting on the flapping wing. To accomplish this goal, the light from the Nd:YAG laser was passed

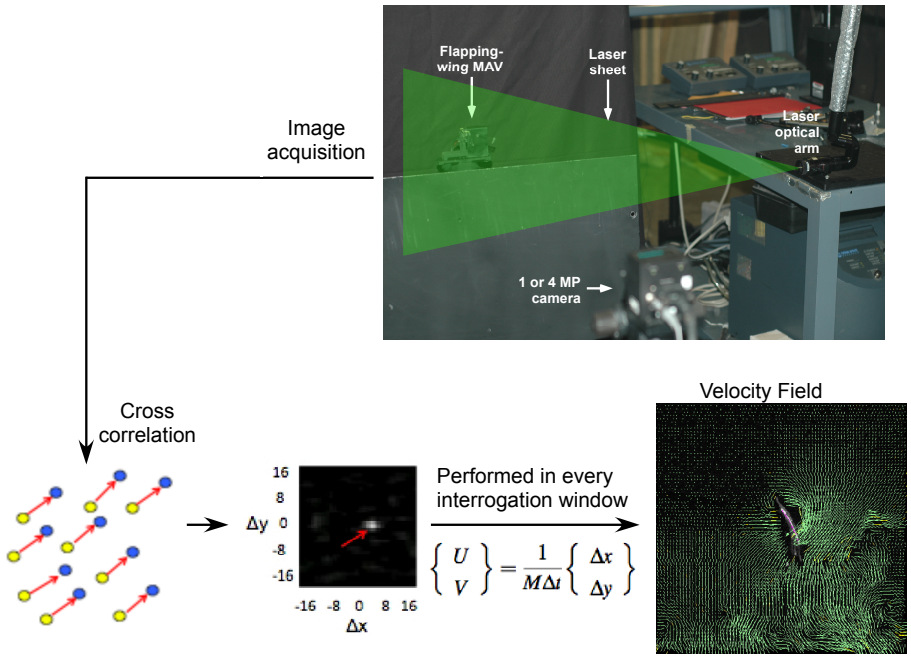

Figure 2.6: Schematic of PIV setup and image processing methodology.

through a cylindrical lens to obtain the planar light sheet. The seeding was distributed to best achieve a uniform dispersion of particles, as well as to provide a sufficiently large number of particles to successfully perform the cross-correlation. In this case, a 4-megapixel (4 MP) resolution CCD camera was used to capture the particle images, which was synchronized to the laser using a timing hub. A Hall-effect sensor produced a once-per-cycle trigger to measure the flapping frequency of the MAV, which was also connected to the synchronizer.

The pulse separation time, Δt, between the image pair was set to 60 μs for the measurements made at a flapping frequency of 17 Hz, and to 40 μs for measurements at a flapping frequency of 25 Hz. The pulse separation time was decreased for the 25 Hz case to compensate for the increased flow velocities and to ensure that the particles did not

displace by more then 25% within the 24-by-24 interrogation window between the two PIV frames. Spurious vectors were determined using a Gaussian peak with a stringent signal-to-noise ratio of 1.5.

The PR-PIV was utilized to capture chordwise flow measurements, as shown in Fig. 2.5. These measurements were performed at six span locations of 30%, 50%, 60%, 70%, 80% and 90% span, two flapping frequencies of 17 Hz and 25 Hz, and six stroke angles in increments of 20° during the translational strokes. The velocity fields were then analyzed and used to estimate the aerodynamic forces acting on the wing.

2.5.3 Time-Resolved PIV (TR-PIV)

TR-PIV is based on the same principles as PR-PIV but is used to capture the planar velocity fields as a continuous time-history. This system utilizes the same high-speed laser and camera setup that was discussed in Section 2.4. The frame rate of the high-speed CMOS camera was kept at 1,500 fps for TR-PIV, and 250 sequential PIV images were captured during each run. Both chordwise and spanwise measurement planes were recorded using the TR-PIV system.

While temporal resolution is the main benefit of using the TR-PIV system, there is some loss in spatial resolution compared to the PR-PIV system. Because of the high repetition rate of the TR-PIV laser and camera setup, the system needs to stream large amounts of data over very short periods of time. The high-speed camera is limited to a resolution of 1 MP by the transfer rate limits of the hyper-streaming system. In contrast, PR-PIV features a low repetition rate, but in this case allows for the use of a 4 MP camera

for imaging.

2.6 Challenges of Making Flapping-Wing Flow Measurements

Acquiring flow measurements on a flapping wing presented several unique challenges. In general, setting up PIV requires the careful alignment of the camera viewing axis to the laser light sheet plane. If the camera is misaligned with respect to the light sheet, only part of the image will be in focus. This problem can increase the error in the cross-correlation process, as well as affect the sub-pixel accuracy. In particular, intense reflections from the clear Mylar covering the wing planform made the cross-correlations near the wing surface virtually impossible. These reflections were somewhat reduced by the appropriate selection of camera aperture setting and laser intensity level. The presence of the mechanism in the background of the PIV images also interfered with the particle correlation process, but this problem was largely mitigated by pre-processing using background subtraction. This latter technique involved generating a composite minimum intensity image, which was then subtracted from each individual PIV image. There were also some initial issues with laser shadowing in regions of the flow, but a careful orientation of the laser sheet relative to the wing largely alleviated this problem.

Because of the aeroelastic deformation of the wing during its stroke, fatigue of the aluminum joint required periodic replacement of the wings. The carbon rod ends would initially tear the Mylar after approximately 30 minutes of experimentation. This problem was resolved by replacing pieces of tape at the end of the rod with larger pieces, which served to better spread the stresses at this location. This solution roughly doubled the life

of the wing.

2.7 Errors in Motion-Tracking Measurements

Given the size of the retroreflective markers (they were 3.5 mm in diameter) and the relative proximity of the motion capture camera system to the flapping wing, it was estimated that the error in the spatial tracking of the markers was approximately 2.8% of the measured displacements. This resulted in an error of approximately 4.4% in the calculated values for the sectional noncirculatory lift coefficient. It was also estimated that there was a 2.5% error in the measured values for the sectional noncirculatory mid-chord moment coefficient.

2.8 Errors in Flow Measurements

Uncertainties in the PIV measurements result from the size and density of the tracer particles (i.e., tracking errors), the degree of background noise, the size of the interrogation windows, amongst other sources [10, 46]. For the current PIV experiments, the error in the pixel displacements used in the calculation of the velocity fields was approximately 3.3%. The combined uncertainties of the noncirculatory and circulatory sectional lift resulted in an error estimate of 5.6% in the values of the total sectional lift coefficient. For the sectional drag measurements, the uncertainty here was lower because it was computed solely from the PIV velocity fields, resulting in an estimated error of 2.5%. The combination of these errors resulted in an error estimate of about 6% in the measurements of the section and wing lift-to-drag ratios.

2.9 Summary

This chapter has discussed the experimental methods utilized in the present work. The flapping-wing test rig and its setup have been described. The motion capture system allowed for the measurement of the wing kinematics, and the components of the system were explained. The present work utilized time-resolved flow visualization (TR-FV) to qualitatively analyze the unsteady, complex aerodynamics. Phase-resolved particle image velocimetry (PR-PIV) and time-resolved particle image velocimetry (TR-PIV) were used to acquire velocity field measurements in several planes. The fundamental principles of PR-PIV and TR-PIV have been explained, in addition to the experimental equipment used in each setup. Several challenges of performing flow measurements on a flapping-wing MAV were also described.

Chapter 3

Results and Discussion

3.1 Introduction

This chapter presents the results of the experiments that were conducted, which are discussed in some detail. The flow visualization (FV) was used to make qualitative images of the evolution of unsteady flow structures in the flapping-wing flow field. The particle image velocimetry (PIV) measurements quantified these flow structures and the surrounding flow field. Results of the motion tracking experiment helped to quantify the complicated kinematics of the flexible wing, and allowed for the calculation of the non-circulatory forces and moments acting on the flapping wing. The velocity fields obtained from PIV were utilized to compute the circulatory forces acting on the flapping wing.

3.2 Time-Resolved Flow Visualization Results

3.2.1 Introduction

The FV results provided insight into the complex, unsteady, three-dimensional flow inherent to the flapping wing. The temporal resolution possible with this setup allowed for a detailed analysis of the flow structures in the unsteady flow field. As explained in Chapter 2, the time-resolved flow visualization (TR-FV) measurements were performed in both chordwise and spanwise planes. Chordwise measurements were performed at sev-

eral span locations and stroke positions to examine the formation and shedding process of the LEV. For the spanwise measurements, the light sheet was arranged so as to illuminate a plane along the span of the wing. These measurements provided velocity fields in the cross-plane of the near-wake, and helped to show the evolution of the root and tip vortices that were trailed from the wing.

3.2.2 Chordwise Time-Resolved Flow Visualization

The chordwise TR-FV measurements imaged the temporal evolution of several structures in the flow, including the LEV formation as it developed on the upper surface of the wing. Figure 3.1 shows the evolution of the flapping-wing flow field during a representative downstroke; the wing has been outlined (in red) in these images.

The flapping phase angle, Ψ, was used to relate the location of the wing during its wing stroke. One wing stroke has an angular range from 0° to 360°. In the present work, 0° corresponds to the maximum stroke angle of the wing during pronation, and 180° corresponds to the maximum stroke angle during supination.

It is well known that a starting vortex forms at the trailing edge of an airfoil when it is impulsively accelerated from rest [14]. For reciprocating flapping-wing motion, this process occurs during pronation and supination when the wing temporarily stops and changes its direction of motion. In Fig. 3.1 b), a starting vortex of counter-clockwise circulation was seen to form at the trailing edge of the wing after pronation. This starting vortex subsequently slowly convected below the stroke plane and ultimately diffused into the downstream wake, as shown in Fig. 3.1 i).

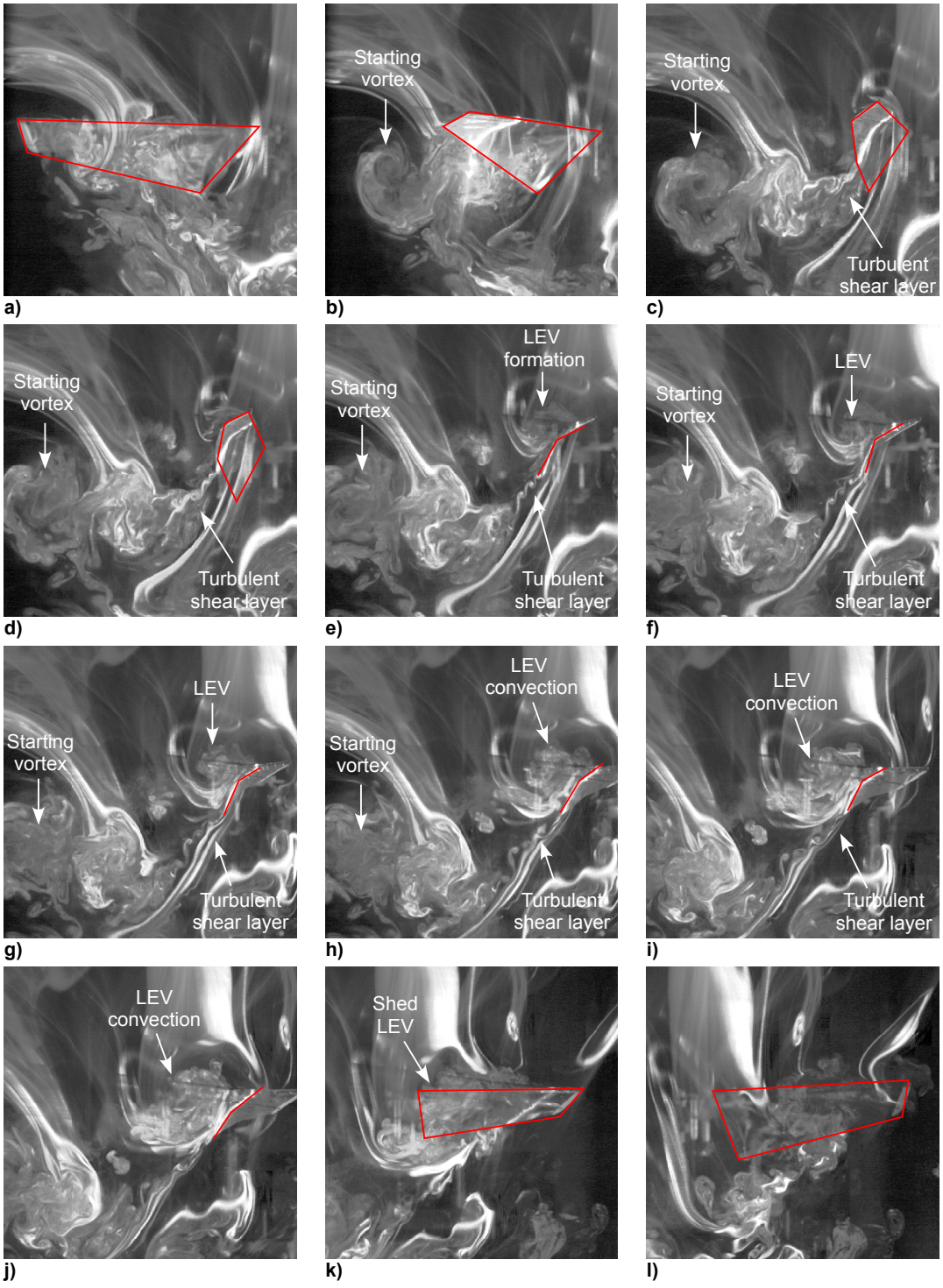

Figure 3.1: Chordwise TR-FV measurements at mid-stroke: a) Midpoint of pronation, Ψ = 0°; b) Ψ = 45°; c) Ψ = 67°; d) Ψ = 72°; e) Ψ = 84°; f) Ψ = 90°; g) Ψ = 95°; h) Ψ = 102°; i) Ψ = 108°; j) Ψ = 115°; k) Ψ = 138°; l) Midpoint of supination, Ψ = 180°.

As shown in Figs. 3.1 c)–i), a turbulent shear layer can be seen to form at the trailing edge of the wing during the wing stroke. Small eddies of alternate signs comprised this turbulent shear layer, which was generated throughout the translational stroke. Each translational stroke deposited a new layer of vorticity into the wake.

Figure 3.1 shows the formation, growth and shedding process of the LEV throughout the downstroke. This process is shown in greater detail in Fig. 3.2. At the beginning of downstroke in Fig. 3.2 a), the LEV has not formed on the upper surface. As the wing pitches up through mid-stroke, the formation of the LEV is shown in Fig. 3.2 c). The LEV then grows in size at the leading edge in Fig. 3.2 d) as the wing continues to pitch up. Figure 3.2 e), shows that the LEV convects down the chord of the wing. By the end of the downstroke, the LEV has been shed off the wing into the wake.

The flow structure of the LEV along the wing span was characterized by capturing TR-FV images at two additional locations at 25% and 75% span. Figure 3.3 compares the TR-FV results at the three span locations through the downstroke. Note that at 25% span, the LEV formation, growth and convection process is similar to the process seen at 50% span. The LEV forms at mid-stroke, grows in size as the wing translates, and then convects over the chord. At 75% span, however, there is no evidence of LEV formation at any point during the wing stroke; there is only evidence of separated flow at 75% span, as shown in Fig. 3.3 e).

Chordwise TR-FV images were acquired during the pronation of the wing to observe the flow features at the end of a half-stroke. Figure 3.4 shows measurements from the end of the upstroke to the beginning of its downstroke. In Fig. 3.4 b), the LEV has been shed from the wing at the end of the upstroke as the wing begins to decelerate and

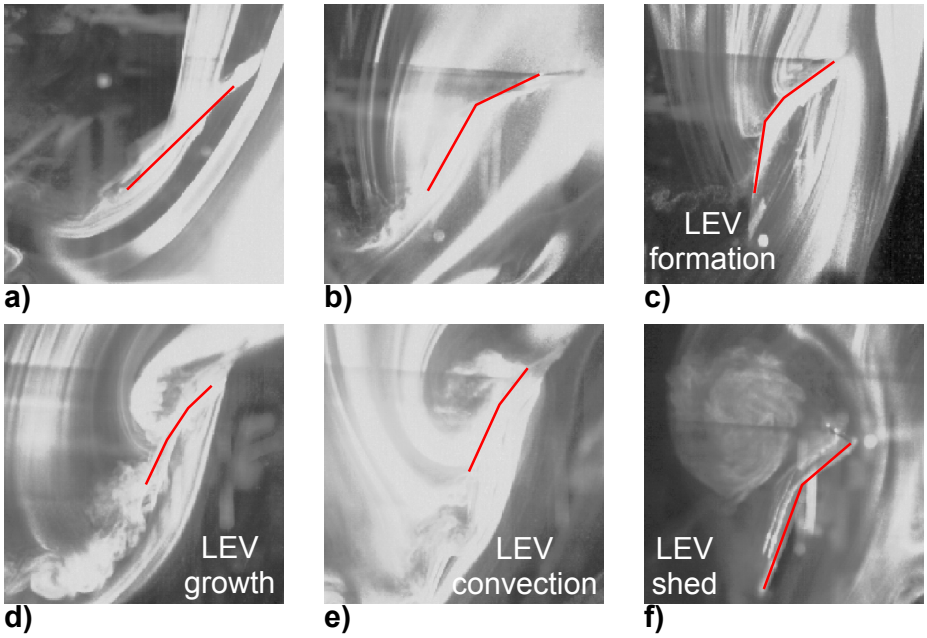

Figure 3.2: Chordwise TR-FV results at 50% span: a) $\Psi = 38°$; b) $\Psi = 77°$; c) LEV formation, $\Psi = 90°$; d) LEV growth, $\Psi = 102°$; e) LEV convection, $\Psi = 114°$; f) LEV shedding, $\Psi = 141°$.

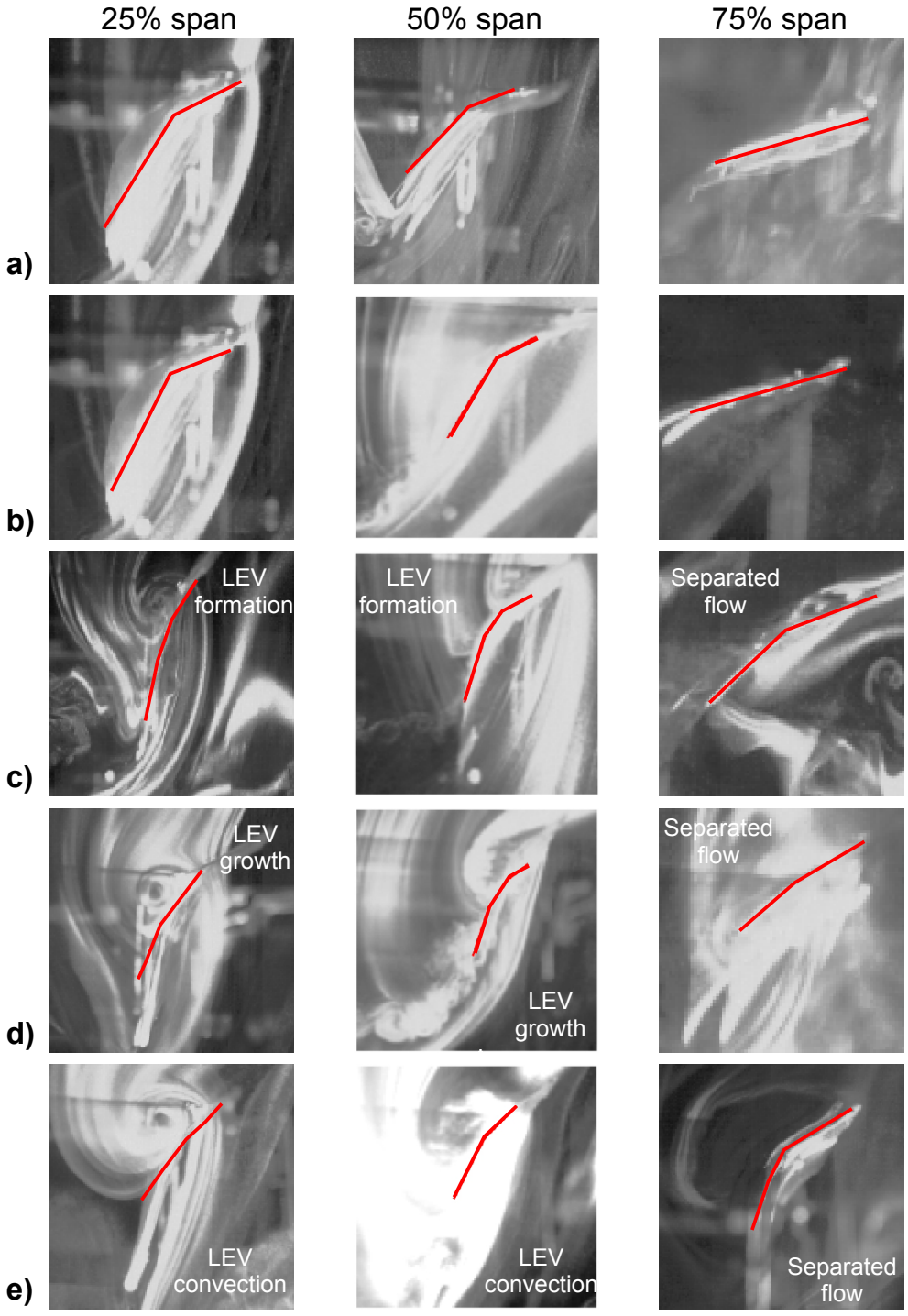

Figure 3.3: Chordwise TR-FV results at 25%, 50% and 75% span: a) $\Psi = 54°$; b) $\Psi = 77°$; c) $\Psi = 90°$; d) $\Psi = 102°$; e) $\Psi = 114°$.

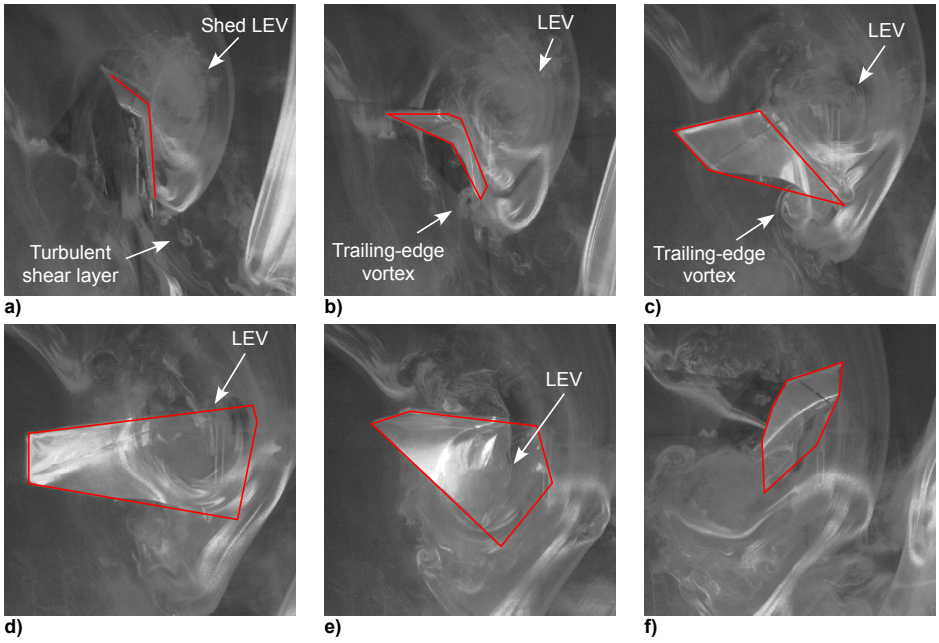

Figure 3.4: Chordwise TR-FV results at wing pronation: a) $\Psi = 326^\circ$; b) $\Psi = 336^\circ$; c) $\Psi = 348^\circ$; d) $\Psi = 0^\circ$; e) $\Psi = 14^\circ$; f) $\Psi = 24^\circ$.

pronate. The LEV begins to diffuse into the wake as the wing begins to pronate, as shown in Fig. 3.4 d). The wing then completes its pronation and cuts through the shed LEV at the beginning of its downstroke.

The foregoing wing-vortex interaction can enhance lift generation on the wing through a physical mechanism known as wake capture, which has been discussed in Chapter 1. In previous research, a rigid flapping wing has been shown to translate through a LEV shed from the wing in the previous stroke [36]. In the present case, the flapping wing also cuts through the shed LEV as the wing starts its downstroke.

Figures 3.4 c) and 3.4 d) show the development of a small vortical flow structure at the trailing edge of the wing. This vortex forms as a result of the rollup of the turbulent shear layer during the deceleration and pronation of the wing. This phenomenon has also

been observed in previous research on flapping-wing mechanisms [36].

3.2.3 Spanwise Time-Resolved Flow Visualization

This section details the TR-FV measurements taken along the span of the wing where the laser was aligned to the mid-chord of the wing. Figure 3.5 shows spanwise TR-FV images during one flapping cycle, commencing and concluding with an image at the midpoint of the upstroke.

In Fig. 3.5 b), a root and tip vortex pair shed from the previous wing stroke is shown in the wake. After the wing has passed through the midpoint of the upstroke, a pair of root and tip vortices are trailed into the wake, shown in Fig. 3.5 d). At this point in the wing stroke, the root and tip vortex pair from the previous stroke have convected further into the wake. After the wing has traveled a full half-stroke, the root and tip vortex pair from the previous stroke fully diffuse into the wake, as shown in Figs. 3.5 e) and 3.5 f). As shown in Fig. 3.5 e), a secondary tip vortex emerges from the tip of the wing. However, this vortex flow was not imaged during every half-stroke and appears to be an aperiodic phenomenon. The process of root and tip vortex generation, convection and diffusion repeats itself, as shown in Figs. 3.5 g) and 3.5 h).

When tracking the position of the root vortex in Fig. 3.5 b)–d) and Fig. 3.5 f)–g), the root vortex appears to convect more quickly downward through the wake in comparison to the tip vortex. This outcome likely occurs because of the relative strength of the tip vortex compared to root vortex, this behavior being further examined using the TR-PIV measurements that will be discussed in Section 3.3.

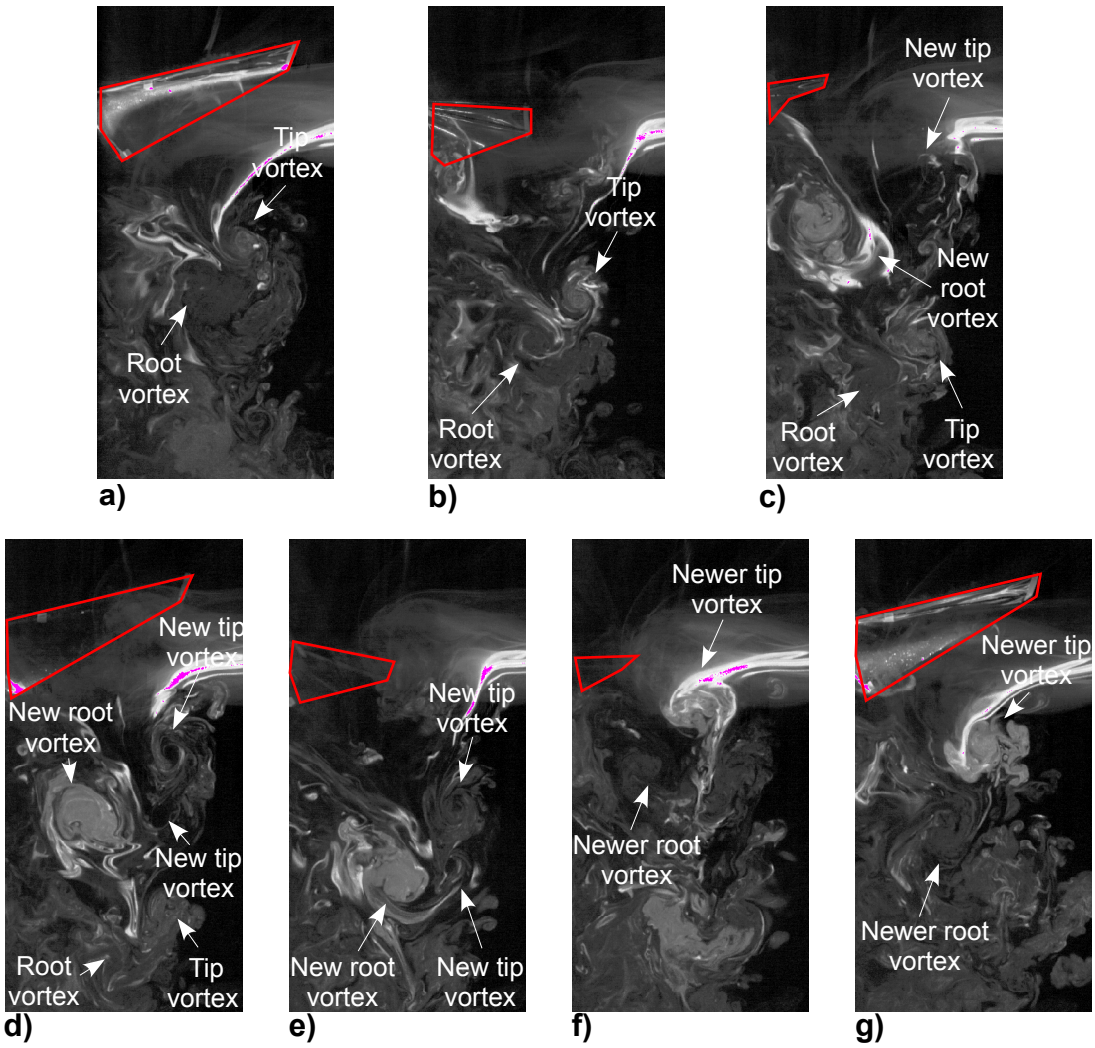

Figure 3.5: Spanwise TR-FV results: a) $\Psi = 326°$; b) $\Psi = 336°$; c) $\Psi = 348°$; d) $\Psi = 0°$; e) $\Psi = 2°$; f) $\Psi = 14°$; g) $\Psi = 24°$.

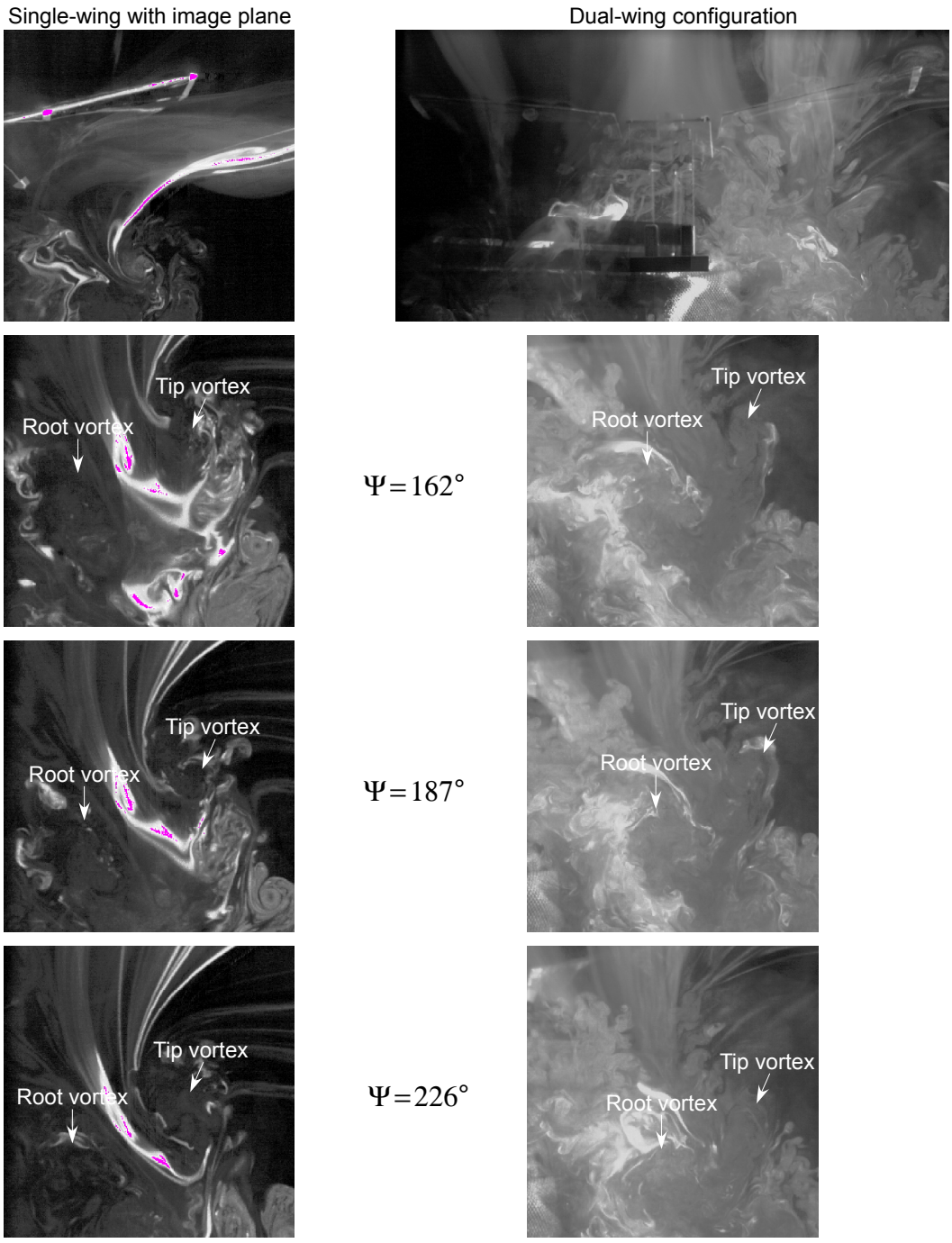

Figure 3.6: Spanwise FV measurements made on a single-wing configuration with a vertical image plane and a dual-wing configuration.

FV measurements in the spanwise plane for this single-winged setup were compared to FV measurements made on a dual-winged test rig setup, as shown in Fig. 3.6. The presence of the image plane enforces flow symmetry in the single-wing setup. When comparing the wake system of the two setups, it was shown that the root and tip vortices have similar formation and convection characteristics throughout the wing stroke. These measurements justify testing on a single-wing with the use of a image plane as a representation of a dual-winged device.

3.2.4 Summary

This section has shown some of the FV measurements that were taken of the flow field of the flapping wing. High-speed videography allowed for time-accurate tracking of the various flow structures as they evolved in the complex, unsteady flow field. Chordwise FV showed the presence of a starting vortex after pronation and supination in the wake, and it also showed a turbulent shear layer emerging from the trailing edge of the wing during its translational stroke. The sequence of LEV formation, convection, and shedding was imaged and was found to mimic the process of classic dynamic stall. Spanwise FV results revealed the formation of a root and tip vortex pair, where the root vortex was shown to qualitatively convect through the wake more quickly than the tip vortex.

3.3 Time-Resolved Particle Image Velocimetry (TR-PIV) Results

3.3.1 Introduction

Velocity field measurements of the flow field generated by the flapping wing were acquired using TR-PIV. Most of the results were obtained at a flapping frequency of 17 Hz. These measurements helped to quantify the flow field during the entire flapping cycle in both the chordwise and spanwise planes.

3.3.2 Time-Resolved Particle Image Velocimetry in Chordwise Planes

Chordwise TR-PIV measurements were acquired during the wing stroke with the laser sheet aligned at 25% and 50% span. A comparison of the instantaneous velocity fields taken at these span locations is shown in Fig. 3.7. The contours in the plot are based on the vertical component of the total velocity, with red representing an upwash and blue representing a downwash. At the 25% and 50% span locations, the maximum downwash velocity was measured to be 4.7 and 4.8 ms^{-1}, respectively. These velocities were noted to be approximately half of the average tip velocity.

The presence of the starting vortex is well shown at both span locations in Fig. 3.7. The vortex strength can be characterized by its peak swirl velocity, which is the maximum velocity present in the vortex. The peak swirl velocity of the shed starting vortex was approximately 1.8 ms^{-1} at 25% span location. In comparison, the peak swirl velocity at 50% span location was almost 4.1 ms^{-1}. The difference in peak swirl velocity between the two span locations largely arises from differences in the local section velocities, which

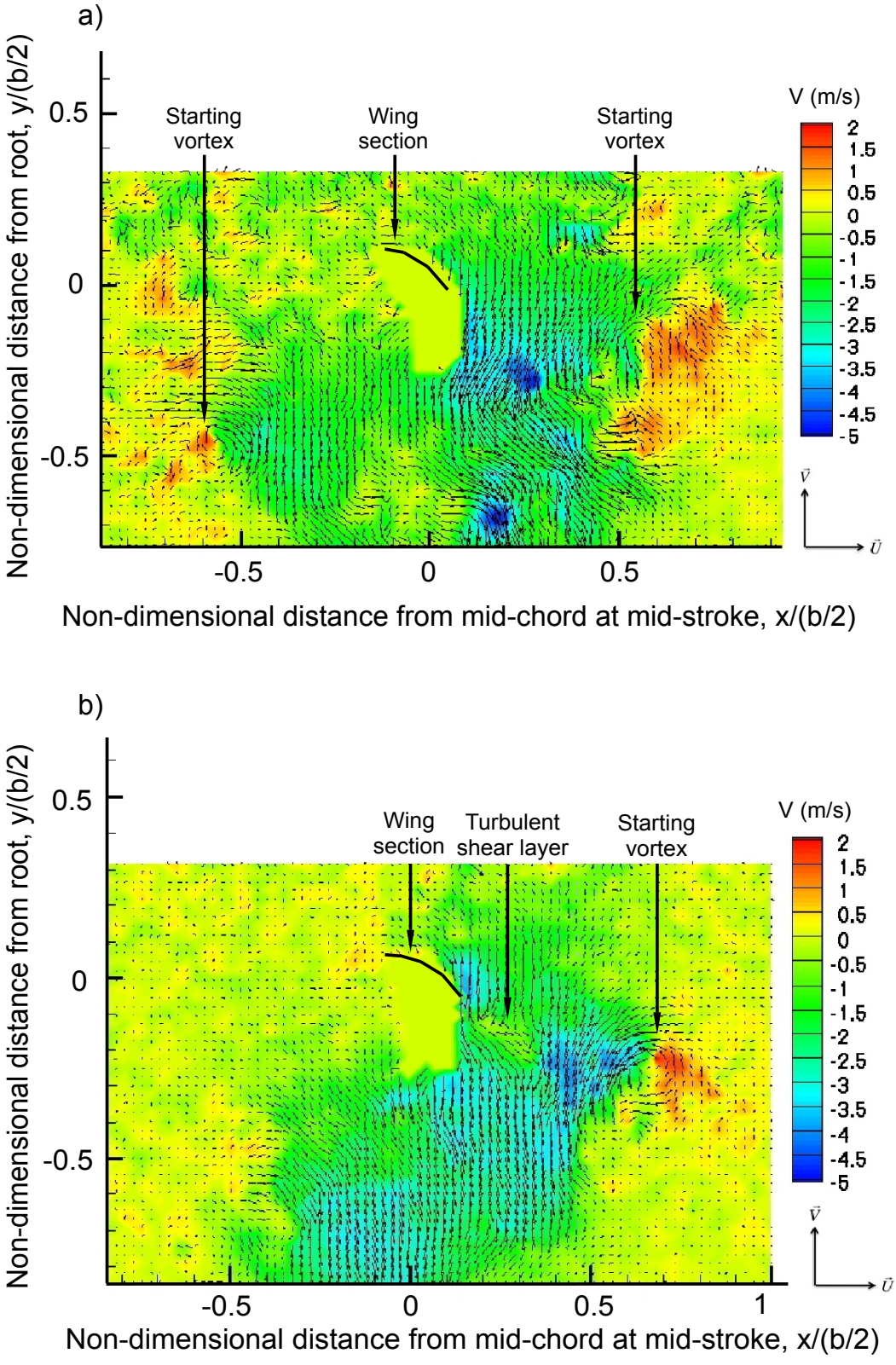

Figure 3.7: Chordwise PIV results at midstroke: a) 25% span; b) 50% span.

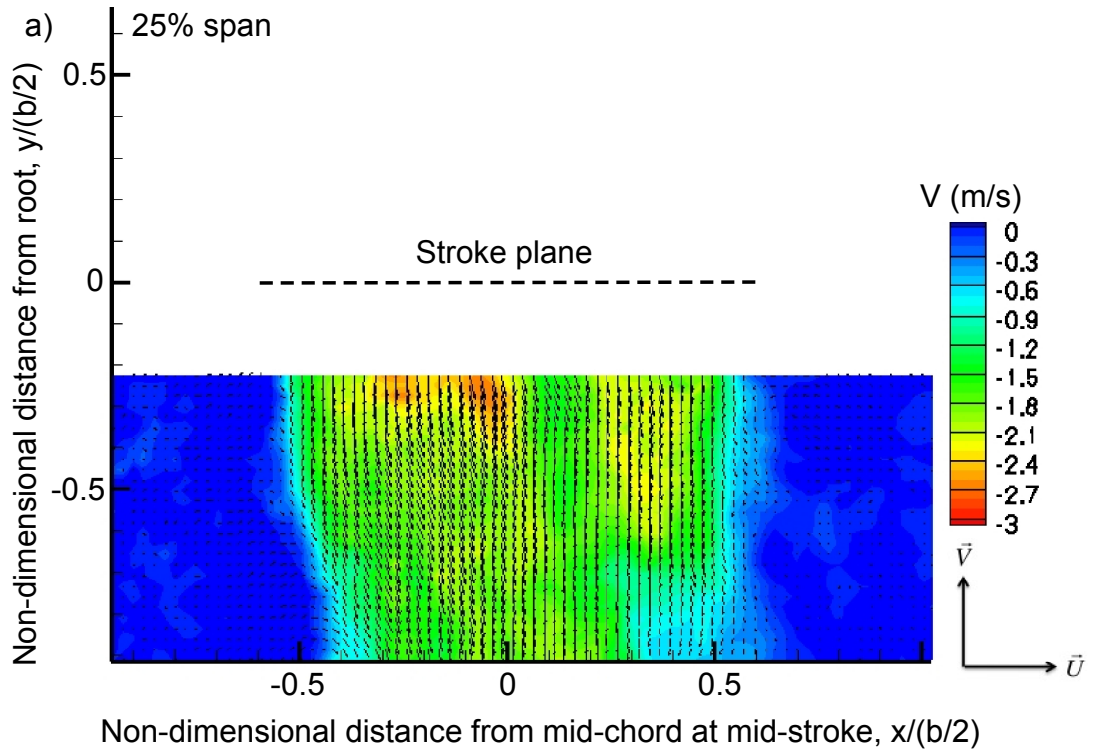

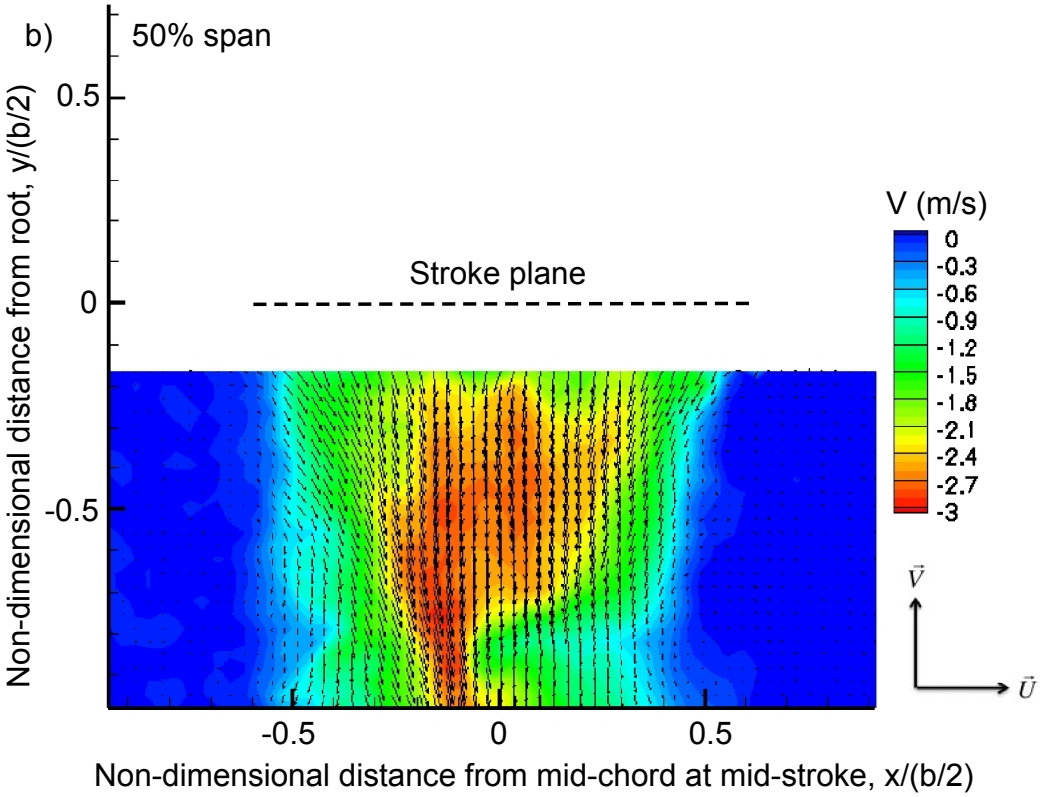

Figure 3.8: Time-averaged wake in the chordwise plane over one flapping cycle at: a) 25% span; b) 50% span.

leads to lower lift production at the inboard locations.

The temporal resolution of the TR-PIV setup allowed for time-averaging of the instantaneous PIV images. Approximately 100 images were captured and then averaged over one flapping cycle at 25% and 50% span. Figure 3.8 shows the time-averaged flow field where the contours represent the vertical velocities. The maximum vertical downwash in the averaged near-wake field at 25% span was approximately 2.7 ms^{-1}, and at 50% span was 3 ms^{-1}. Comparing Fig. 3.8 a) and 3.8 b), greater velocities persist farther into the wake at 50% span. The contours in Fig. 3.8 also show an increase in vertical velocity in the wake of the flapping wing. Because of continuity considerations, the area enclosed by the slipstream must decrease and wake contraction is shown in Fig. 3.8 at both 25% and 50% span. There is a change in the momentum of the fluid in the vertical direction, which results in a force on the wing.

3.3.3 Time-Resolved Particle Image Velocimetry in Spanwise Planes

The TR-PIV measurements in spanwise planes were acquired along the mid-chord of the wing during the wing stroke. The orientation of the light sheet allowed for a quantitative analysis of the root and tip vortex as they were shed from the wing into the near-wake. An instantaneous velocity field of the near-wake in this plane is shown in Fig. 3.9. At the midpoint of the downstroke, the root and tip vortex were found to have peak swirl velocities of 20% and 28% of the maximum wingtip velocity, respectively. These values for peak swirl velocity at this point in the flapping cycle are similar to those measured on a previous flapping-wing mechanism by Ramasamy and Leishman [6].

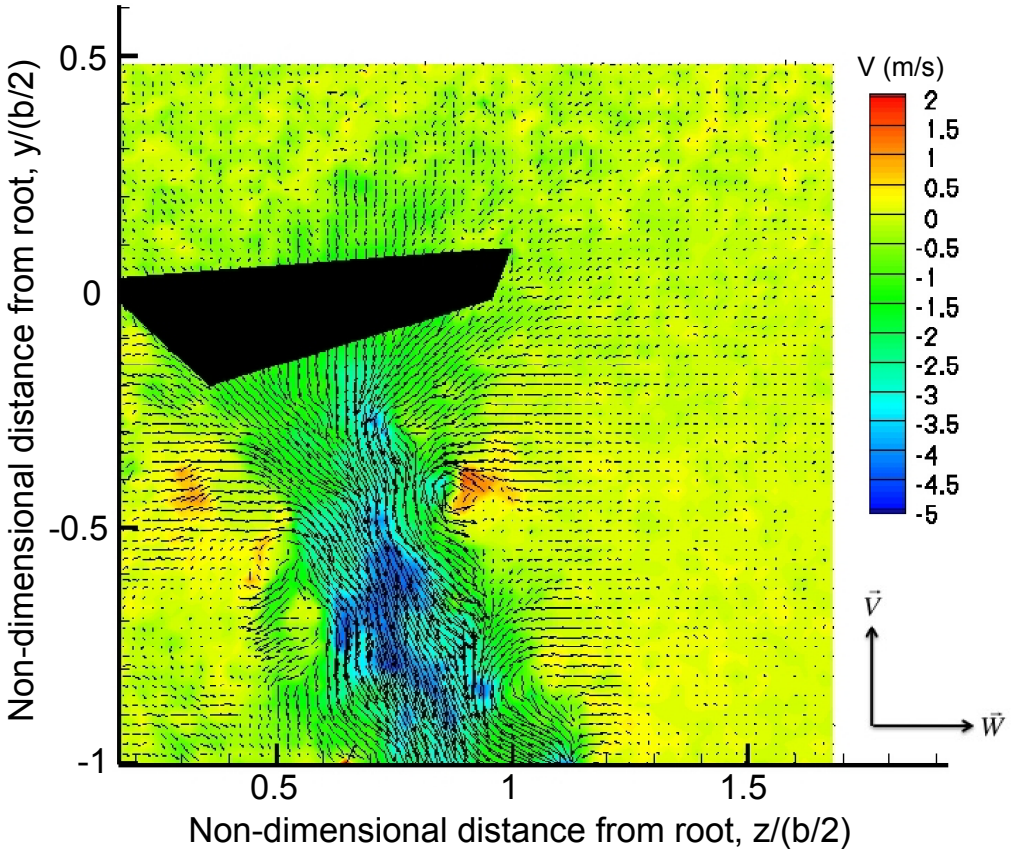

Figure 3.9: Spanwise PIV taken at the midpoint of the upstroke ($\Psi = 180°$) with the laser sheet aligned along the mid-chord of 50% span.

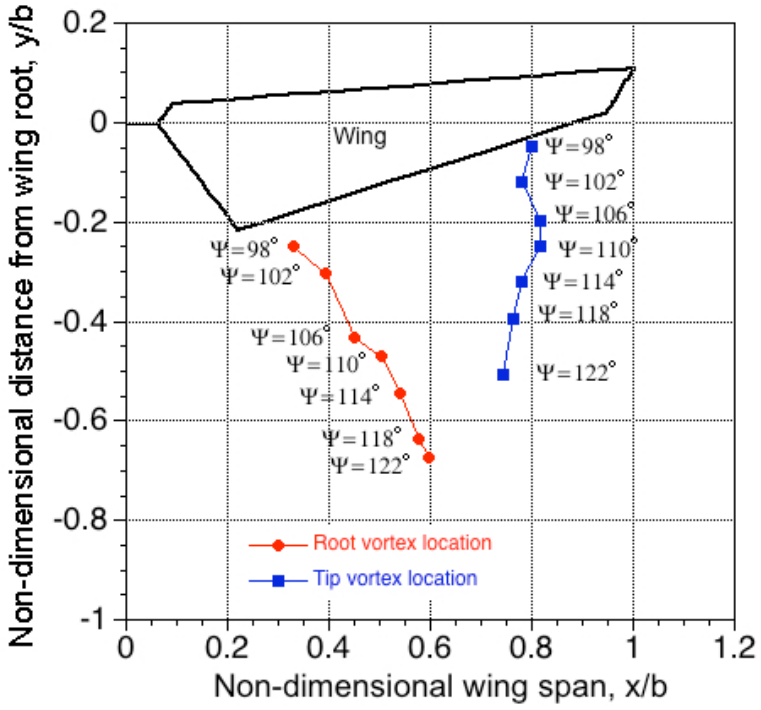

Figure 3.10: Locations of the root and tip vortices in space and time in the wake throughout the wing stroke.

To provide a more precise representation of the relative positions of the root and tip vortex, spanwise TR-PIV measurements were used to track the location of the root and tip vortex during the entire wing stroke, as shown in Fig. 3.10. These results show that the root and tip vortices convect toward one another in the near-wake to form a contracting wake structure.

The measured velocity fields were used to compute the circulation of the root and tip vortex to measure their relative strength. This process was performed by utilizing the circulation-box method, which will be explained in greater detail in Section 3.5.2. When the root and tip vortex pair had convected into the wake such that they were 16° old, the circulation of the root vortex was measured to be 0.1381 m^2s^{-1} and the corresponding

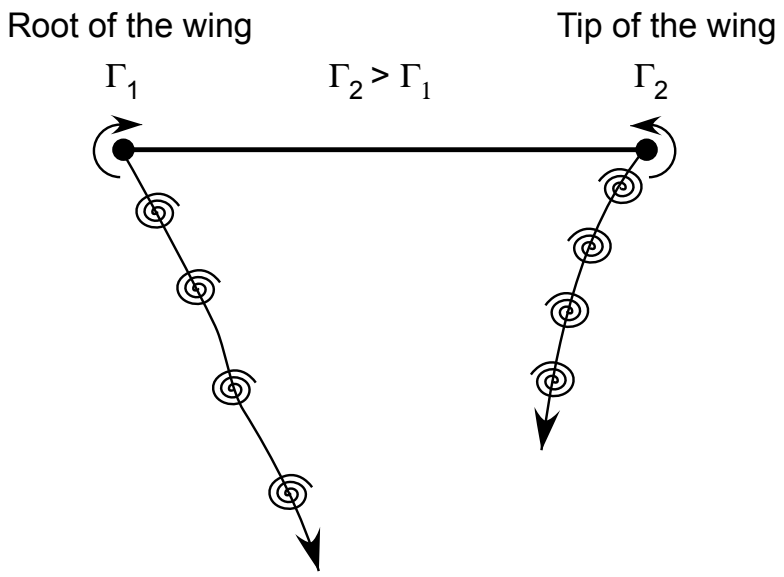

Figure 3.11: Schematic of root and tip vortex pair convecting through the wake with different circulation values.

circulation of the tip vortex was measured to be 0.1984 m^2s^{-1}. These values showed that the tip vortex was much (37%) stronger than the root vortex at this point in the wing stroke. The relative strength of the root and tip vortex is the main reason that the root vortex convects downward through the wake with a higher induced velocity. A schematic of this process is shown in Fig. 3.11.

As was performed with TR-PIV chordwise measurements, 100 images were ensemble averaged over one flapping cycle to examine the averaged near-wake, as shown in Fig. 3.12. The convection paths of the root and tip vortices in Fig. 3.10 suggested a contracting wake structure, and this outcome is confirmed by shape of the velocity contours in Fig. 3.12. As shown previously in the chordwise plane, the increase in vertical velocity in the wake and the resulting contraction of the slipstream is expected because it indicates that there is a force being applied to the wing.

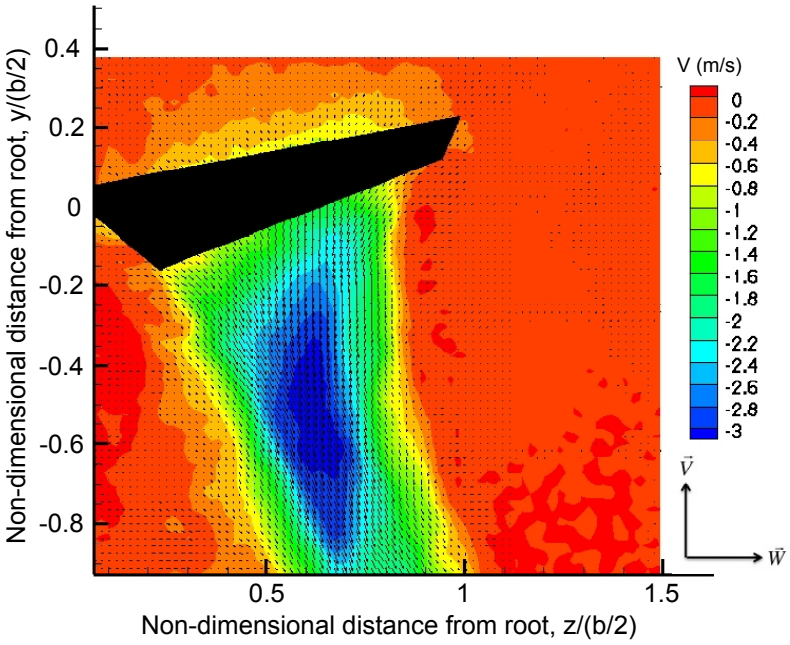

Figure 3.12: Time-averaged wake in the spanwise plane over one flapping cycle.

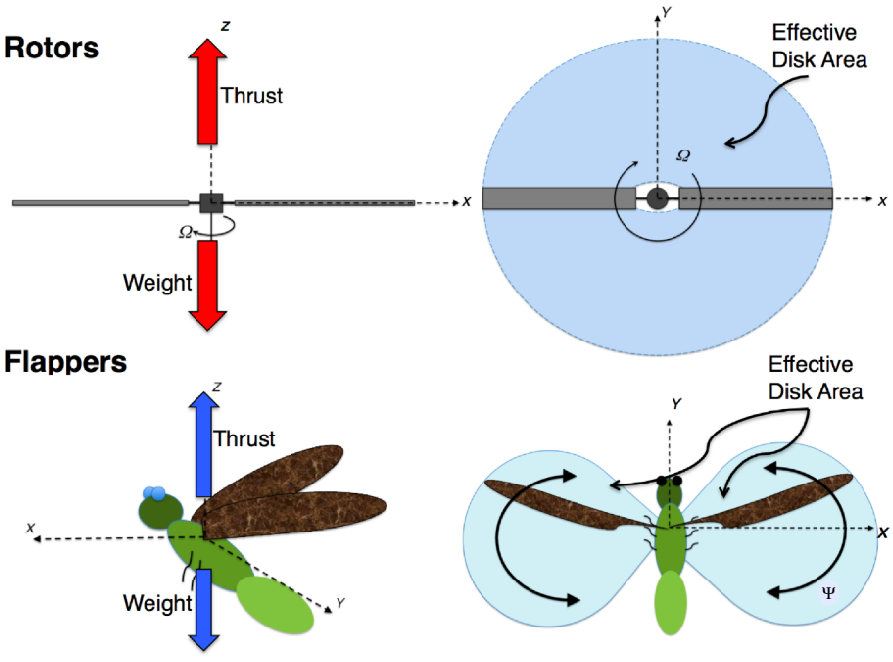

Figure 3.13: Effective disk areas for conventional rotors and flapping-wing flyers [2].

It has been suggested [26] that the control volume for a flapping wing is based upon the effective disk area defined by the net swept area in the stroke plane over one flapping cycle. For a rotor system, a cylindrical control volume is formed by the circular disk area created by the rotor blades. Figure 3.13 shows the disk area of a conventional rotor and the assumed effective disk area of a flapping wing [2].

Figures 3.8 and 3.12 have shown a contracting wake structure in two planes in the near-wake of the flapping wing. Specifically, Fig. 3.12 shows that the flapping wing does not produce increased wake velocities near the root of the wing over a flapping cycle. This outcome occurs because the effective disk area is very small at the root of the flapping wing. A rotor disk would feature increased wake velocities at the root of the blade because the rotating blade creates a uniform disk, as shown in Fig. 3.13. These results appear to confirm the previous assumption of a partial effective disk area for a flapping wing, over which the governing equations of the flow can be applied to determine theoretical results for the flow velocities and performance.

3.3.4 Summary

TR-PIV measurements were acquired in the chordwise and spanwise planes to quantitatively examine the flapping-wing flow field. The downwash velocities of the flow and the peak swirl velocities of the starting vortex were quantified at 25% and 50% span. With the spanwise TR-PIV measurements, the root and tip vortices were quantified by their peak swirl velocities and their circulation values. It was found that the tip vortex was stronger than the root vortex. The vortex pair was also tracked in the near-wake, and

the root vortex was found to convect more quickly through the wake compared to the tip vortex. Results of the time-averaged wake of the flapping wing also showed that the effective disk area can be adequately defined by the net swept area in the stroke plane over one flapping cycle.

3.4 Noncirculatory Force and Moment Results

3.4.1 Introduction

Noncirculatory forces and moments were estimated from the results of the motion tracking experiment. The motion capture system was able to characterize the complex kinematics of the flexible wing throughout the entire stroke, from which rates and accelerations could be determined. Processing of the time-history of the motion enabled the calculation of noncirculatory forces and moments on the wing using the principles of apparent mass as applied in incompressible, unsteady, thin airfoil theory. The results were used to isolate one part of the wing kinematics and aeroelastic wing deformations on the unsteady aerodynamics.

3.4.2 Definition of Forces on a Flapping Wing

The proper calculation of the aerodynamic forces acting on a flapping wing has been an outstanding issue in flapping-wing research. In this regard, measuring accurately the effective angle of attack has been a major challenge. Previous studies have made various assumptions about the flow field in an attempt to estimate the angle of attack. Birch and Dickinson [5] calculated an angle of attack using the velocity vectors that were acquired

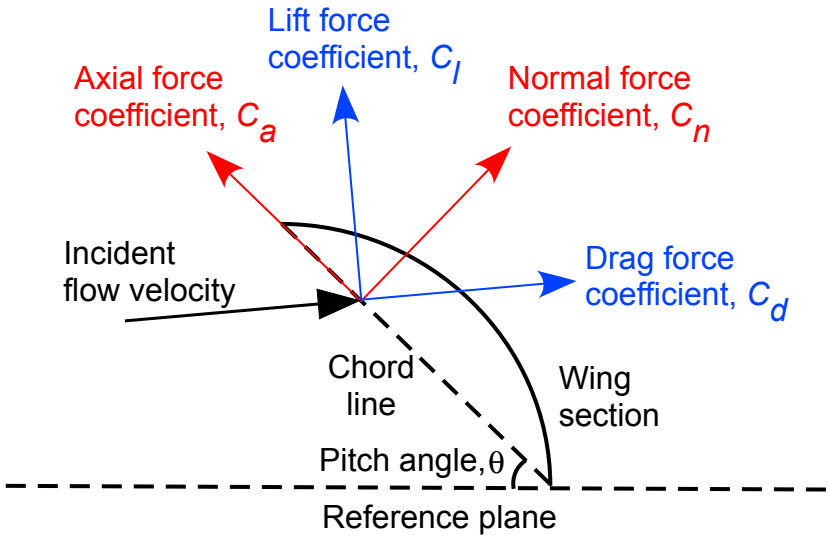

Figure 3.14: Definition of the system of forces as used in the current work.

using PIV, where they assumed that the mean orientation of the flow vectors near the lower surface of the wing represented the free-stream velocity. Usherwood and Ellington [21] assumed a "triangular" downwash distribution to estimate the angle of attack, where the downwash was assumed to vary linearly with the span.

A schematic of the force decomposition used in the present work is shown in Fig. 3.14. The velocity of the wing motion calculated from the motion tracking experiment comprised the incident (i.e., kinematic) flow velocity. Because this resultant flow velocity does not include the induced component of the velocity field, the measured lift and drag coefficients were decomposed into normal and axial force coefficients. This force definition is based on the chord line measured by the motion capture system where the normal force coefficient is defined orthogonal to the chord line and the axial force coefficient is defined along the chord line. The application of thin airfoil theory could be used in future work to calculate an alternative definition of the angle of attack for a

flapping wing, this method being outlined in Appendix B.

3.4.3 Time-History of Wing Motion

The complex wing motion of the flexible flapping wing were measured using the motion tracking system. Characterizing the wing motion was complicated significantly by the aeroelasticity of the wing. However, the deformations of the wing under the action of aerodynamic and inertial loading needed to be very accurately measured to extract meaningful results from the analysis.

Wing displacements were measured at two flapping frequencies of 17 Hz and 25 Hz, as shown in Fig. 3.15. A flapping frequency of 17 Hz was chosen to be consistent with the TR-PIV measurements, and a flapping frequency of 25 Hz was chosen because the actual MAV from which the wing was derived achieves hovering flight at this frequency. Measurements were made at six span locations along the wing. In addition to capturing wing displacement data, the motion capture system could measure the angular positions of the markers, which provided the pitch and stroke angle displacements throughout the wing motion. These displacements were processed using a 4th-order accurate 5-point central differencing method to calculate the resulting velocities and accelerations.

The data acquired at the 50% span location is representative of the flapping-wing motion throughout the stroke. Figure 3.15 a) shows the pitching characteristics of the wing at a flapping frequency of 17 Hz; notice that the pitch angle on the upstroke and downstroke of the wing is nominally symmetric. The results also show that the pitch angle changes throughout the translational stroke. These wing kinematics are unlike those

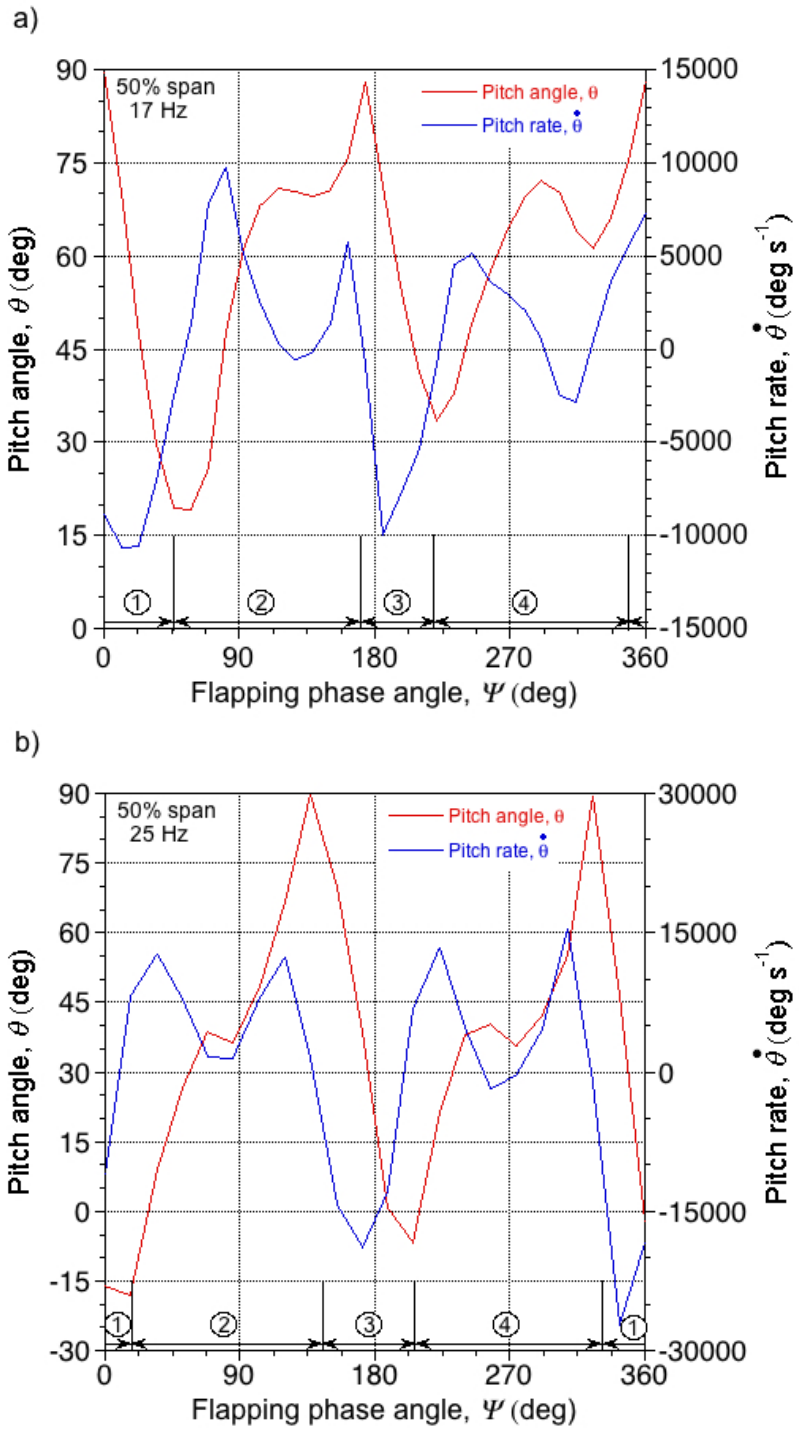

Figure 3.15: Pitch and pitch rate at 50% span: a) flapping frequency of 17 Hz; b) flapping frequency of 25 Hz. Note: 1) Pronation, 2) Downstroke, 3) Upstroke, 4) Supination.

of previous rigid flapping wing experiments [6, 13] where the pitch angle was held nominally constant throughout the translational stroke. In the present case, the wing continues to pitch up through most of its translational stroke before briefly pitching down as the wing enters into pronation or supination. Notice the large pitch rates associated with the flapping-wing motion; the wing must rotate as much as 10,000° per second during pronation and supination when operated at a flapping frequency of 17 Hz. These high rates produce significant moments, which will be explored in Section 3.4.6.

When the flapping frequency was increased to 25 Hz, there was better symmetry in the pitch angles during the upstroke and downstroke, as shown in Fig. 3.15 b). The wing experienced even greater pitch rates during the wing stroke at this higher flapping frequency, in this case reaching as high as 25,000° per second during pronation.

The differences in the wing kinematics between the two flapping frequencies are shown in Fig. 3.16. Specifically, at 25 Hz the wing shows a somewhat more complicated motion than was measured at 17 Hz. Figure 3.16 shows that the positive peaks in the pitch angle at 25 Hz occur 37° and 34° in phase earlier than the positive peaks in the pitch angle at 17 Hz. This means that the processes of pronation and supination occur earlier in the stroke such that the wing begins to pronate or supinate before the maximum stroke angle has been reached. Previous research [13] has shown that such kinematics favorably impact lift production by better utilizing wake capture effects to enhance lift generation.

The induced twisting of the flexible wing across the span was also examined. Figure 3.17 shows the twisting of the flexible wing at flapping frequencies of 17 Hz and 25 Hz when the wings have reached the midpoints of their translational strokes. At 17 Hz, negative twist was observed at both locations in the wing stroke. It is well known that negative

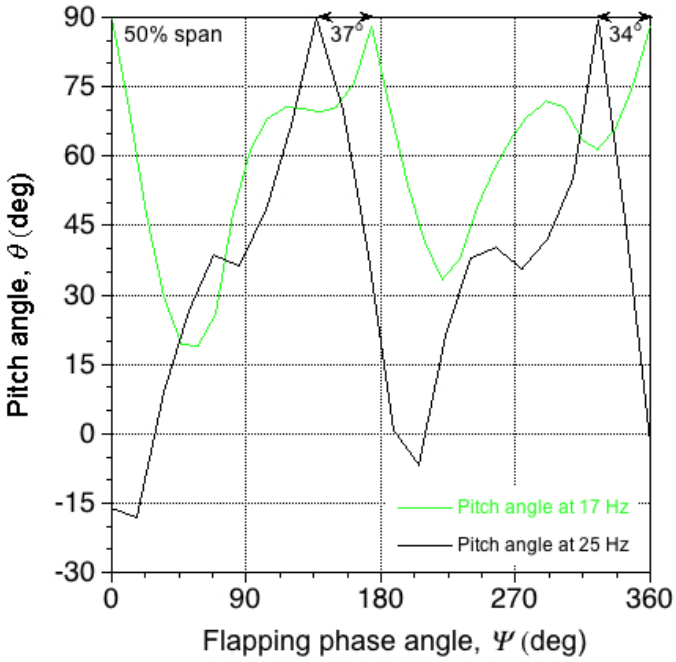

Figure 3.16: Pitch and pitch rates at 50% span comparing flapping frequencies of 17 Hz and 25 Hz.

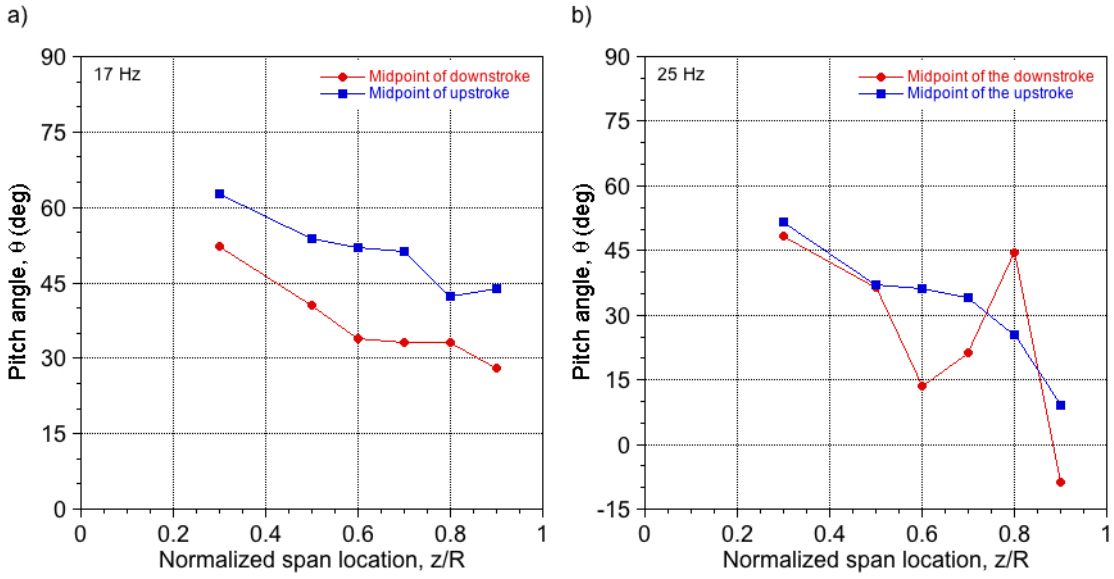

Figure 3.17: Induced twist of the flexible wing at the midpoint of the translational stroke at: a) flapping frequency of 17 Hz; b) flapping frequency of 25 Hz.

wing twist can serve to enhance the hovering ability of a lifting surface (i.e., a rotor blade) by redistributing the lift in a more desirable form, thereby helping to reduce the induced power requirements [1]. In Fig. 3.17 b), it is shown that the wing has similar values of negative twist at the midpoint of the upstroke, but much more complex aeroelastic deformations occur at the midpoint of the downstroke.

3.4.4 Noncirculatory Lift and Pitching Moments

Noncirculatory aerodynamics are produced by flow accelerations, which account for the pressure forces required to accelerate the fluid near the wing. These effects are manifest by a reciprocal effect on the wing, and are often called apparent mass effects. Because they are not associated with the generation of circulation in the flow, they are also known as noncirculatory effects. The noncirculatory or apparent mass terms arise from the $\partial\phi/\partial t$ term contained in the unsteady Bernoulli equation (i.e., Kelvin's equation) [see Karamcheti [47]]. For example, for a thin-airfoil of chord $c = 2b$ moving normal to its surface at velocity $w(t) = \ddot{h}$, the noncirculatory fluid force, F^{nc}, acting on the surface is

$$F^{nc} = -M_a \frac{dw}{dt} = -M_a \ddot{h} \tag{3.1}$$

The term M_a is known as the *apparent mass* and in this case is given by

$$M_a = \pi\rho b^2 = \pi\rho \frac{c^2}{4} \tag{3.2}$$

Substituting this into Eq. (3.1), this gives

$$F^{nc} = \pi\rho \frac{c^2}{4} \ddot{h} \tag{3.3}$$

which in coefficient form is

$$C_F^{nc} = \frac{\pi b \ddot{h}}{V^2} \tag{3.4}$$

This can be identified with the $\ddot{h}$ term in Eq. (3.5). Other apparent mass forces and pitching moments will be produced for different types of forcing; see Bisplinghoff et al. [48] for a further discussion.

To calculate the noncirculatory contributions to the total lift, the results from unsteady thin airfoil theory [24] were used. The noncirculatory lift coefficient can be written in terms of the instantaneous motion of the wing section as

$$C_{l,nc} = \pi b \left(\frac{\dot{\theta}}{V} + \frac{\ddot{h}}{V^2} - \frac{ba\ddot{\theta}}{V^2} \right) \tag{3.5}$$

where $\dot{\theta}$ is the pitch rate, $\ddot{h}$ is the plunging acceleration, $\ddot{\theta}$ is the pitch acceleration, V is the local free-stream velocity, b is the local semi-chord length, and a is the pitch axis location relative to the mid-chord measured in semi-chords. The assumption of an incompressible flow allows for the isolation of noncirculatory lift generation from those resulting from circulation, which also means that the effects do not depend on the prior history of the motion, i.e., the apparent mass effects depend only on the instantaneous motion.

The pitching moment about the mid-chord from the noncirculatory effects can also be calculated using the results of the motion tracking experiment and invoking the concepts from unsteady thin airfoil theory [24]. In this case, the moment coefficient about the mid-chord is

$$C_{m,1/2} = \frac{\pi}{2} \left[\frac{ba\ddot{h}}{V^2} - \frac{b^2}{V^2} \left(\frac{1}{8} + a^2 \right) \ddot{\theta} \right] \tag{3.6}$$

The kinematics needed for these two foregoing equations were acquired at each of the six

span locations using the wing geometry and the results obtained from the motion tracking experiment.

3.4.5 Sectional Noncirculatory Forces

Sectional noncirculatory forces were calculated at the six span locations. The individual contributors of the noncirculatory forces were also computed. As shown in Eq. (3.5), the contributions to the sectional noncirculatory lift depend on three variables during the stroke: pitch rate, plunge acceleration and pitch acceleration. Figure 3.18 shows noncirculatory force data broken down into these components at 50% span at flapping frequencies of 17 Hz and 25 Hz. Notice that the noncirculatory lift coefficient is largest when the wing is entering or undergoing pronation and supination at both frequencies. This outcome arises because the pitch rate is the dominant contributor to the noncirculatory lift. During the rotational part of the flapping cycle, the wing experiences significant pitch rates because the wing must rapidly rotate through at least 90° of pitch angle.

Figure 3.18 also shows that the plunge or heave acceleration does not contribute significantly to the noncirculatory lift coefficient. In fact, the wing experienced relatively small plunge accelerations throughout the stroke; the contributions from the pitch acceleration minimally affected lift production during the translational stroke. During pronation and supination, the pitch acceleration only slightly affected lift production. Notice the symmetry in lift generation throughout the wing stroke in both Fig. 3.18 a) and Fig. 3.18 b). Because the pitch rate is the dominant source of noncirculatory lift pro-

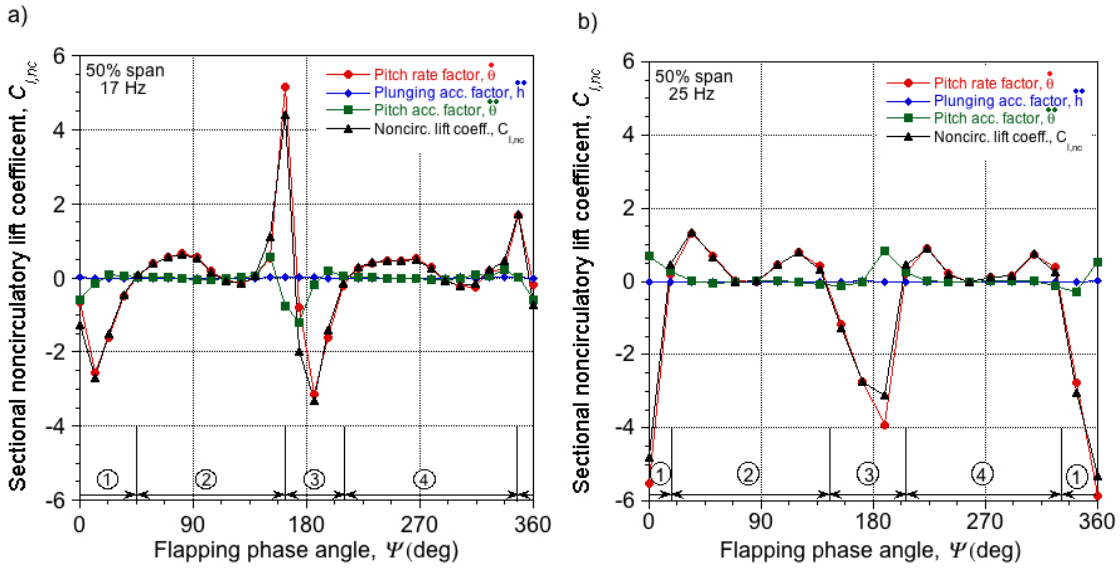

Figure 3.18: Sectional noncirculatory lift and its components at 50% span at: a) flapping frequency of 17 Hz; b) flapping frequency of 25 Hz.

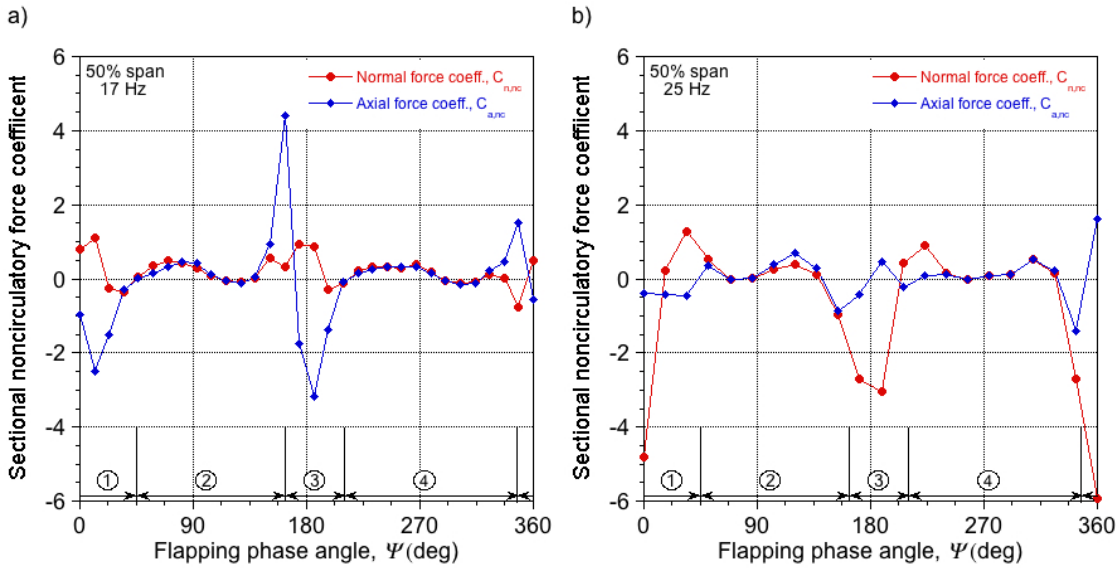

Figure 3.19: Sectional noncirculatory normal and axial force coefficients at 50% span at: a) flapping frequency of 17 Hz; b) flapping frequency of 25 Hz.

duction, the symmetry in the wing motion also manifests as a symmetric generation of noncirculatory lift components.

Figure 3.19 shows the sectional noncirculatory normal and axial force coefficients. At both flapping frequencies, the normal and axial force coefficients have similar magnitudes during the translational stroke. The axial force coefficient shows larger excursions during pronation and supination compared to the normal force coefficient at a frequency of 17 Hz. The results are different at a flapping frequency of 25 Hz where the normal force coefficient features more significant excursions during the rotation of the wing. Comparing the results in Figs. 3.18 and 3.19, the axial force somewhat resembles the lift production at 17 Hz in Fig. 3.18 a), whereas the normal force is similar to the lift generation at 25 Hz, as shown in Fig. 3.18 b).

The sectional noncirculatory lift results at the six span locations were examined at 17 Hz and 25 Hz, as shown in Fig. 3.20. At both frequencies, positive and negative lift peaks are shown at every span location during pronation and supination. Figure 3.20 a) shows that the peaks in the lift values decrease as the span location increases. Specifically, the 30% span location features the largest lift coefficient excursions during the flapping cycle. This outcome likely is because of the very small dynamic pressure and relatively modest levels of lift production. The peaks in the lift value for each span location occur at different locations during the wing stroke. This phasing of the lift production occurs as a result of the differences in the wing kinematics and aeroelastic response at each span location.

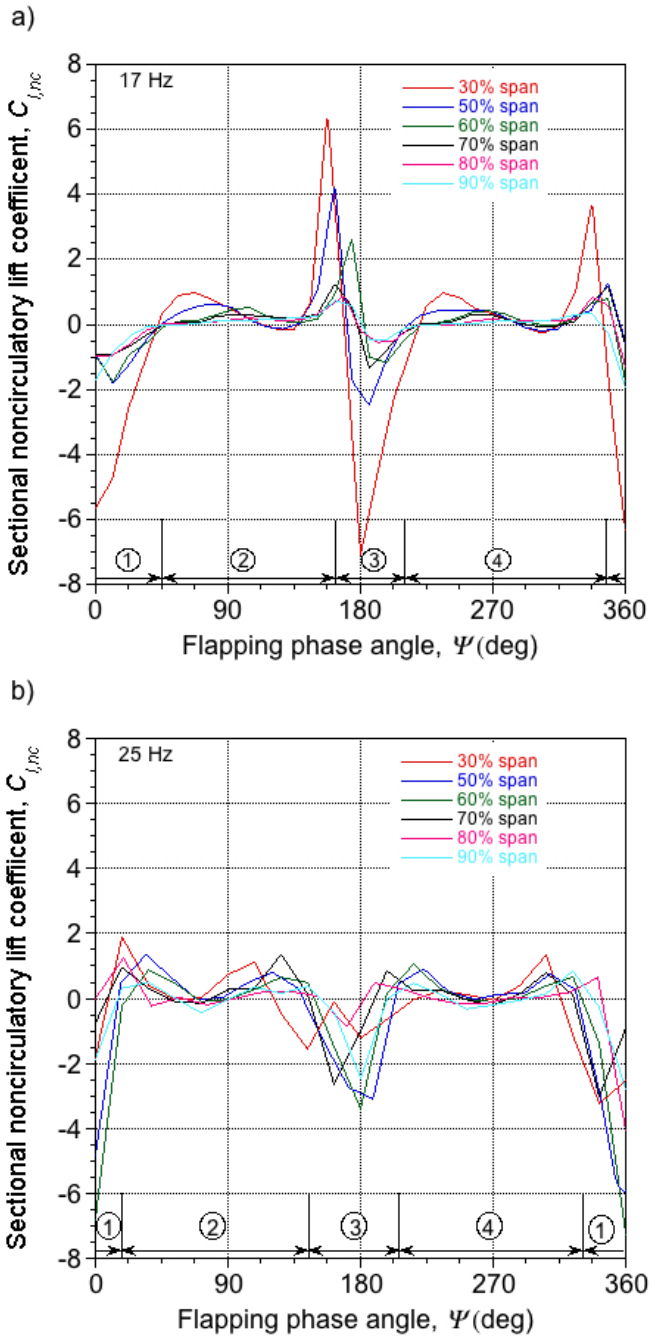

Figure 3.20: Sectional noncirculatory lift at six span locations at: a) flapping frequency of 17 Hz; b) flapping frequency of 25 Hz.

3.4.6 Sectional Noncirculatory Moments

The sectional noncirculatory component of the moment about the mid-chord was calculated from Eq. (3.6) at six span locations. For this equation, the two variables that are changing throughout the wing stroke are the plunge acceleration and the pitch acceleration. Each of their individual contributions and the values of the mid-chord moment across the span are identified.

Figure. 3.21 shows the mid-chord moment coefficient at 50% span location when the wing flaps at frequencies of 17 Hz and 25 Hz. At both frequencies, the largest values for the moment coefficient occur as the wing undergoes pronation and supination. Given the rapid rotation of the wing at these parts of the stroke, a large pitching moment is to be expected. Throughout the translational strokes, the moment values are smaller and approximately symmetric about each half-stroke. When examining the individual contributions of the pitch acceleration and the plunge acceleration, Figs. 3.21 a) and 3.21 b) show that the plunging acceleration has a negligible impact on the mid-chord pitching moment; the pitch acceleration is mostly responsible for the generation of the moment in this case.

The mid-chord pitching moment distribution across the wing span at flapping frequencies of 17 Hz and 25 Hz is shown in Fig. 3.22. Notice that the largest sectional values of the moment occur at the 30% span location, as shown in Fig. 3.22. From Eq. (3.6), it is apparent that the moment coefficient is directly proportional to the semi-chord and inversely proportional to value of the local sectional velocity. The 30% span location has the largest semi-chord (12 mm) of the six span locations but has a relatively lower incident

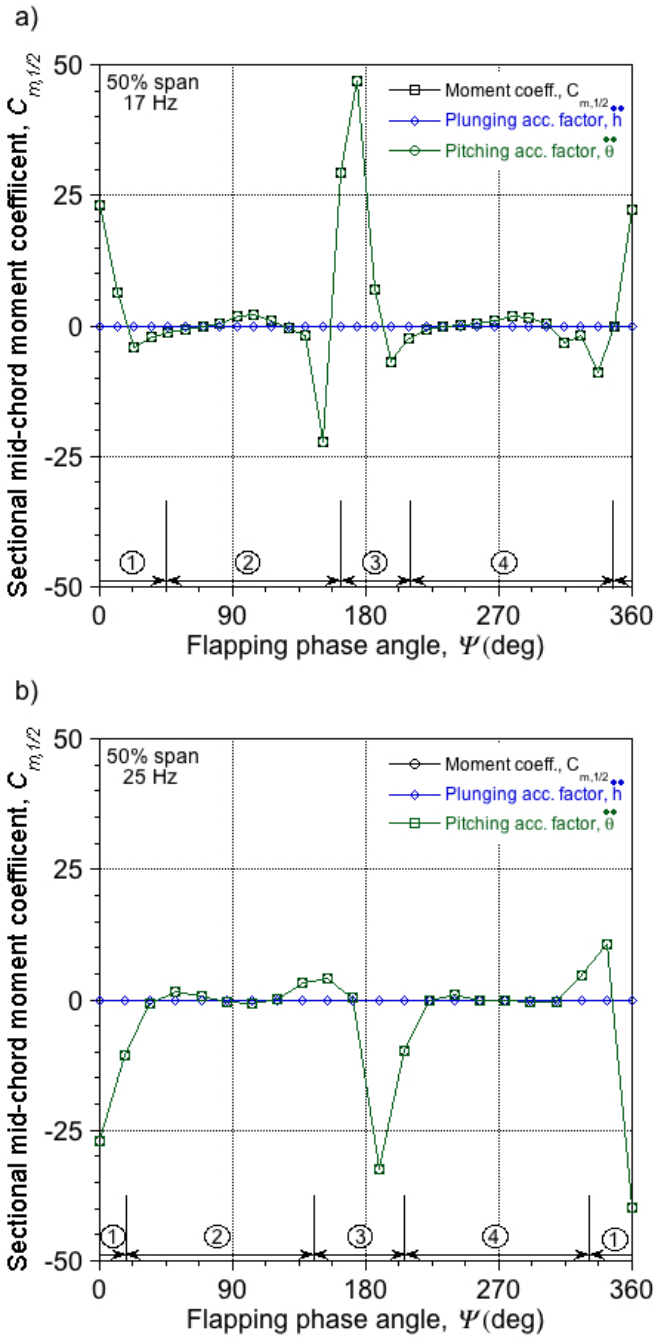

Figure 3.21: Sectional mid-chord moment coefficient at 50% span at: a) flapping frequency of 17 Hz; b) flapping frequency of 25 Hz.

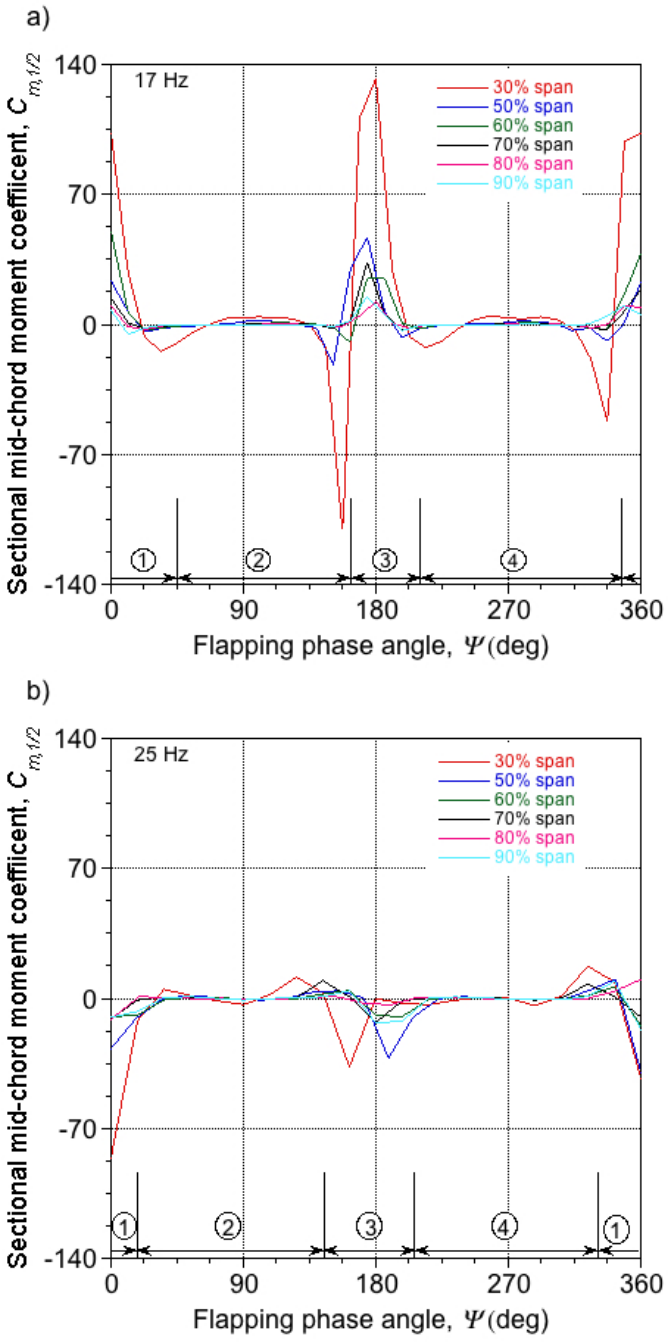

Figure 3.22: Sectional mid-chord moment at six span locations at: a) flapping frequency of 17 Hz; b) flapping frequency of 25 Hz.

velocity because of its further inboard location. Notice that the complex wing kinematics cause the maximum moment coefficient to be in-phase during the wing stroke across every span location. Comparing the mid-chord moment coefficient at the two flapping frequencies, Fig. 3.22 b) shows that the positive peaks occur earlier in the wing stroke for the 25 Hz case, which is a result of the more complicated wing kinematics obtained at this frequency.

3.4.7 Noncirculatory Forces and Moment on the Wing

The sectional noncirculatory lift results from the six span locations were integrated over the span to calculate the noncirculatory lift over the wing. The integration was performed using a trapezoidal method with boundary conditions of zero lift at the root and tip of the wing.

Figure 3.23 shows the noncirculatory lift coefficients produced on the wing at flapping frequencies of 17 and 25 Hz. Notice the symmetry in the integrated noncirculatory lift between the upstroke and downstroke at both flapping frequencies. Noncirculatory forces were noted to have a greater impact on lift generation during the rotational portion of the wing stroke compared to the translational portion of the wing stroke. The lift coefficient during the downstroke and upstroke reaches a maximum value of 0.35 at 17 Hz, and a maximum value of 0.56 at 25 Hz.

While it is clear from Fig. 3.23 that the noncirculatory forces affect the lift generation throughout the wing stroke, it is important to know whether these forces enhance (or otherwise) the net performance of the flapping wing. When the noncirculatory forces

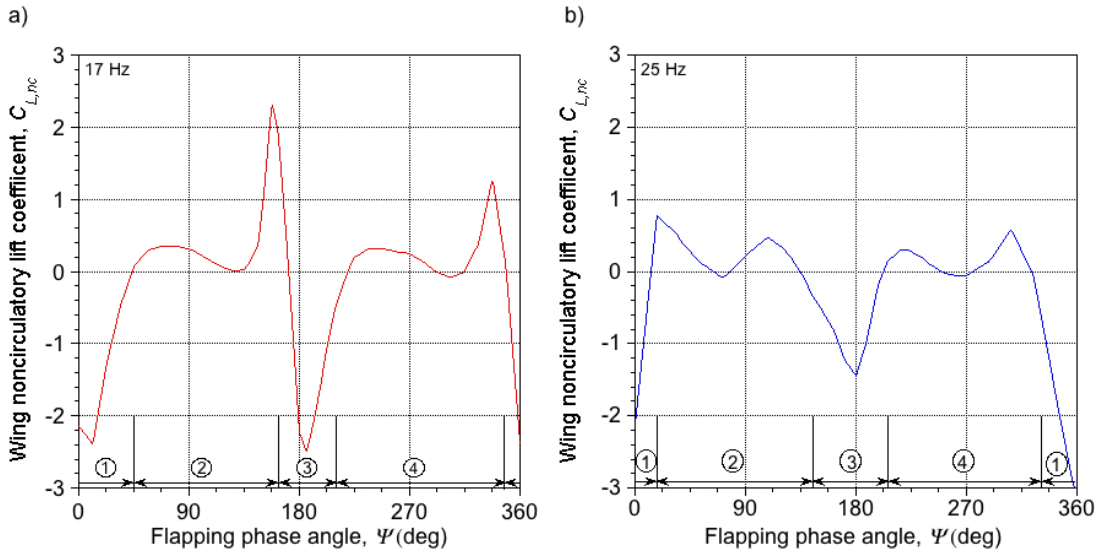

Figure 3.23: Wing noncirculatory lift production throughout the wing stroke at: a) flapping frequency of 17 Hz; b) flapping frequency of 25 Hz.

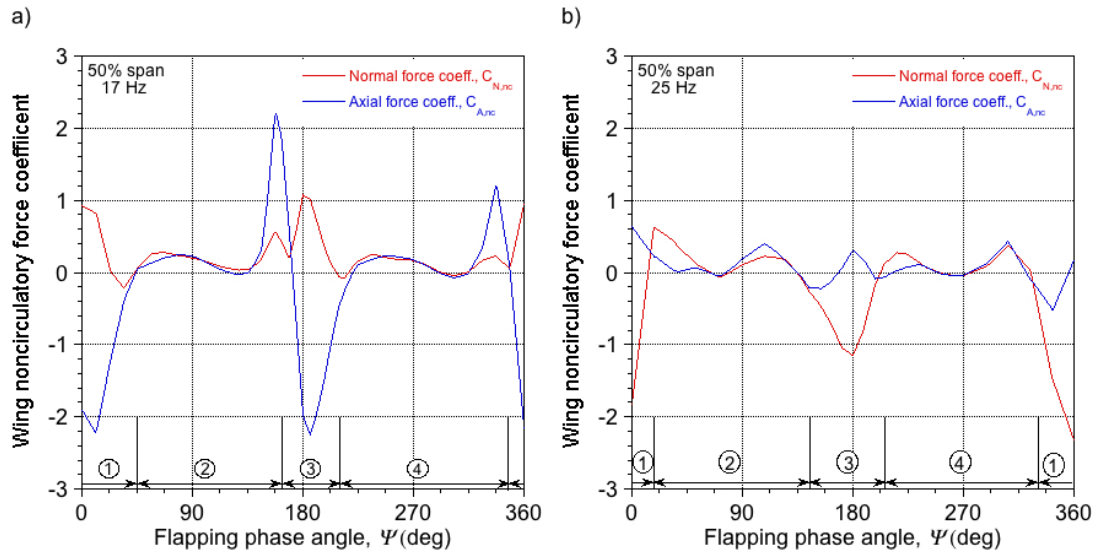

Figure 3.24: Wing noncirculatory normal and axial force production throughout the wing stroke at: a) flapping frequency of 17 Hz; b) flapping frequency of 25 Hz.

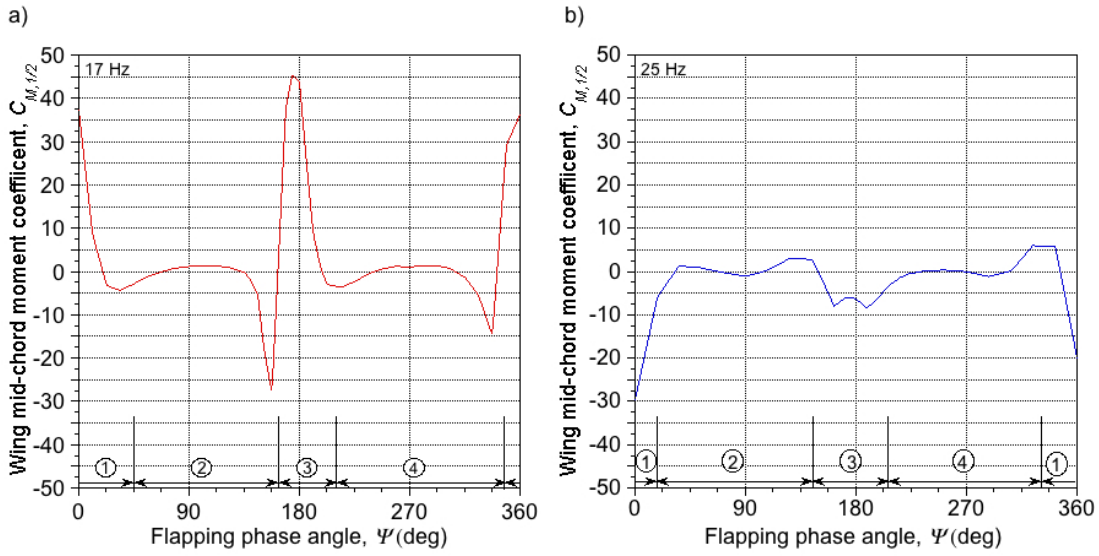

Figure 3.25: Wing noncirculatory moment about the mid-chord throughout the wing stroke at: a) flapping frequency of 17 Hz; b) flapping frequency of 25 Hz.

were integrated over one flapping cycle, it was found that these forces did not substantially affect total lift generation. In fact, the positive and negative pitch rates that predominantly influenced noncirculatory lift production were canceled by one another when they were integrated over one flapping cycle. From the standpoint of performance, this particular flapping wing at least does not create sufficient noncirculatory effects to enhance total lift production.

Figure 3.24 shows the wing normal and axial force coefficients throughout the wing stroke. Comparing Figs. 3.23 a) and 3.24 a), the axial force production more closely follows the production of lift at a flapping frequency of 17 Hz. Conversely, the normal force curve is similar to the lift curve at a frequency of 25 Hz, as shown in Figs. 3.23 b) and 3.24 b). This outcome is consistent with the observations made of the sectional force results.

The noncirculatory component of the moment on the wing at flapping frequencies of 17 Hz and 25 Hz is shown in Fig. 3.25. The largest moments occur during pronation and supination, as was previously shown with the sectional moment results. It is also clear that the peak moment coefficients at 17 Hz are larger than those at 25 Hz. Figure 3.25 shows that the flapping wing experiences large moments during its motion.

3.4.8 Summary

The complex wing kinematics of the flexible flapping wing were measured using a motion tracking system. The pitch angle during the downstroke and upstroke was found to be nominally symmetric. The measured kinematics of the wing were then used to calculate the sectional noncirculatory forces and the pitching moment about the mid-chord. The pitch rate was found to be the dominant contributor to the noncirculatory aerodynamics, which gave the largest contributions during pronation and supination. The pitch acceleration was found to be mainly responsible for the production of a pitching moment, and this term resulted in large moments being produced during pronation and supination. The sectional values for the forces and moments were integrated over the span to calculate wing force and moment coefficients. Integration over the entire flapping cycle showed that the noncirculatory forces do not contribute significantly to the total lift produced by the flapping wing.

3.5 Circulatory Lift and Drag Results

3.5.1 Introduction

The two-dimensional velocity fields obtained from PR-PIV measurements allowed for estimates of the circulatory lift and the drag of the wing section. These measurements were made at flapping frequencies of 17 Hz and 25 Hz. A circulation-box approach was applied to the measured velocity fields to estimate the circulatory lift. A momentum deficiency approach was used to enable the calculation of the sectional drag of the flapping wing. The results subsequently obtained were used to quantify the effects of the LEV on both the lifting capability of the flapping wing as well as on the efficiency of producing such lift.

3.5.2 Calculating the Circulatory Lift

The use of pressure sensors to measure aerodynamic forces on thin, flexible wings is simply not feasible. However, the two-dimensional velocity fields acquired from PIV can be used to estimate the "bound" values of circulation using the so-called circulation-box method, which can then be used to calculate the sectional lift using the Kutta-Joukowski theorem. Estimates of the bound circulation at multiple span locations can then be used to estimate the spanwise lift distribution. The procedure to estimate the bound circulation has already been used successfully to make estimates of the sectional lift produced on rotor blades [49, 50].

The schematic of this process is shown in Fig. 3.26. The first step in the procedure

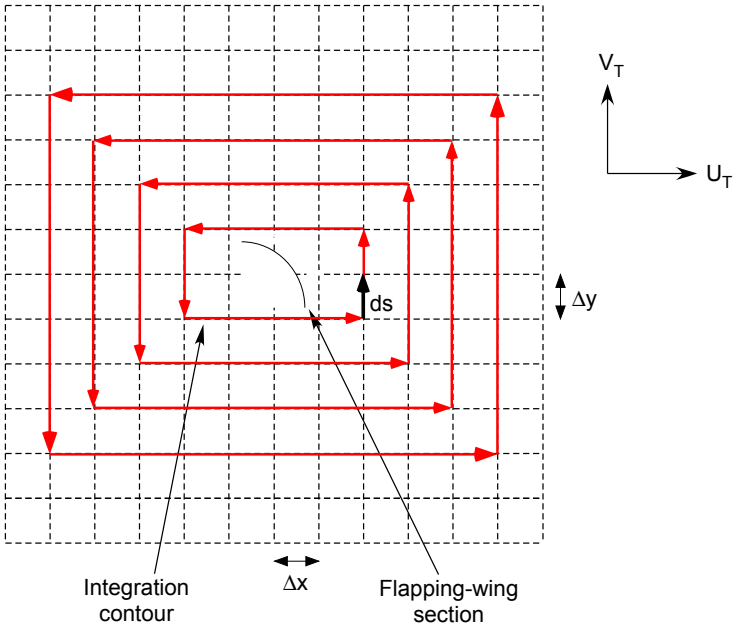

Figure 3.26: Integration process used around flapping wing to estimate sectional circulatory lift.

is to choose an initial integration contour that encloses the wing but without intersecting it. The contour can be of any shape around the wing but one of convenience is preferable; rectangular contours of different aspect ratios were used in the present work. The integration contour is then increased in unit steps (e.g., one node in the PIV grid) while numerically evaluating the closed loop line integral for the bound circulation, Γ_b, as given by

$$\Gamma_b = \oint_C V \cdot ds = \sum U_T \Delta x + V_T \Delta y \tag{3.7}$$

where U_T and V_T are the tangential velocities along the contour shown in Fig. 3.26, and Δx and Δy is the spacing of the grid containing the velocity field measurements. After a certain number of grid steps, a steady-state value of circulation is reached, as shown in

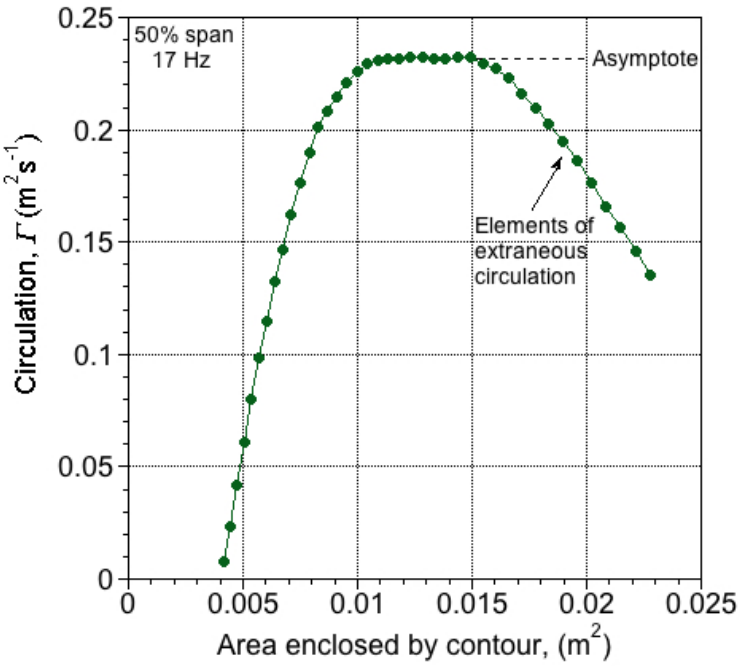

Figure 3.27: Integration process around flapping wing to estimate the sectional circulatory lift.

Fig. 3.27. Once the bound circulation on the wing is estimated, the sectional circulatory lift per unit span can be computed from the Kutta-Joukowski theorem by using

$$L = \rho V \Gamma_b \tag{3.8}$$

where ρ is the density of the air and V is the local free-stream velocity of the wing section.

A key challenge in implementing the foregoing procedure is to avoid including extraneous elements of circulation, which will artificially add to or subtract from the true value of bound circulation. In the complex flow field produced by a flapping wing, the presence of multiple vortical flow structures (e.g., turbulent shear layers, starting vortices, etc.) in the wake necessarily limited the size of the integration contour that could be used. For example, the influence of the starting vortex on the bound circulation was noted after

the contour size grew to a certain size. In Fig. 3.27, the circulation can be seen to decrease from its steady-state value if the contour becomes too large because of the inclusion of extraneous circulation, in this case from the starting vortex.

3.5.3 Calculating Drag

The momentum deficiency approach for an incompressible flow, as originally discussed by Betz [51], can be used to estimate the drag of a wing section. This approach proceeds by measuring the momentum in the flow upstream and downstream of the wing, followed by the calculation of the decrement in momentum. This change in momentum can then be equated to the force on the wing. More information about this method is provided by Giles and Cummings [52], Kusunose [53], and McAlister et al. [54].

A momentum balance upstream and downstream of the wing section gives

$$D = \int_{-\infty}^{\infty} \left(p_1 + \rho U_1^2\right) ds - \int_{-\infty}^{\infty} \left(p_2 + \rho U_2^2\right) ds \tag{3.9}$$

The total pressure is given by

$$P_T = p + \frac{1}{2}\rho \left(U^2 + V^2 + W^2\right) \tag{3.10}$$

which is introduced to the momentum balance in Eq. (3.9) to give the drag as

$$\begin{aligned} D = &\int_{-\infty}^{\infty} \left(P_{T_1} - P_{T_2}\right) ds + \frac{1}{2}\rho \int_{-\infty}^{\infty} \left(U_{T_1}^2 - U_{T_2}^2\right) ds \\ &- \frac{1}{2}\rho \int_{-\infty}^{\infty} \left(\left(V_{T_1}^2 + W_{T_1}^2\right) - \left(V_{T_2}^2 + W_{T_2}^2\right)\right) ds \end{aligned} \tag{3.11}$$

where the subscripts 1 and 2 denote the upstream and downstream locations relative the wing section, respectively. The first two integrals of Eq. (3.11) represent the profile drag,

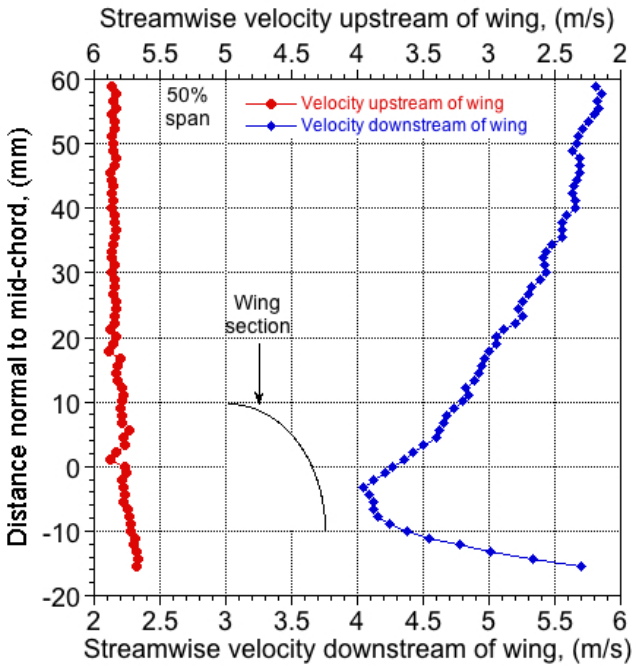

Figure 3.28: Reduction in velocity downstream of wing section at 50% span location.

and the third integral represents the induced drag [54] so that

$$D = \int_{-\infty}^{\infty} (P_{T_1} - P_{T_2})\, ds + \frac{1}{2}\rho \int_{-\infty}^{\infty} \left(U_{T_1}^2 - U_{T_2}^2\right) ds \tag{3.12}$$

The first integral in Eq. (3.12) can be neglected because there is only a small reduction of pressure inside the wake downstream of a flapping wing. Using this assumption gives the final expression for drag as

$$D = \frac{1}{2}\rho \int_{-\infty}^{\infty} \left(U_{T_1}^2 - U_{T_2}^2\right) ds \tag{3.13}$$

Figure 3.28 shows an example of the reduction in velocity downstream of the wing section, which appears as a loss of momentum in the flow and, therefore, a drag on the wing.

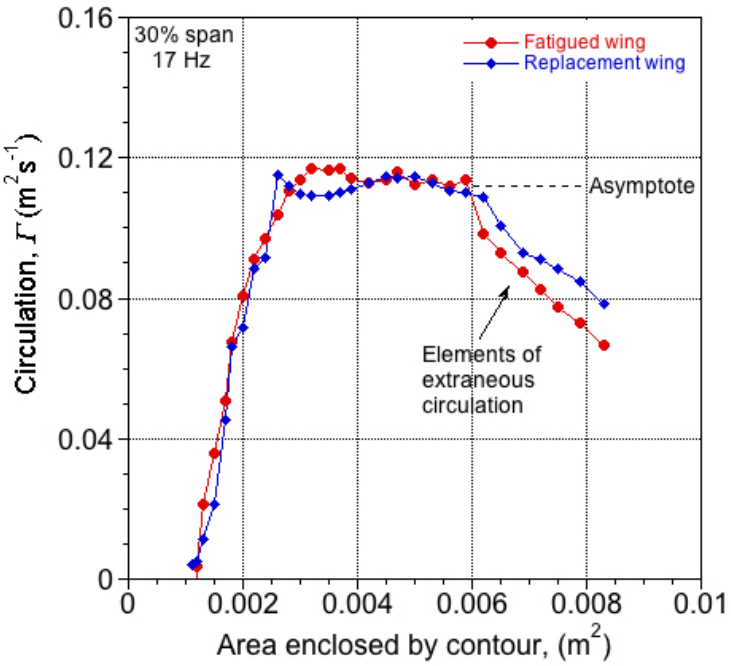

Figure 3.29: Circulation values measured on the fatigued and replacement wings.

3.5.4 Wing Construction Consistency

As previously mentioned, the fatigue life of the wing when it was flapped at a frequency of 17 Hz was approximately only one hour of testing. This problem required the periodic replacement of the wing, and consistency in construction was monitored throughout the experiments. When a wing reached the end of its fatigue life, it was removed from the wing mount and replaced with a new wing. The new wing was then tested at the same frequency and stroke location as the wing that was removed.

To ensure consistency of the aerodynamic measurements, the circulation-box method was then applied to the velocity fields measured on each wing (the fatigued wing and replacement wing). The asymptotic values of the circulation for each wing were compared to ensure that the replacement wing had no significant geometric or structural differences.

Figure 3.29 shows the circulation magnitudes at 30% span when the wing was flapped at 17 Hz. The results demonstrate that the new wing generates almost identical values for circulation compared to the wing that it is replacing.

3.5.5 Sectional Circulatory Lift and Drag Results

The sectional values for circulatory lift and drag were calculated at six span locations throughout the wing stroke using the approaches discussed in Sections 3.5.2 and 3.5.3. A representative sample of the results will be presented in this section.

Figure 3.30 shows the sectional circulatory lift and drag coefficients across the span at phase angles of $\Psi = 64^\circ$ and $\Psi = 244^\circ$ at a flapping frequency of 17 Hz. These phase angles occur before the midpoint of each translational stroke so the LEV has not yet formed. In Figs. 3.30 a) and 3.30 b), it is apparent that the sectional lift coefficient is greatest at the middle span locations (50% and 60% span). The lift coefficient then decreases toward the tip of the wing. The drag coefficient does not greatly change across the span, but reaches its peak value at the most inboard location of 30% span. Comparing Figs. 3.30 a) and 3.30 b), the lift coefficients are larger at the middle span locations at $\Psi = 244^\circ$. However, near the tip (80% and 90% span) the lift coefficients are greater at $\Psi = 64^\circ$. It is also shown that the drag coefficients are larger across the entire span at $\Psi = 244^\circ$.

In Fig. 3.31, sectional circulatory lift and drag coefficients are shown across the span before the midpoint of each translational stroke at a flapping frequency of 25 Hz. The results show that the largest lift coefficients occur at 30% span at both phase an-

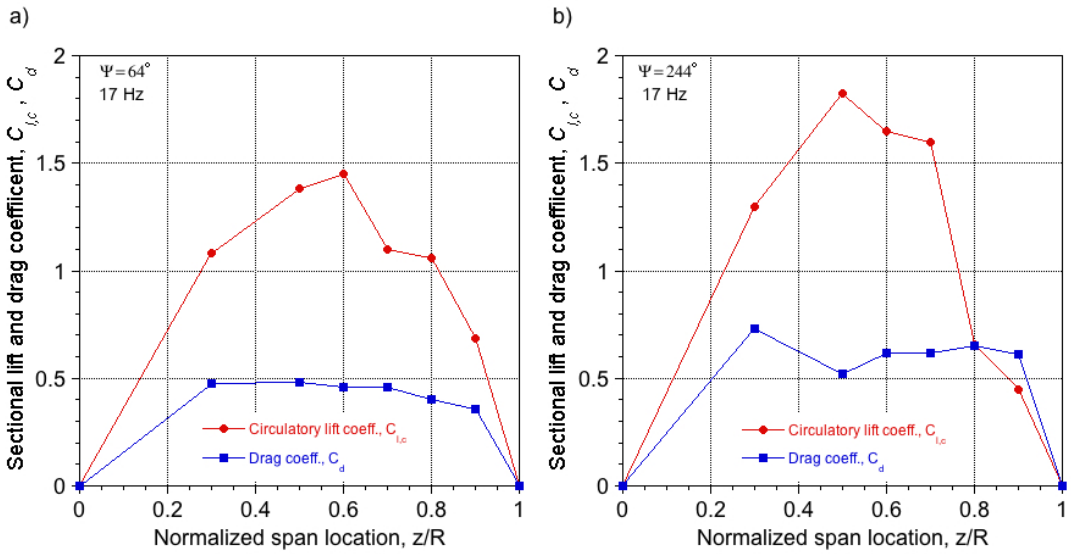

Figure 3.30: Sectional circulatory lift and drag coefficients at a flapping frequency of 17 Hz: a) at $\Psi = 64°$; b) at $\Psi = 244°$.

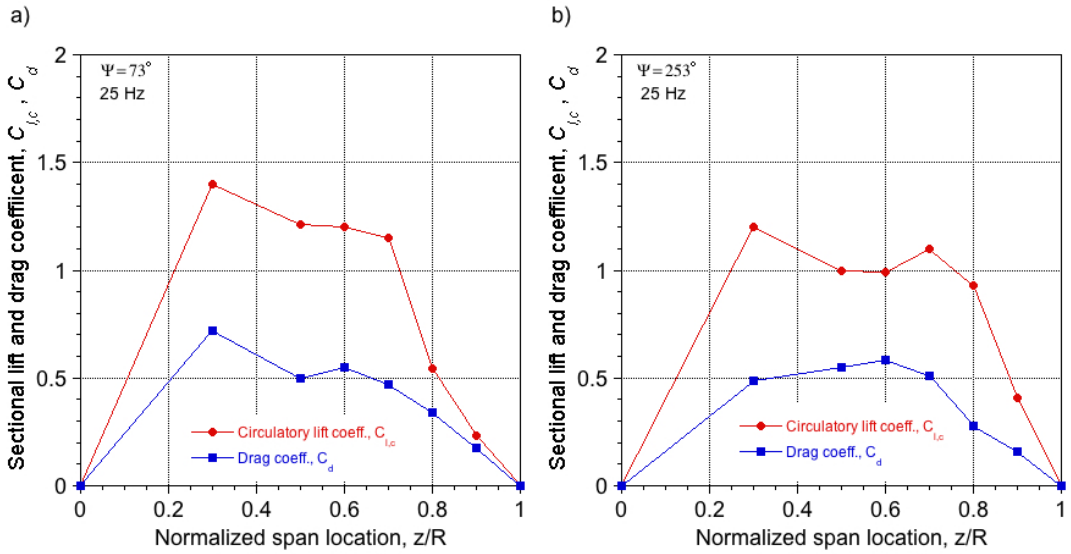

Figure 3.31: Sectional circulatory lift and drag coefficients at a flapping frequency of 25 Hz: a) at $\Psi = 73°$; b) at $\Psi = 253°$.

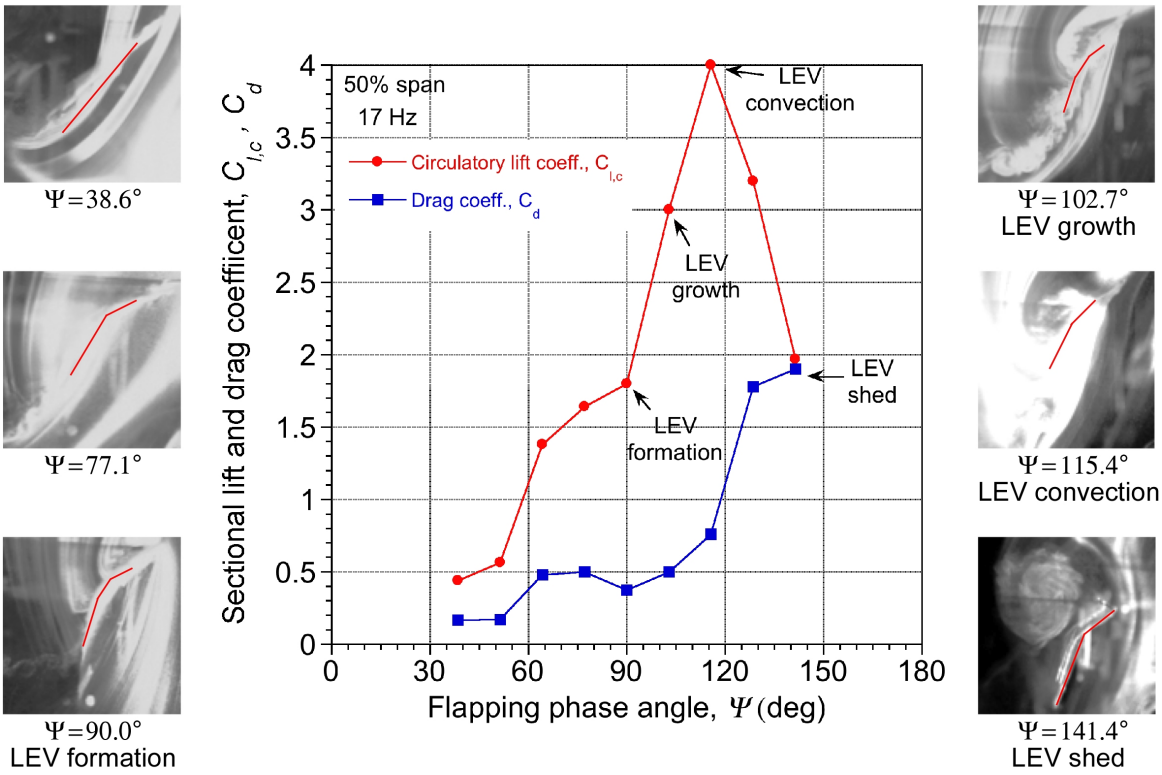

Figure 3.32: Sectional circulatory lift and drag coefficients at 50% span and a flapping frequency of 17 Hz.

gles. Also notice that on moving out toward the wing tip, the lift coefficient generally decreases. The drag coefficient similarly decreases from root to tip in Fig. 3.31 a); however, in Fig. 3.31 b) the largest drag coefficient occurs at 60% span. When comparing Fig. 3.31 a) and Fig. 3.31 b), the circulatory lift and drag coefficients were noted to have similar magnitudes across the span.

The history of the sectional circulatory lift and drag was examined throughout the wing stroke at the 50% span location. Figure 3.32 shows the lift and drag during the stroke with corresponding TR-FV images of the flow field several phase angles. When examining the circulatory lift coefficient in conjunction with the TR-FV images, it appears

that the lift coefficient begins to increase with the formation of the LEV at $\Psi = 90°$. The lift coefficient continues to increase with the growth of the LEV in size and strength at the leading edge at $\Psi = 102.7°$. The LEV detaches from the leading edge and convects over the chord at $\Psi = 115.7°$. At this point, the lift coefficient increases to its maximum value. As the wing moves through $\Psi = 128.1°$ and $\Psi = 141.1°$, the LEV is shed from the wing and the lift coefficient decreases rapidly. Clearly, the drag coefficient also rises significantly during the process of LEV shedding.

The imaging of the upper surface and trends in the forces produced on the flapping wing suggest features that are common to the classic problem of dynamic stall. Figure 3.34 shows the lift and drag coefficient data taken by McCroskey et al. [55] during the dynamic stall process on an oscillating two-dimensional airfoil. The process begins when the airfoil exceeds the static stall angle and there is a delay in the onset of flow separation. After flow separation occurs at the leading edge, a LEV begins to form. The presence of the LEV causes additional lift generation because it lowers the pressure on the upper surface of the wing. This effect results in larger lift values. The LEV eventually breaks from the leading edge and convects over the chord providing sustained lift overshoots during this process. Notice that the sectional drag increases rapidly as the LEV undergoes this process of formation and convection, as shown in Fig. 3.34. After the LEV has been shed from the trailing edge, the wing experiences lift stall as the flow on the upper surface enters a state of full separation. Flow reattachment occurs when the airfoil returns to a sufficiently low enough angle of attack. A schematic of this dynamic stall process is shown in Fig. 3.33.

The comparison of Figs. 3.34 and 3.35 shows that the flapping wing also undergoes

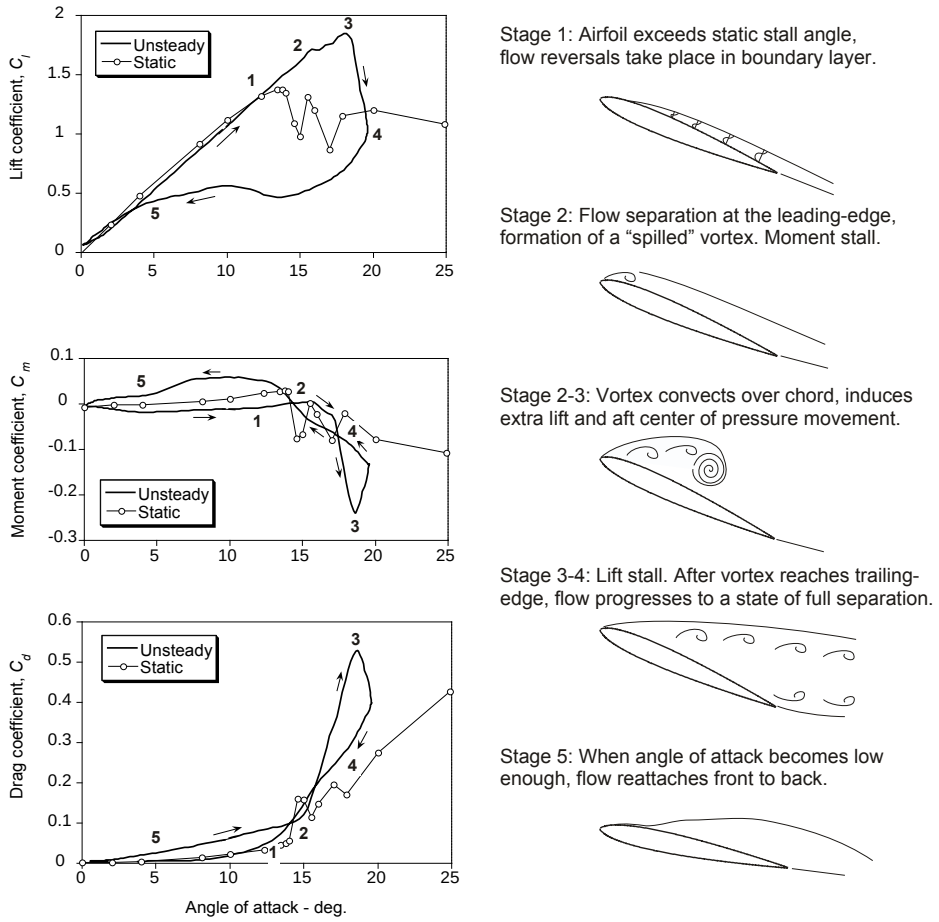

Figure 3.33: Schematic showing the flow morphology and the unsteady airloads during the dynamic stall process on an oscillating two-dimensional airfoil [1].

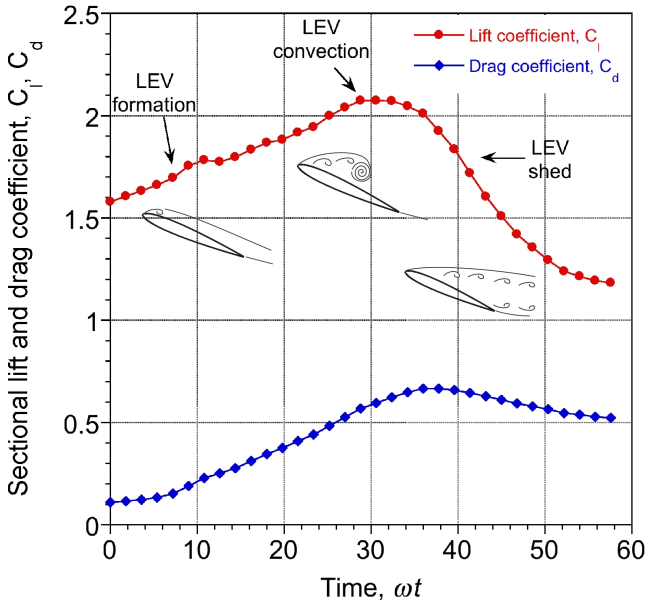

Figure 3.34: Force coefficients produced on an oscillating two-dimensional airfoil experiencing dynamic stall.

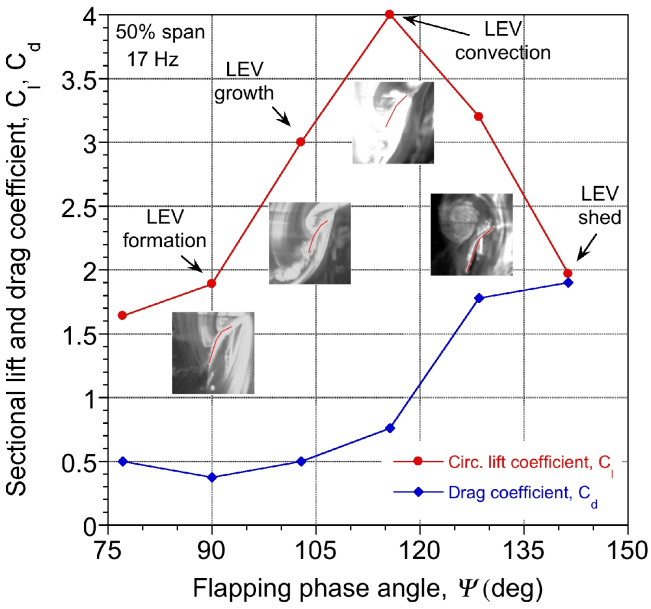

Figure 3.35: Sectional circulatory lift and drag on the flapping wing at 50% span and a flapping frequency of 17 Hz.

a very similar process to classic dynamic stall. A rapid lift increase through the formation and convection of the LEV is shown in both cases. Once the LEV is shed, both the airfoil and flapping wing show sharp increases in lift during the convection of the LEV. The drag also increases with the onset and progression of the dynamic stall process in both cases.

This process of LEV formation, convection, and shedding is similar to the process of dynamic stall on an oscillating two-dimensional airfoil. The speed at which these unsteady processes occur can be compared on the basis of a non-dimensional time parameter known as reduced time, s. This value represents the relative distance traveled by an airfoil in terms of airfoil semi-chords during a time interval [1], and is given by

$$s = \frac{1}{b}\int_{t_1}^{t_2} V\,dt \tag{3.14}$$

where b is the local semi-chord length, t_1 and t_2 refer to the time interval of the formation and shedding of the LEV, and V is the local section velocity. The reduced time of the dynamic stall process at a higher Reynolds number ($Re = 10^6$) is typically between 6–9 [1]. For the current flexible flapping wing, the process of LEV formation and shedding occurs at a reduced time of about 4.2. This result means that the process of LEV formation and shedding occurs more quickly on this flapping wing when compared to a similar process on an airfoil at higher Reynolds numbers.

3.5.6 Sectional Normal and Axial Force

The sectional circulatory lift and drag coefficients were decomposed into normal and axial force coefficients, as defined in Fig. 3.14. Figures 3.36 and 3.37 show the sectional normal and axial forces across the span at flapping frequencies of 17 Hz and 25 Hz.

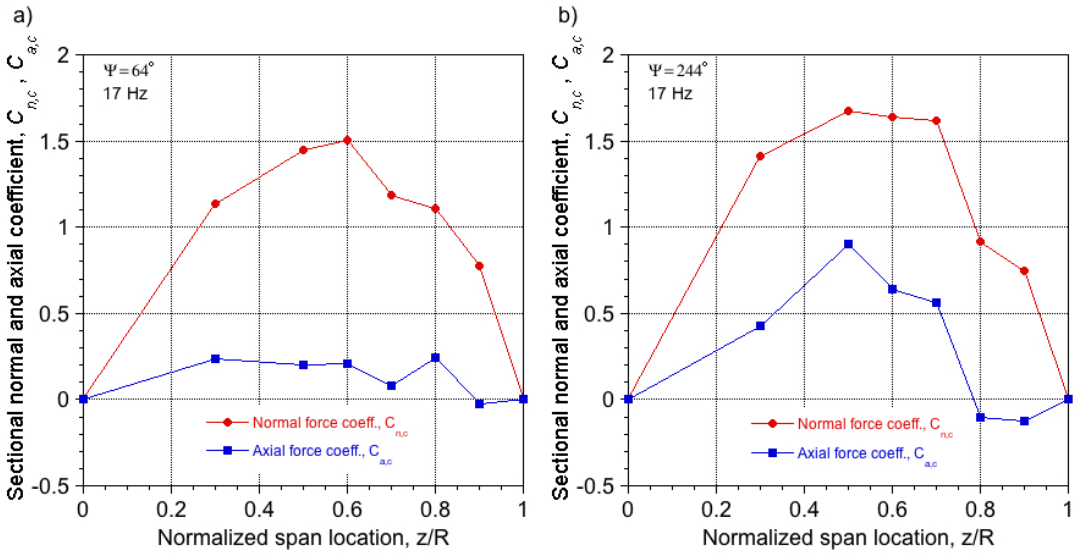

Figure 3.36: Sectional normal and axial force coefficients at a flapping frequency of 17 Hz: a) at $\Psi = 64°$; b) at $\Psi = 244°$.

These measurements can be compared to sectional lift and drag results shown Figs. 3.30 and 3.31. In Fig. 3.36, it is apparent that the normal force distribution resembles the shape of the lift coefficient distribution measured at 17 Hz. This outcome occurs because of the particular wing kinematics at this stroke location; the pitch angle and the orientation of the wing velocity have aligned a significant component of the lift force along the direction of the normal force. In Fig 3.30 b), the axial force distribution resembles the drag force distribution across the span, but in this case it is more complex and features negative values at 80% and 90% span. These negative values mean that the axial force acts along the chord line in the direction of the trailing edge.

Figure 3.37 shows the sectional circulatory normal and axial forces at a flapping frequency of 25 Hz. Compared to the lift force shown in Fig. 3.31 a), the normal force is generally smaller in magnitude and has a maximum value at 60% span. In Fig. 3.37 b),

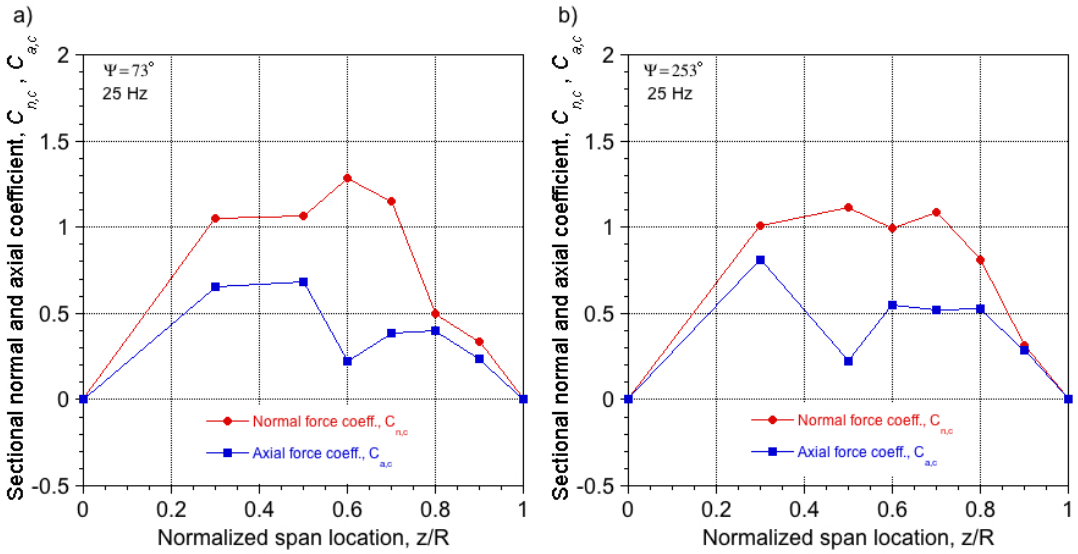

Figure 3.37: Sectional normal and axial force coefficients at a flapping frequency of 25 Hz: a) at $\Psi = 73°$; b) at $\Psi = 253°$.

the normal force distribution correlates well with the lift force distribution at this stroke location. In both cases, the axial force shows similar magnitudes to those of the drag force, but has a different distribution. This outcome occurs because of differences in the local wing kinematics at each span location.

3.5.7 Summary

Circulatory lift and drag have been calculated at six span locations and two flapping frequencies. The circulatory lift was measured during the LEV formation and shedding, which showed that the LEV was responsible for significantly increasing the lift on the wing. These measurements were qualitatively consistent with measurements of classic dynamic stall made on an oscillating two-dimensional airfoil. Sectional normal and axial force components were also computed.

3.6 Total Lift and Drag and Lift-to-Drag Ratio

3.6.1 Introduction

The noncirculatory and circulatory lift values were combined and examined in terms of total lift production throughout the wing stroke. The relative contributions to the total lift from noncirculatory and circulatory forces were compared. By acquiring drag measurements, estimates were made of the lift-to-drag ratio of the flapping wing, which can provide a measure of how efficiently the flapping wing is producing lift.

3.6.2 Sectional Total Lift and Drag and Lift-to-Drag Ratio

Sectional measurements of the noncirculatory and circulatory lift coefficients were combined to calculate total sectional lift coefficients. The contributions from each source of the sectional lift are shown in Fig. 3.38 for 50% span during the downstroke at a flapping frequency of 17 Hz. In this analysis, the proper amplitude and phasing of the noncirculatory forces was enforced. The noncirculatory and circulatory forces must be added vectorially in this unsteady problem. It is evident from Fig. 3.38 that the contributions from the circulatory lift are greater than those from the noncirculatory lift. The difference in the magnitude is most significant during the formation and convection of the LEV where the circulatory lift dramatically increases. Figure 3.38 shows that for these particular wing kinematics, the noncirculatory contributions to the total lift are not as significant as the circulatory contributions.

With the calculations of the total sectional lift and drag coefficients, an estimate

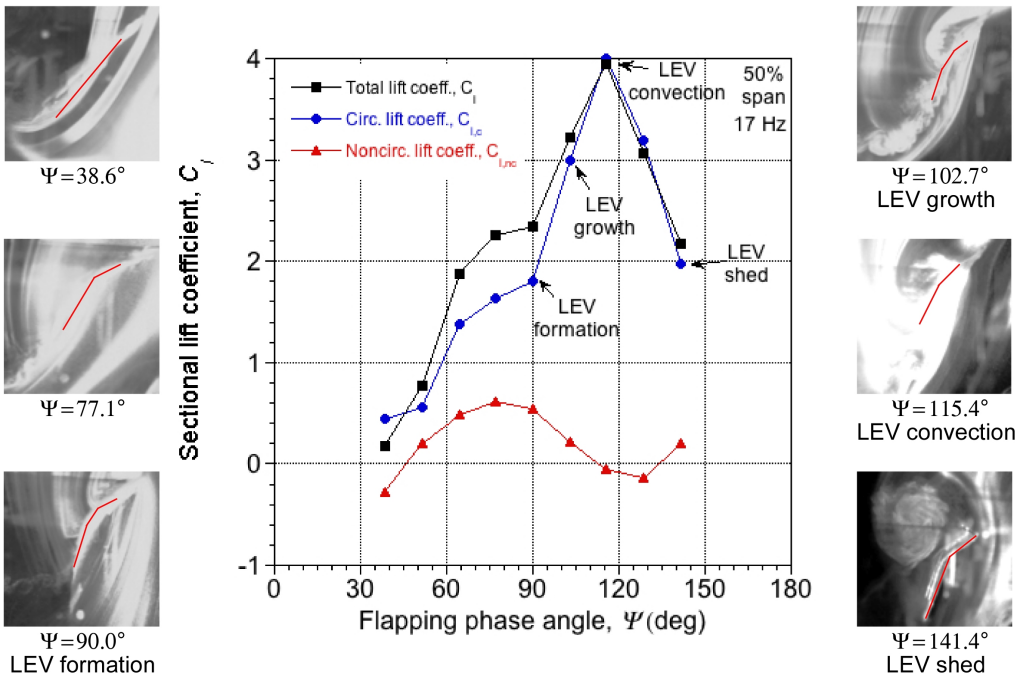

Figure 3.38: Sectional noncirculatory and circulatory lift coefficients combined into a total lift coefficient during the downstroke at 50% span and a flapping frequency of 17 Hz.

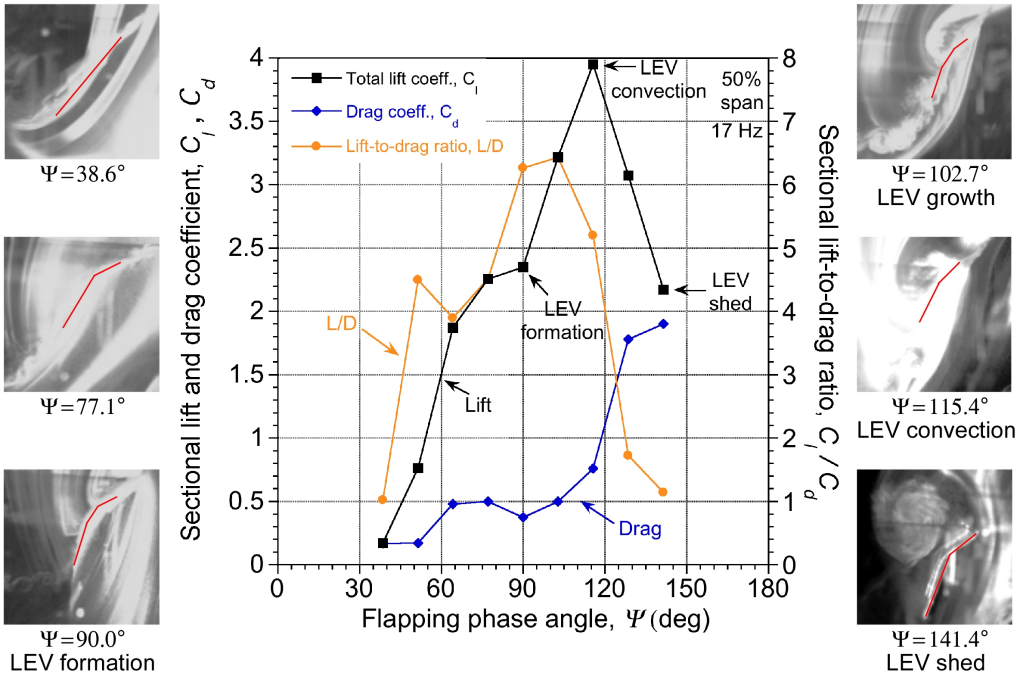

Figure 3.39: Sectional lift-to-drag ratio at 50% span at a flapping frequency of 17 Hz.

of the lift-to-drag ratio can be made. Figure 3.39 shows values of the lift-to-drag ratio throughout the downstroke at 50% span and a flapping frequency of 17 Hz. The results shows that the sectional lift-to-drag ratio is sustained at values between 4 and 4.6 before the onset of dynamic stall. Once LEV formation commences, the lift-to-drag ratio increases to 6.3. With LEV growth, the lift-to-drag ratio rises to 6.43. The lift-to-drag ratio remains at an increased value of about 5.2 during the convection of the LEV. Once the LEV begins to shed from the wing, the lift-to-drag ratio rapidly falls to 1.72 and then 1.14. Notice that because the lift generation increases at a faster rate than the drag production during the LEV formation, growth, and convection process, it is very significant that the sectional lift-to-drag ratio increases during this process. In fact, this behavior is different compared to the classical process of dynamic stall where the lift-to-drag ratio decreases catastrophically during leading-edge vortex shedding.

The foregoing values were compared to the previously shown dynamic stall data collected by McCroskey et al. [55]. Figures 3.40 and 3.41 compared the lift-to-drag ratio as it changes during the dynamic stall process on an oscillating two-dimensional airfoil at a higher Reynolds number ($Re = 10^6$) with the results from the present flapping wing. These plots show significant differences in the lift-to-drag ratio during the dynamic stall process. With the two-dimensional airfoil, the lift-to-drag ratio decreases significantly throughout the process of dynamic stall. The additional lift produced by the presence of the LEV on the upper surface does not compensate for the increases in drag. However, in the case of the flapping wing, the sectional lift-to-drag ratio actually increases throughout the process of LEV formation and shedding. This interesting result may give insight into why flapping-wing flyers deliberately produce LEVs.

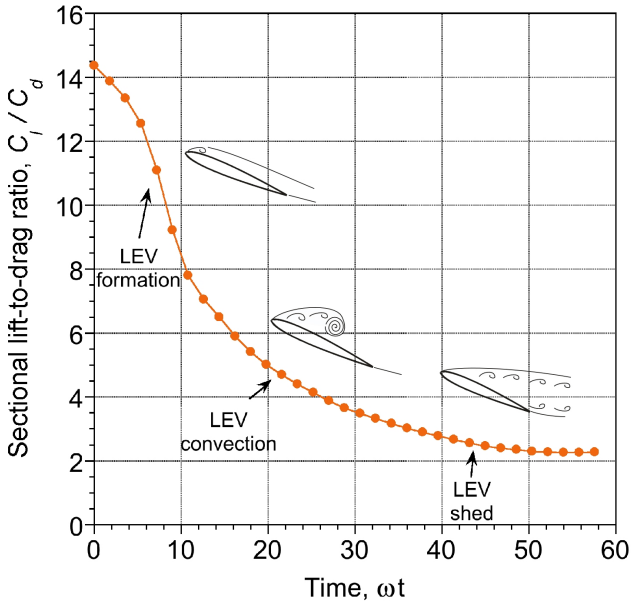

Figure 3.40: Sectional lift-to-drag ratio produced on an oscillating two-dimensional airfoil experiencing dynamic stall (Reynolds number = 10^6).

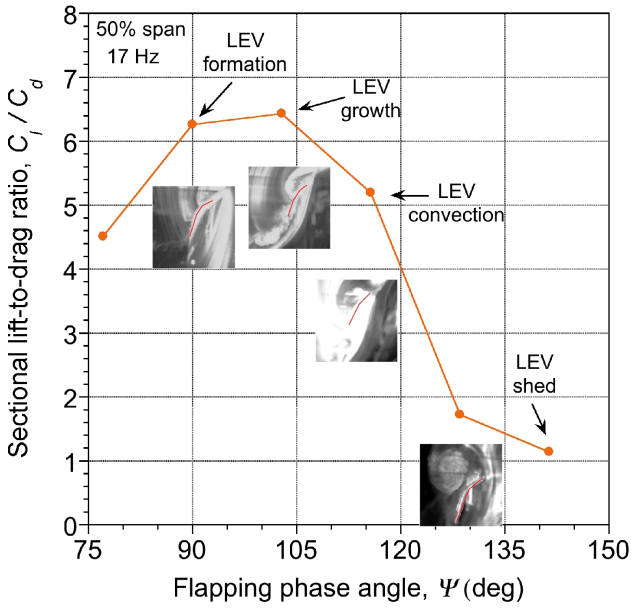

Figure 3.41: Sectional lift-to-drag ratio produced on a flapping wing during its downstroke at 50% span and a flapping frequency of 17 Hz (Reynolds number = 9000).

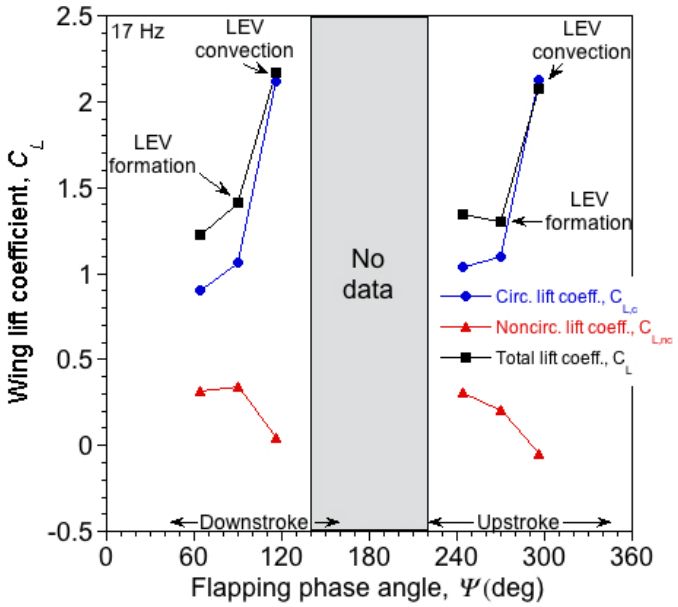

Figure 3.42: Wing total lift decomposed into noncirculatory and circulatory contributions at a flapping frequency of 17 Hz.

3.6.3 Wing Total Lift, Drag and Lift-to-Drag Ratio

Measurements of the sectional lift and drag were made at six span locations. After integrating these values over the chord, the wing forces and lift-to-drag ratios were calculated. Figure 3.42 shows the wing total lift coefficient and its two components (noncirculatory and circulatory) during the translational strokes at a flapping frequency of 17 Hz. The circulatory lift is shown to have a greater relative contribution compared to the noncirculatory lift. While LEV formation and convection have been shown to occur only over some of the wing span, the increased lift at those span locations caused the total wing lift to also increase during these parts of the stroke.

In Fig. 3.43, the total lift coefficient is shown in terms of its circulatory and noncirculatory components during the translational strokes at a flapping frequency of 25 Hz.

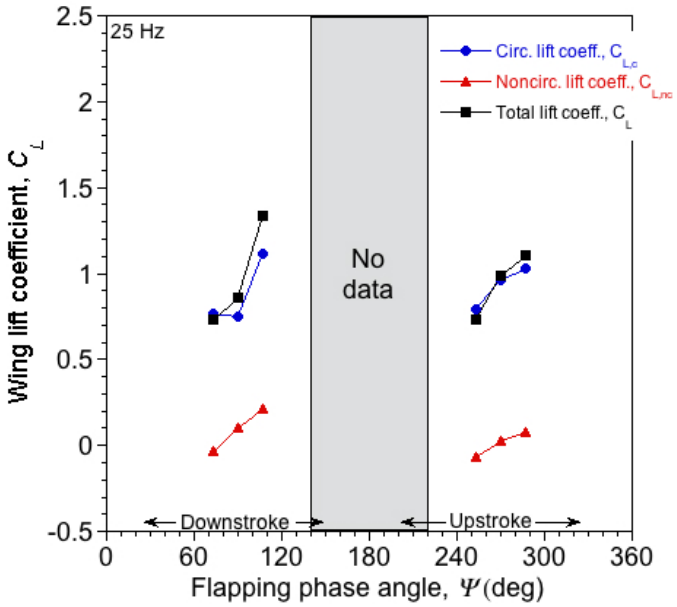

Figure 3.43: Wing total lift decomposed into noncirculatory and circulatory contributions at a flapping frequency of 25 Hz.

The circulatory lift is obviously a much larger part of the lift than the noncirculatory lift, as seen in the forces at 17 Hz. Compared to the total lift data at 17 Hz, lower wing lift coefficients were produced at a frequency of 25 Hz. During the downstroke and upstroke at 17 Hz, the total lift coefficient was greater by about 0.49 and 0.62 before LEV formation in comparison to the 25 Hz case. The total lift coefficient at 17 Hz during LEV convection was greater by 0.83 and 0.96 compared to that measured at 25 Hz.

Figure 3.44 shows the total wing lift and drag, as well as the wing lift-to-drag ratio, at a flapping frequency of 17 Hz. Notice that the lift-to-drag ratio of the wing increases when the LEV is produced. During the downstroke, the lift-to-drag ratio before LEV formation is 3.4. When the LEV convects over the chord, the lift-to-drag ratio increases to 3.65. During the upstroke, the lift-to-drag before LEV formation is 2.64. During LEV

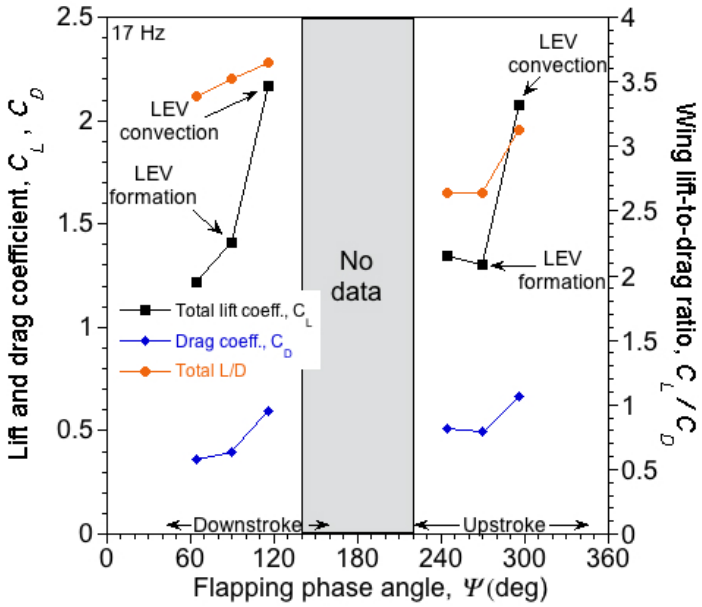

Figure 3.44: Wing lift-to-drag ratio during the translational stroke at a flapping frequency of 17 Hz.

convection, the lift-to-drag ratio actually increases to 3.12.

In Fig. 3.45, the total lift and drag are shown along with the calculated wing lift-to-drag ratio at a flapping frequency of 25 Hz. Notice that the lift-to-drag ratio increases as the wing moves through its translational strokes. Comparing the results in Figs. 3.44 and 3.45, the lift-to-drag ratios were generally higher at 17 Hz. Even before LEV formation, the lift-to-drag ratio was larger at 17 Hz compared to the 25 Hz case. Also notice that at 17 Hz, the larger lift-to-drag ratios occur during the downstroke. Conversely, the greater lift-to-drag ratios occur during the upstroke at 25 Hz. The complex wing kinematics are responsible for these asymmetries in the lift and drag production.

It should be pointed out, however, that these lift-to-drag ratios are still relatively low in comparison to typical lift-to-drag ratios found on airfoils that operate at higher chord Reynolds numbers. As shown in the data taken by McCroskey et. al [55], the sectional

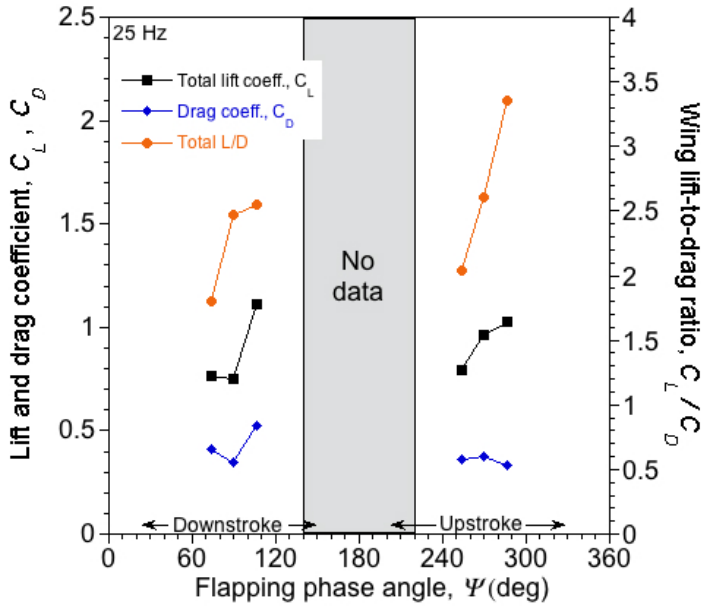

Figure 3.45: Wing lift-to-drag ratio during the translational stroke at a flapping frequency of 25 Hz.

lift-to-drag ratio before the onset of dynamic stall was approximately 14.5. Comparatively, the maximum sectional lift-to-drag ratio found during the stroke of the flapping wing at either frequency was approximately 6.43 (during LEV convection).

3.6.4 Importance of Lift-to-Drag Ratio in the Evaluation of Performance

The lift-to-drag ratio is an important consideration in the analysis of a hover-capable platform. In the discussion of hover performance, the figure of merit, FM, of a rotor is defined as the ratio of the ideal power required to hover to the actual power required to hover [1]. It can be used to gauge the ability of a hovering vehicle to generate thrust for a given power. This metric depends on a redefined sectional lift-to-drag ratio, $C_l^{3/2}/C_d$, in

the equation

$$FM = \frac{1}{\kappa + \left(\frac{2.6}{\sqrt{\sigma}}\right)\left(\frac{C_l^{3/2}}{C_d}\right)^{-1}} \tag{3.15}$$

This equation shows that FM will be maximized when all of the airfoils are operating at their best lift-to-drag ratios. The airfoils must be carefully designed for high-lift, low-drag, and the ability maintain its favorable characteristics over a range of angles of attack and chord Reynolds numbers [56].

The lift-to-drag ratio also plays an critical role in the determination of the forward flight performance of a hover-capable platform. The lift-to-drag ratio of a rotor, $(L/D)_R$, is dependent upon the sectional lift-to-drag ratios of the airfoil, as given by

$$\left(\frac{L}{D}\right)_R = \left[\frac{\kappa\sigma C_L}{12\mu^2} + \frac{3}{4\mu}\left(\frac{C_d}{C_l}\right)(1 + K_1\mu^2 + K_2\mu^4)\right]^{-1} \tag{3.16}$$

This equation shows that the performance of the rotor is directly proportional to the operating sectional lift-to-drag ratios of the airfoil. An average blade section lift-to-drag ratio of about 30 limits the maximum realizable rotor lift-to-drag ratio to a value of approximately 7 [56].

These results for a rotor suggest that more foundational research is needed toward optimizing the design of a flexible flapping wing. The present work shows maximum sectional lift-to-drag ratios of only 6–6.5 during LEV shedding. Throughout the remainder of the wing stroke, the sectional lift-to-drag ratios were between 1–4.5. While lower efficiencies are to be expected in this range of chord Reynolds number 10^2–10^5, the efficiency of wing sections will need to be improved such that good lift-to-drag ratios are sustained throughout the entire wing stroke. This will be essential for a flapping-wing MAV to meet requirements for payload capacity, range, and endurance.

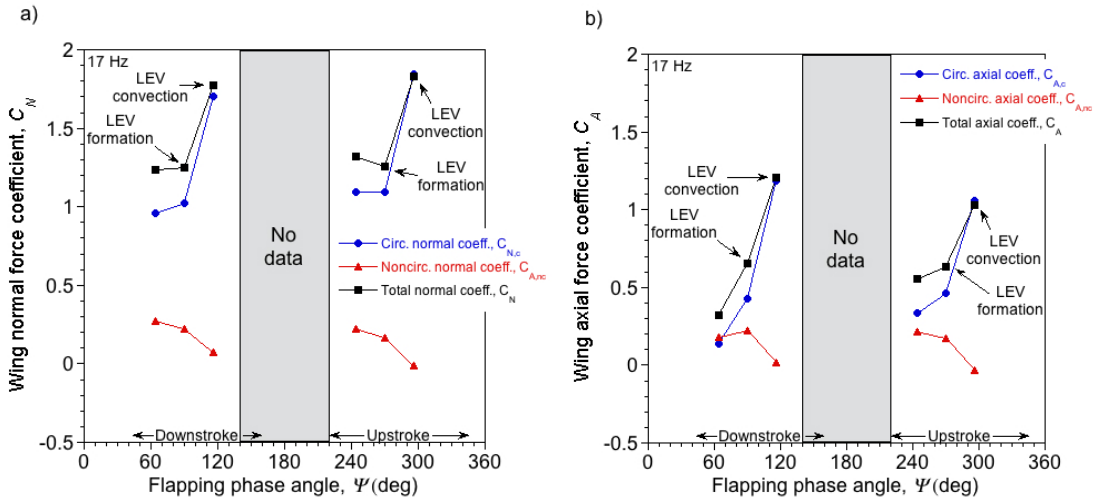

Figure 3.46: Wing total forces decomposed into contributions from noncirculatory and circulatory forces at a flapping frequency of 17 Hz: a) normal force coefficient; b) axial force coefficient.

3.6.5 Wing Total Forces

Sectional normal and axial forces generated by noncirculatory and circulatory forces were combined during the translational strokes. Figure 3.46 shows these forces at a flapping frequency of 17 Hz. In Fig. 3.46 a), the circulatory normal force is shown to have a greater relative contribution to the lift on the wing compared to the noncirculatory force. The axial force, however, receives comparable contributions from both the noncirculatory and circulatory components before the convection of the LEV. In Fig. 3.46, it is shown that after the formation and convection of the LEV the outcomes manifest as increases in both the normal and axial force coefficients. The circulatory component of the normal and axial force rapidly increases during the convection of the LEV.

Figure 3.47 shows the wing total force and its noncirculatory and circulatory components at a flapping frequency of 25 Hz. It is evident from Fig. 3.47 that the circulatory

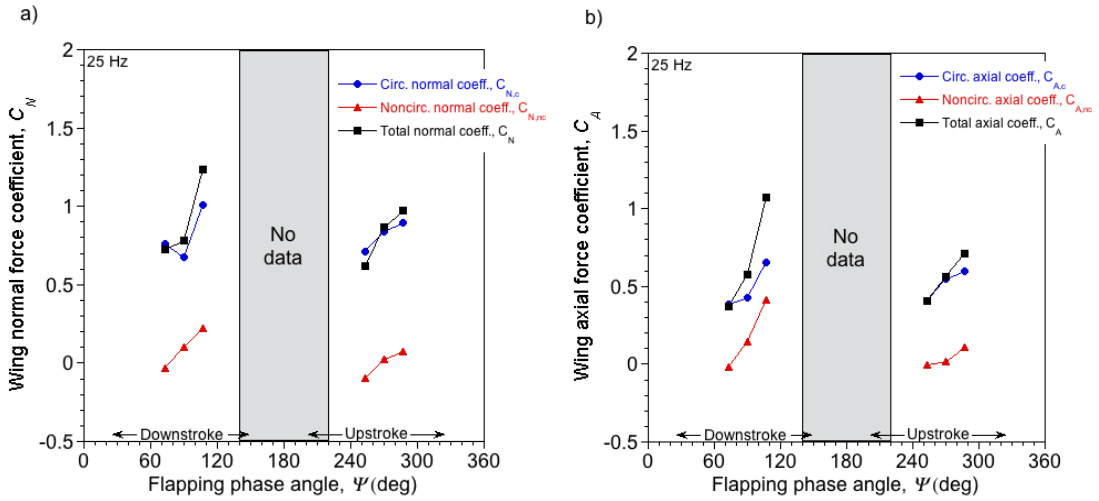

Figure 3.47: Wing total forces decomposed into contributions from noncirculatory and circulatory forces at a flapping frequency of 25 Hz: a) normal force coefficient; b) axial force coefficient.

normal force is the dominant contributor to the total value of the normal force. Throughout both the upstroke and downstroke, the total normal force has slightly higher coefficients than the total axial force. The difference in magnitude between the total normal force and total axial is not as significant as the difference seen in the data measured at 17 Hz.

The total forces acting on the wing were decomposed in the in-plane direction. A positive coefficient value in the in-plane direction represents a force opposing wing motion, and a negative coefficient value represents a propulsive force acting in the direction of the wing motion. Figure 3.48 shows that the in-plane force mostly opposes wing motion during the stroke. It is shown that the in-plane forces can locally act in the direction of wing motion at 17 Hz ($\Psi = 116^\circ$ and $\Psi = 296^\circ$). At 25 Hz, however, it is shown that the wing forces oppose the direction of the wing motion throughout the translational

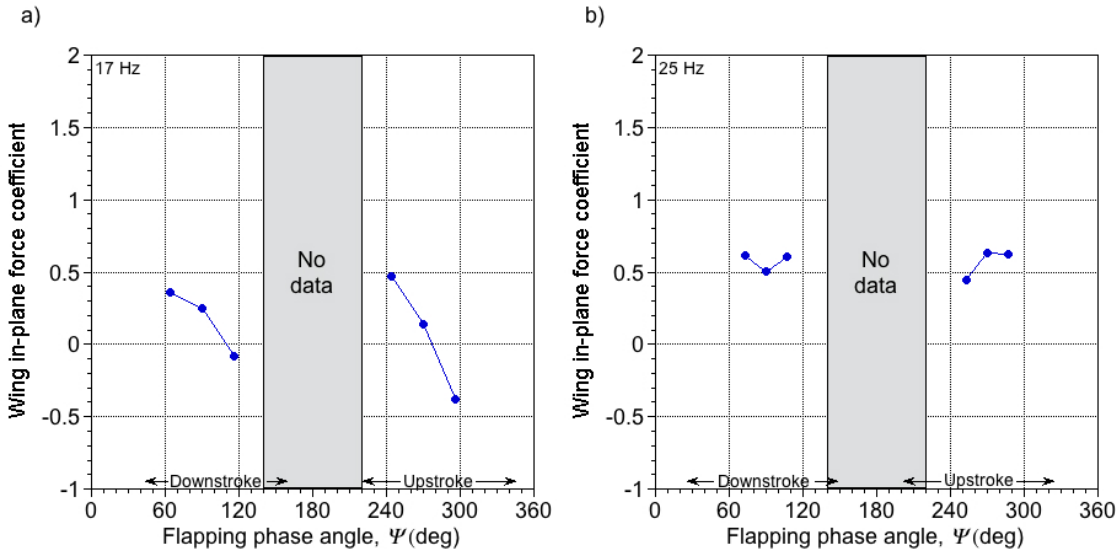

Figure 3.48: Wing total forces decomposed into in-plane force coefficient: a) flapping frequency of 17 Hz; b) flapping frequency of 25 Hz.

stroke. When these in-plane forces were integrated over one flapping cycle, it was found that the wing forces oppose the direction of wing motion. To create the propulsive forces that are necessary for forward flight, the stroke plane would therefore need to be inclined at an angle.

Table 3.1 shows the amount of lift produced in grams by the flapping wing at a frequency of 25 Hz. The actual MAV weighs approximately 12 grams and achieves hovering flight at a flapping frequency of 25 Hz. The values in Table 3.1 have been measured for a single-wing configuration. It is clear that if the measured lift production is multiplied by a factor of two, the net lift then exceeds the vehicle weight.

Flapping Phase Angle (deg)	Lift Production (grams)
73.25	7.938
90	7.995
106.75	11.98
253.25	9.67
270	11.469
286.75	14.61

Table 3.1: Lift production in grams throughout flapping cycle at a flapping frequency of 25 Hz.

3.6.6 Summary

In this section, the noncirculatory and circulatory portions of the lift were combined to evaluate total lift production. The results were also examined in context to the lift-to-drag ratio, both at a sectional level and for the entire wing. It was shown that the lift-to-drag ratio increased with the onset of the LEV formation and shedding process. Such a result is not seen on two-dimensional airfoils at higher chord Reynolds numbers where the onset of dynamic stall leads to a very rapid reduction in the sectional lift-to-drag ratio. This result perhaps sheds some light into why flapping-wing flyers deliberately produce LEVs.

Chapter 4

Concluding Remarks

4.1 Conclusions

Experiments were conducted to help in the understanding of the complex, unsteady, three-dimensional flow field produced by a flexible flapping wing. The wing was taken from a flying MAV concept. High-speed flow interrogation techniques, including time-resolved flow visualization and time-resolved particle image velocimetry, allowed for the time-accurate tracking of the flow features throughout the wing stroke. The complex aeroelastic deformations and wing kinematics were measured using a motion tracking system. Two-dimensional velocity fields were acquired using phase-resolved particle image velocimetry, which also allowed for estimates of the circulatory lift and drag. Once the total lift was calculated, the lift-to-drag ratio of the wing was estimated.

The following conclusions have been drawn from the work conducted during the present research:

1. The flow visualization measurements revealed the presence of a starting vortex at the end of each half-stroke. A turbulent shear layer was also observed to emerge from the trailing edge of the wing throughout its translational stroke. The process of leading-edge vortex (LEV) formation, growth in size and strength of the LEV, and its subsequent convection over the chord was imaged in detail on the upper surface of the wing. The LEV was found to form around the midpoint of the downstroke,

and was shed into the wake at the end of the half-stroke.

2. The flow visualization measurements made in the spanwise plane showed the generation of a root and a tip vortex pair. The root vortex was shown to qualitatively convect through the wake at a greater speed than the tip vortex. Chordwise PIV measurements were used to quantify the peak swirl velocities of the starting vortex at 25% and 50% span locations. In the spanwise plane, the PIV measurements were used to measure the circulation of the root and tip vortex. The tip vortex was found to be stronger than the root vortex, and this relative strength was the main reason that the root vortex convected downward through the wake with a higher velocity.

3. The measurements made using a motion tracking system revealed that the pitch angle during the downstroke and upstroke was nominally symmetric. The flapping wing was also shown to experience large pitch rates, especially during pronation and supination. The measured kinematics were used to calculate the sectional noncirculatory forces on the flapping wing. The pitch rate was found to be the dominant contributor to the production of the noncirculatory lift. The pitch acceleration was shown to be mainly responsible for the large moments during pronation and supination. The sectional values were integrated over the span to calculate the force and moment coefficients on the wing. When integrated over the flapping cycle, it was shown that the noncirculatory forces do not significantly contribute to the total lift produced by the wing.

4. The results from the PIV studies enabled the calculation of the sectional circulatory lift and drag. It was shown that the LEV was responsible for significantly increas-

ing the circulatory lift of the wing during its formation, growth, and convection. The circulatory lift subsequently decreased, and the drag significantly increased when the LEV was shed from the wing. After combining the noncirculatory and circulatory lift into a total lift value, the lift-to-drag ratio estimates revealed that the flapping wing operated more efficiently during the LEV formation and convection process. This outcome contrasts with force measurements of dynamic stall on an oscillating airfoil at higher Reynolds numbers where the lift-to-drag ratio rapidly decreases during LEV shedding. If a flapping-wing airfoil operates more efficiently under these conditions, then this outcome may suggest why biological flyers intentionally produce LEVs during their wing flapping motion.

4.2 Suggestions for Future Work

The results obtained during the course of the present work has provided a new understanding into the aerodynamics of flapping wings. The work has also contributed to the determination of the lift and drag production of flapping wings and assessments of aerodynamic efficiency. From an experimental perspective, however, there are still several key areas that could be addressed to better understand the flapping-wing flow field, and the potential use of a flapping-wing concept as the underpinning of a viable MAV platform.

4.2.1 Spanwise Flow and Stability of the Leading-Edge Vortex (LEV)

The LEV has been shown in both previous work [5, 21] and in the current work to enhance the lift production of a flapping wing. However, there are still remaining questions about the structure and stability of the LEV throughout the flapping cycle. Ellington et al. [3] have shown that a stable conical LEV structure is maintained on the upper surface of the wing because of the presence of a significant spanwise flow. This stable LEV structure, as also seen on delta wings, can be responsible for sustained, enhanced lift generation throughout the entire wing stroke. Research performed by Birch and Dickinson [5] showed a stable LEV structure at a lower chord Reynolds number, but without the presence of a significant spanwise flow. They instead suggested that a downward flow induced by the tip vortex limited the growth of the LEV and contributed to its attachment throughout the stroke. Ramasamy and Leishman [6] showed that the LEV was not stable throughout stroke; in fact, they noted a continuous formation, convection, and shedding process where multiple LEVs were formed during each wing stroke.

While the answers to this question will likely involve understanding the dependencies of the chord Reynolds number effects, the flow interrogation techniques used in the present work could be extended to quantify the spanwise flow inside the LEV, i.e., three-component velocity fields could be measured. To this end, stereoscopic PIV could be used, despite the greater challenges in this case. Stereoscopic PIV differs from conventional two-dimensional PIV in that it uses two cameras. The cameras are carefully focused to the laser light sheet from different camera viewing angles, and after careful calibration can be used to obtain the out-of-plane velocity components in the flow. Such

measurements could shed light onto the effects of any spanwise flow on the structure and stability of the LEV.

4.2.2 Additional Circulatory Lift and Drag Measurements

The measurement resolution of the total lift and drag production on the wing throughout its stroke was limited by the sheer number of experiments that were required and the volume of data. In the present work, measurements were taken at six span locations and six stroke locations at two different flapping frequencies. Additional measurements could be made in the future to provide a more detailed assessment of the lift and drag production throughout the wing stroke. Specifically, improving the spatial and temporal fidelity of the measurements could help to better quantify the lift and drag produced during the process of LEV shedding. Such measurements could provide further insight into the ability of the flapping wing to generate lift after the loss of lift enhancement from the LEV. One key contribution of the present work was the measurement of the sectional lift-to-drag ratio produced on the wing during the process of LEV generation. Additional such measurements could provide better insight into the efficiency of the flapping wing throughout its entire wing stroke.

4.2.3 Definition of the Flapping-Wing Angle of Attack

As mentioned previously, an outstanding problem in flapping-wing research is the proper definition of the angle of attack at the wing sections. Previous work has made assumptions about the flow field in an attempt to estimate the angle of attack. Birch and

Dickinson [5] calculated an angle of attack using the velocity vectors that were acquired using PIV, and Usherwood and Ellington [21] assumed a "triangular" downwash distribution to estimate the angle of attack. Rather than make assumptions about the flapping-wing flow field, however, the angle of attack could also be calculated using the principles of thin airfoil theory. This approach requires measurements of the wing velocity, induced camber, and downwash of the flapping wing. In the present work, the velocity of the wing was acquired from motion-tracking measurements, and the downwash from PIV measurements. The induced camber of a flexible flapping wing, however, is difficult to measure directly, i.e., measuring the camber using the motion-tracking system and retro-reflective markers along the chord is not feasible because the weight of the markers can alter the camber. Instantaneous flow images of the wing show the camber of the wing, but the process of measuring and calculating a representative number of slopes is extremely time-consuming. To this end, the proposed method using thin airfoil theory has been outlined in Appendix B.

Appendix A

Deformation Grid Algorithm

For the PR-PIV and TR-PIV measurements, the images were processed using a deformation grid cross-correlation process [10,57]. This procedure is better for measuring flows with steep velocity gradients, such as vortical flows. A schematic of the procedure is shown in Fig. A.1. The procedure starts with the correlation of an interrogation window of an initial size, which is the first iteration. After the mean displacement in that region has been estimated, the interrogation window is translated by an integer pixel value to achieve better correlation during the second iteration. The third iteration involves the displaced interrogation window being moved by sub-pixel values based on the displacement of the second iteration. The interrogation window is then sheared twice for integer and sub-pixel values based on the velocity correlations from neighboring windows. After the velocity has been calculated after these iterations, the window is split into four equal windows. The windows are then translated by the average displacement estimated from the final iteration of the previous sequence. The procedure is continued until the resolution required to resolve the flow field is achieved. The second interrogation window is deformed until the particles remain at the same location after the correlation.

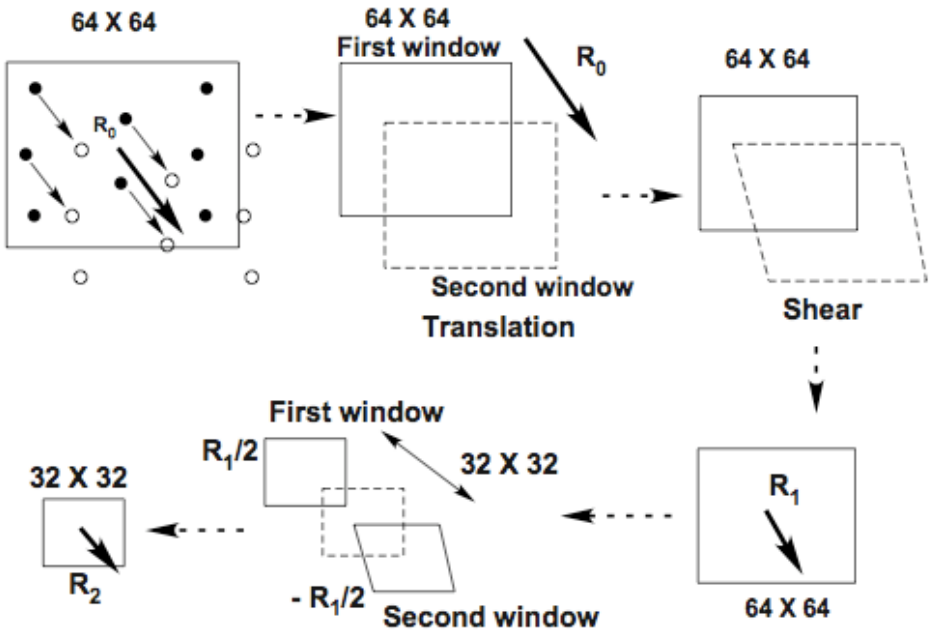

Figure A.1: Schematic of the recursive correlation method [10].

Appendix B

Using Thin Airfoil Theory To Calculate Angle of Attack

The principles of thin airfoil theory could be used to better estimate the angle of attack on a flapping wing. The idea behind thin airfoil theory is that a two-dimensional airfoil can be replaced by a camber line, on which a vortex sheet singularity of unknown strength is placed [1]. The strength of this vortex sheet is found by satisfying flow tangency on the camberline and by invoking the Kutta condition at the trailing edge [1]. A solution for vortex sheet strength is expressed in terms of a Fourier series with harmonics that are given by

$$A_{0,w} = \alpha - \frac{1}{\pi}\int_0^{\pi}\left(\frac{w}{V}\right)d\theta \tag{B.1}$$

and

$$A_{n,w} = \frac{2}{\pi}\int_0^{\pi}\left(\frac{w}{V}\right)\cos n\theta d\theta \tag{B.2}$$

where w is the velocity perturbation, V is the free-stream or local section velocity, and θ is related by $x = -b\cos\theta$. These coefficients can also be written in terms of the airfoil camber by

$$A_{0,dydx} = \alpha - \frac{1}{\pi}\int_0^{\pi}\left(\frac{dy}{dx}\right)d\theta \tag{B.3}$$

and

$$A_{n,dydx} = \frac{2}{\pi}\int_0^{\pi}\left(\frac{dy}{dx}\right)\cos n\theta d\theta \tag{B.4}$$

For a flexible flapping wing, the contributions to the coefficients from the measured velocity field and the geometry of the wing camber must be combined to give the loading on the wing. This is given by

$$A_0 = A_{0,w} + A_{0,dydx} \tag{B.5}$$

and

$$A_n = A_{n,w} + A_{n,dydx} \tag{B.6}$$

To calculate the angle of attack, the result of Eq. (B.5) and the first-order harmonic of Eq. (B.6) needs to calculated, i.e.,

$$C_l = 2\pi \left[A_0 + \frac{A_1}{2} \right] \tag{B.7}$$

With the knowledge that

$$C_l = 2\pi\alpha \tag{B.8}$$

the angle of attack is given by

$$\alpha = A_0 + \frac{A_1}{2} \tag{B.9}$$

This result gives an estimate for the angle of attack of the wing section in terms of both its camber and the external velocity field.

Bibliography

[1] Leishman, J. G., *Principles of Helicopter Aerodynamics*, 2nd ed., Cambridge University Press, New York, NY, 2006.

[2] Mayo, D. B., and Leishman, J. G., "Comparison of the Hovering Efficiency of Rotating Wing and Flapping Wing Micro Air Vehicles," *Journal of the American Helicopter Society*, Vol. 55, 2010.

[3] Ellington, C. P., Van den Berg, C., Willmott, A. P., and Thomas, A. L. R. , "Leading-Edge Vortices in Insect Flight," *Nature (London)*, Vol. 384, 1996, pp. 626–630.

[4] Van den Berg, C., and Ellington, C. P., "The Vortex Wake of a Hovering Model Hawkmoth," *Philosophical Transactions of the Royal Society of London Series B*, Vol. 352, 1997, pp. 317–328.

[5] Birch, J. M., and Dickinson, M. H., "Spanwise Flow and the Attachment of the Leading-Edge Vortex on Insect Wings," *Nature (London)*, Vol. 412, 2001, pp. 729–733.

[6] Ramasamy, and Leishman J. G., "Phase-Locked Particle Image Velocimetry Measurements of a Flapping Wing," *Journal of Aircraft*, Vol. 43, No. 6, 2006, pp. 1867–1875.

[7] Weis-Fogh, T., "Quick Estimates of Flgiht Fitness in Hovering Animals, Including Novel Mechanisms for Lift Production," *Journal of Experimental Biology*, Vol. 59, 1973, pp. 169–230.

[8] Sane, S., "The Aerodynamics of Insect Flight," *Journal of Experimental Biology*, Vol. 206, 2003, pp. 4191–4208.

[9] Heathcote, S., Martin, D., and Gursul, I., "Flexible Flapping Airfoil Propulsion at Zero Freestream Velocity," *AIAA Journal*, Vol. 42, No. 11, November 2004, pp. 2192–2204.

[10] Ramasamy, M., and Leishman, J. G., "Benchmarking Particle Image Velocimetry with Laser Doppler Velocimetry for Rotor Wake Measurements," *Journal of Aircraft*, Vol. 45, No. 11, November 2007, pp. 2622–2629.

[11] Sibilski, K., "Dynamics of Micro-Air-Vehicle with Flapping Wings," *Acta Polytechnica*, Vol. 44, No. 2, 2004, pp. 15–21.

[12] Shyy, W., Lian, Y., Tang, J., Viieru, D., Liu, H., *Aerodynamics of Low Reynolds Number Flyers,* Cambridge University Press, New York, NY, 2008.

[13] Dickinson, M., Lehmann, F. O., Sane, S. P., "Wing Rotation and the Aerodynamic Basis of Insect Flight," *Science*, Vol. 284, No. 5422, 1999, pp. 1954–1960.

[14] Anderson, J. D., *Fundamentals of Aerodynamics,* McGraw-Hill, New York, NY, 2007.

[15] Tarascio, M., Ramasamy, M., Chopra, I., and Leishman J. G., "Flow Visualization of MAV Scaled Insect Based Flapping Wings in Hover," *Journal of Aircraft*, Vol. 42, No. 2, March 2005, pp. 355–360.

[16] Srygley, R. B., Thomas, L. R., "Unconventional Lift-Generating Mechanisms in Free-Flying Butterflies," *Nature (London)*, Vol. 420, December 2002, pp. 660–662.

[17] Warrick, D. R., Tobalske, B. W., Powers, D. R., "Lift Production in the Hovering Hummingbird," *Proceedings of The Royal Society*, Vol. 276, 2009, pp. 3747–3752.

[18] Sun, M., Tang, J., "Unsteady Aerodynamic Force Generation by a Model Fruit Fly Wing in Flapping Motion," *The Journal of Experimental Biology*, Vol. 205, 2002, pp. 55–70.

[19] Shyy, W. and Liu, H., "Flapping Wings and Aerodynamic Lift: The Role of Leading-Edge Vortices," *Journal of Aircraft*, Vol. 45, No. 12, December 2007, pp. 2817–2819.

[20] Van den Berg, C., and Ellington, C. P., "The Three-Dimensional Leading-Edge Vortex of a 'Hovering' model hawkmoth," *Philosophical Transactions of the Royal Society of London Series B*, Vol. 352, 1997, pp. 329–340.

[21] Usherwood, J. R., and Ellington, C. P., "The Aerodynamics of Revolving Wings," *Journal of Experimental Biology*, Vol. 205, 2002, pp. 1547–1564.

[22] Birch, J., Dickson, W., Dickinson, M., "Force Production and Flow Structure of the Leading Edge Vortex on Flapping Wings at High and Low Reynolds Numbers," *Journal of Experimental Biology*, Vol. 207, December 2003, pp. 1063–1072.

[23] Sane, S. P., Dickinson, M., "The Control of Flight Force by a Flapping Wing: Lift and Drag Production," *The Journal of Experimental Biology*, Vol. 204, 2001, pp. 2607–2626.

[24] Theodorsen T., "General Theory of Aerodynamic Instability and the Mechanism of Flutter," National Advisory Committee for Aeronautics, NACA Report 496, 1935.

[25] Tang, J., Viieru, D., and Shyy, W., "Effects of Reynolds Number, Reduced Frequency and Flapping Kinematics on Hovering Aerodynamics," 45th AIAA Aerospace Sciences Meeting and Exhibit, AIAA 2007-129, Reno, NV, January 8–11, 2007.

[26] Ellington, C. P., "The Aerodynamics of Insect Flight. III.," *Philosophical Transactions of the Royal Society of London. Series B.*, Vol. 305, 1984, pp. 41–78.

[27] Ennos, A. R., "The Kinematics and Aerodynamics of the Free Flight of some Diptera," *Journal of Experimental Biology*, Vol. 142, 1989, pp. 49–85.

[28] Lehmann, F. O., Sane, S., Dickinson, M., "The Aerodynamic Effects of Wing-Wing Interaction in Flapping Insect Wings," *Journal of Experimental Biology*, Vol. 208, 2005, pp. 3075–3092.

[29] Ellington, C. P., "The Novel Aerodynamics of Insect Flight: Application to Micro-Air Vehicles," *Journal of Experimental Biology*, Vol. 202, 1999, pp. 3439–3448.

[30] Lehmann, F. O., and Dickinson, M., "The Changes in Power Requirements and Muscle Efficiency During Elevated Force Production in the Fruit Fly Drosophila Melanogaster," *Journal of Experimental Biology*, Vol. 200, 1997, pp. 1133–1143.

[31] Waszak, R. M., Jenkins, N. L., and Ifju, P., "Stability and Control Properties of an Aeroelastic Fixed Wing Micro Aerial Vehicle," AIAA Atmospheric Flight Mechanics Conference, Montreal, CN, August 6–9, 2001.

[32] Ho., S., Nassef, H., Pornsinsirirak, N., Tai, Y-C., and Ho, C.-M., "Unsteady Aerodynamics and Flow Control for Flapping Wing Flyers," *Progress in Aerospace Sciences*, Vol. 39, 2003, pp. 635–681.

[33] Zhao, L., and Deng, X., "Power Distribution in the Hovering Flight of the Hawk Moth Manduca Sexta," *Bioinspiration Biomimetics*, Vol. 4, 2009, pp. 1–7.

[34] Toomey, J., Eldredge, J., "Numerical and Experimental Investigation of the Role of Flexibility in Flapping-Wing Flight," 36th Fluid Dynamics Conference and Exhibit, San Francisco, CA, June 5–8, 2006.

[35] Bomphrey, R. J., Lawson, N. J., Taylor, G. K., Thomas, A. L. R., "Application of Digital Particle Image Velocimetry to Insect Aerodynamics: Measurement of the Leading-Edge Vortex and Near Wake of a Hawkmoth," *Expieriments in Fluids*, Vol. 40, 2006, pp. 546–554.

[36] Birch, J., Dickinson, M., "The Influence of Wing-Wake Interactions on the Production of Aerodynamic Forces in Flapping Flight," *Journal of Experimental Biology*, Vol. 206, March 2003, pp. 2257–2272.

[37] Wang, Z. J., Birch, J. M., Dickinson, M. H., "Unsteady Forces and Flows in Low Reynolds Number Hovering Flight: Two-Dimensional Computations vs. Robotic Wing Experiments," *Journal of Experimental Biology*, Vol. 207, 2003, pp. 449–460.

[38] Poelma, C., Dickson, W. B., Dickinson, M. H., "Time-Resolved Reconstruction of the Full Velocity Field Around a Dynamically-Scaled Flapping Wing," *Experiments in Fluids*, Vol. 41, May 2006, pp. 213–225.

[39] Wu, J. C., "Theory for Aerodynamic Force and Moment in Viscous Flows," *Journal of Aircraft*, Vol. 19, No. 4, 1981, pp. 432–441.

[40] Willert, C. E., and Gharib, M., "Digital Particle Image Velocimetry," *Experiments in Fluid*, Vol. 10, No. 4, January 1991, pp. 181–193.

[41] Huang, H., Dabiri, D., and Gharib, M., "On Errors of Digital Particle Image Velocimetry," *Measurement Science and Technology*, Vol. 8, No. 12, December 1991, pp. 1427–1440.

[42] Keane, R. D., and Adrian R. J., "Theory of Cross-Correlation Analysis of PIV Images," *Measurement Science and Technology*, Vol. 49, No. 3, July 1991, pp. 191–215.

[43] Westerweel, J., "Fundamentals of Digital Particle Image Velocimetry," *Measurement Science and Technology*, Vol. 8, No. 12, December 1997, pp. 1379–1392.

[44] Adrian, R. J., "Particle-Imaging Techniques For Experimental Fluid Mechanics," *Annual Review of Fluid Mechanics*, Vol. 23, 1991, pp. 261–304.

[45] Keane, R. D., and Adrian R. J., "Optimization of Particle Image Velocimeters," *Measurement Science and Technology*, Vol. 1, No. 11, November 1991, pp. 1202–1215.

[46] Raffel, M., Willert, C., Wereley, S., Kompenhans, J.., *Particle Image Velocimetry*, 2nd ed., Springer Publishing Company, New York, NY, 2007.

[47] Karamcheti, K., *Principles of Ideal-Fluid Aerodynamics* John Wiley and Sons, Inc., New York, NY, 1966.

[48] Bisplinghoff, R. L., Ashley, H., and Halfman, R. L., *Aeroelasticity* Addison-Wesley Publishing Co., Reading, MA, 1955.

[49] Bhagwat, M., and Leishman, J. G., "Measurements of Bound and Wake Circulation on a Helicopter Rotor," *Journal of Aircraft*, Vol. 37, No. 2, March 2000, pp. 227–234.

[50] Ramasamy, M., Johnson, B., Leishman, J. G., "Understanding the Aerodynamic Efficiency of a Hovering Micro-Rotor," *Journal of the American Helicopter Society*, Vol. 53, No. 4, October 2008, pp. 412–428.

[51] Betz, A., "Behavior of Vortex Systems," National Advisory Committee for Aeronautics, NACA TM 713, 1935.

[52] Giles, M, and Cummings, R. M., "Wake Integration for Three-Dimensional Flowfield Computations: Theoretical Development," *Journal of Aircraft*, Vol. 36, No. 2, April 1999, pp. 357–365.

[53] Kusunose, K., "Drag Prediction Based on a Wake-Integral Method," 16th Applied Aerodynamics Conference, Albuquerque, NM, June 15–18, 2001.

[54] McAlister, K. W., Schuler, C. A., Branum, L., and Wu, J. C., "3-D Wake Measurements Near a Hovering Rotor for Determining Profile and Induced Drag," National Aeronautics and Space Administration, NASA TP 3577 ATCOM TR 95-A-006, August 1995.

[55] McCrosky, W. J., McAlister, K. W., Carr, L. W., and Pucci, S. L., "An Experimental Study of Dynamic Stall on Advanced Airfoil Sections," National Aeronautics and Space Administration, NASA TM-84245, 1982.

[56] Leishman, J. G., *The Helicopter: Thinking Forward, Looking Back,* College Park Press, College Park, MD, 2007.

[57] Scarano, F., "Iterative Image Deformations Methods in PIV," *Measurement Science and Technology*, Vol. 13, 2002, pp. R1–R19.